TUNING CARBON MOLECULAR SIEVE MEMBRANE PERFORMANCE FOR CHALLENGING GAS SEPARATIONS

A Dissertation
Presented to
The Academic Faculty

by

Graham B. Wenz

In Partial Fulfillment
of the Requirements for the Degree
Doctor of Philosophy in Chemical Engineering

Georgia Institute of Technology
May 2017

TUNING CARBON MOLECULAR SIEVE MEMBRANE PERFORMANCE FOR CHALLENGING GAS SEPARATIONS

Approved by:

Dr. William J. Koros, Advisor
School of Chemical and Biomolecular Engineering
Georgia Institute of Technology

Dr. Ryan P. Lively
School of Chemical and Biomolecular Engineering
Georgia Institute of Technology

Dr. Peter J. Ludovice
School of Chemical and Biomolecular Engineering
Georgia Institute of Technology

Dr. Pradeep K. Agrawal
School of Chemical and Biomolecular Engineering
Georgia Institute of Technology

Dr. Meisha L. Shofner
School of Material Science and Engineering
Georgia Institute of Technology

Date Approved: April 3rd, 2017

This work is dedicated to my parents.

ACKNOWLEDGEMENTS

This has been a journey with many ups and downs, and would not have been possible without the support of many people. First and foremost, I have to express my sincere gratitude to my advisor, Dr. William J. Koros. I am almost certain that I will never meet another human being more dedicated to their work. His combination of endless energy (coffee probably helps here), depth of knowledge and desire to "push the boundaries" has been, and will continue to be, inspirational. I can certainly say that without his guidance and support, I would not have made it to this point. I would also like to thank my Ph.D. committee members: Dr. Pradeep K. Agrawal, Dr. Ryan P. Lively, Dr. Pete J. Ludovice, and Dr. Meisha L. Shofner for valuable input and guidance through the important steps of my Ph.D. education.

Throughout my time in the Koros group, I have had the great fortune to learn, collaborate and socialize with some amazing researchers and people. I would first like to thank all of the previous Koros group members for setting up the "kingdom" that I have utilized over the past 5 years, particularly JR Johnson and Oguz Karvan; while I did not overlap with either of you for an appreciable amount of time, I benefitted greatly from your engineering design and foresight. Justin Vaughn and Vinod Babu had the joy of sharing an office with me and both made for helpful discussions about research, but more importantly about cooking, ornithology, and activities in Atlanta. Steven Burgess shared valuable time with me, both in lab and at Dunkin' Donuts - providing much needed breaks. Yu-Han Chu and Shilu Fu were always there for great conversations, to remind me that I should eat less, and put up with entirely too many pranks from me. Towards the

end Chen Zhang and Gongping Liu were important colleagues and friends, serving as much needed sounding boards for a variety of subjects. Special thanks to Manjeshwar Kamath for providing tasty Indian treats on Thursdays. To the rest of the Koros group (past and present): thank you for your input and guidance throughout my time here!

Outside of Bunger-Henry I have had an amazing group of friends that were an integral part of my time here, providing me with many laughs and good times. Andrew Tadros, Joanna Tsao, Dalar Nazarian, Chris Boyd, Kevin Ling, Weipeng Zhou, Michael Dutzer, Jared Schwartz and Sylvia Sullivan are just of the few were always available for shenanigans. Miles Sakwa-Novak was a go-to for sports talk, grilling and in-depth discussions of things we take for granted (e.g. why are there two tides in a day?). Last but not least, Steph Didas has been the most important source of support, companionship, and guidance throughout this process. I can say, without a shred of doubt, this would have been a much darker experience without her.

I would also like to thank my parents, Marilyn Larsen and Jeff Wenz, for the continual support throughout my life, particularly during this step. While each one of my life decisions to this time has moved me further away from “home”, they never blinked in helping me see things through. They both know my struggles all too well and were always available to listen and provide words of wisdom, but more importantly, to revel alongside me in my successes. For that I will be forever grateful.

There are so many more people to thank, but in the interest of time I’ll summarize with this: thank you all for everything, and if you have read this I’ll buy you a beer (or two) the next time I see you.

TABLE OF CONTENTS

LIST OF TABLES

LIST OF FIGURES

SUMMARY

Intrinsically energy efficient membrane-based processes are emerging as transformational tools for large-scale industrial gas separations. Their simplicity and potential to reduce energy use and greenhouse gas emissions as well as operating and maintenance costs make them desirable alternatives to traditional thermally-driven phase-change based separations. However, direct replacement of traditional separation processes is not yet viable due to low separation efficiency of current membrane materials; nevertheless, development of advanced membrane materials to increase overall membrane separation efficiency is an area of significant industrial and academic research.

Carbon molecular sieve (CMS) membranes, formed by high temperature pyrolysis of polymers under controlled conditions, have emerged as a new class of materials that can surpass the polymer permeability-selectivity "upper bound". Similar to their glassy polymer precursors, CMS materials display a physical aging phenomenon where productivity loss is coupled with a mild increase in selectivity, over time. A majority of this thesis has focused on development of a post-synthetic treatment where CMS hollow fiber membranes are exposed to a solution containing parts per million (ppm) levels of amine dopants with the goal of restricting "free volume" relaxation associated with physical aging. While long-term permeation experiments showed that aging-resistant membranes were not formed, attractive separation performance resulted from amine doped materials. Further characterization suggests amine doping as a new technique to selectively modify large pores present within CMS materials, resulting in increased size and shape selectivity for both CO_2/CH_4 and C_3H_6/C_3H_8 separations investigated.

CMS materials exhibit an attractive combination of productivity and selectivity owing to their bimodal distribution of size selective ultramicropores and high sorption capacity micropores; however, due to their amorphous nature, traditional spectroscopic techniques fail to provide the angstrom-level details of the CMS structure enabling true materials engineering. A self-consistent mechanism for transformation of a flexible random coil polyimide precursor to the resulting ultra-rigid CMS was presented, enabling connection of precursor structure, formation and processing conditions to resulting CMS separation performance.

Lastly, low-level concentrations of molecular oxygen present within the pyrolysis atmosphere was used as a fine tuning technique to enhance separation performance of CMS membranes for the C_2H_4/C_2H_6 gas pair. Molecular oxygen reacts with the edges of the size selective ultramicropores within CMS materials, not the micropores responsible for sorption, resulting in increased diffusional selectivity for C_2H_4/C_2H_6 with moderate reductions in overall membrane productivity.

While this thesis focused on modifications of 6FDA:BPDA-DAM(1:1) derived CMS membranes, the framework provided can be extended to CMS materials derived from different polymeric precursors and pyrolysis conditions. Insights gained from the CMS modification techniques employed here resulted in expanding fundamental knowledge of the complex CMS microstructure, providing key information for directed materials engineering of CMS membranes for challenging gas separations.

CHAPTER 1. INTRODUCTION

1.1 Energy Production: Advancements and Implications

With population increases and widespread economic development, the global demand for energy is rapidly increasing. While coal has been, and for some regions remains an essential source of energy the relatively high amounts of CO_2 emitted from coal combustion is a key contributor to increasing atmospheric CO_2 concentrations and global climate change.

Natural gas has emerged as an attractive alternative fossil fuel to coal due to its abundance and relatively low carbon intensity, emitting 50-60% less CO_2 during combustion. Advancements in upstream oil and gas techniques, such as horizontal drilling and hydraulic fracturing, have enabled access to natural gas and oil reservoirs that were previously uneconomical to produce with standard methods. For example, domestic natural gas production is expected to increase from 27.2 Tcf (trillion cubic feet) in 2015 to ~42 Tcf in 2040 (cf. Figure 1.1), primarily as a result of development of shale gas, tight oil, tight gas, and offshore gas preserves, commonly referred to as unconventional plays (*1*). Additionally, increased production and access to natural gas has reinvigorated research and development of gas-to-liquids (GTL) processes, where natural gas is a feedstock for production of valuable hydrocarbons – alternative to traditional heavy oil-based feedstocks for refining (*2*, *3*).

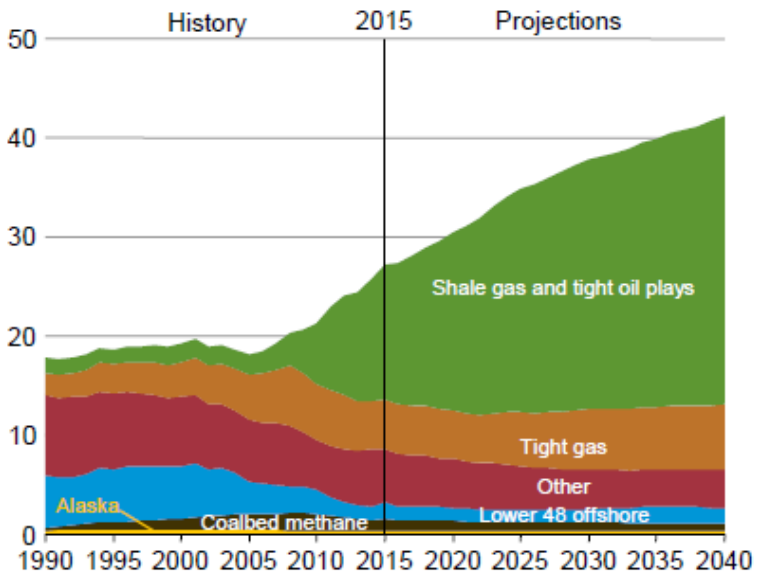

Figure 1.1. United States dry natural gas production from 1990 to 2040 (predicted) in trillion cubic feet (Tcf) (*1*).

Although the majority constituent of raw natural gas is CH_4 (75-90%), a number of light hydrocarbons (C_2-C_4) can be present in small concentrations (1-3%) along with common impurities like H_2O, CO_2, H_2S, and N_2. Presence and concentration of these additional natural gas constituents is heavily dependent upon geographical location and well production techniques. Before natural gas can be introduced into pipeline distribution processes, these contaminants must be removed or reduced to predetermined specifications, making upstream natural gas treatment the largest industrial scale gas separation (*4*). Here "upstream" refers to the processes associated with discovery, extraction and distribution of fossil fuels from naturally occurring formations.

Removal of H_2O, CO_2, and H_2S is necessary, as these impurities cause corrosion and damage of pipelines, transmission and processing equipment. It is also desirable to remove inert gases (e.g. N_2), as they reduce the overall heating value of the product gas,

and contribute to increased compression costs associated with distribution. In fact, separation of N_2, CO_2, and H_2S is of critical importance, as many enhanced oil recovery operations involve reinjection of these gases back into the formations in order to stimulate well production, leading to increased concentrations of these species over the lifetime of a well.

Bulk separations for natural gas treatment, or upgrading, is typically performed via solvent-based absorption processes, with amine-based solvents being the most popular. However, use of absorption solutions requires a complementary stripping process where thermally-driven regeneration of the solvent is performed to remove the absorbed species (e.g. CO_2). The combination of large energy requirements and significant capital, operational and maintenance expenses lead to absorption systems becoming very costly for natural gas upgrading. Additionally, the large footprint of the absorption system and additional supporting equipment make these systems impractical for off-shore, remote, or relatively low volume gas reservoirs – which comprise a majority of the newly discovered natural gas plays. Clearly industry is looking for alternative separation solutions, allowing for further development of these reserves.

Additionally, increased natural gas production has created a shift in the downstream petrochemical industry, where natural gas utilization as fuel and chemical feedstocks is projected to increase 1.3%/year (*1*). Here "downstream" refers to the refining and conversion of fossil fuels (e.g. natural gas and oil) into value-added products such as transportation fuels and bulk commodity chemicals. Associated hydrocarbon components (ethane, propane, butane, etc.) of raw natural gas streams, or natural gas liquids (NGLs), are desirable feedstocks for downstream processes and are of significant

value. These NGLs are typically fed into a steam cracking furnaces, along with traditional naptha feedstocks, to create light olefins ethylene and propylene which are important building blocks for a variety of chemicals and consumer products. The composition cracking effluent depends on the composition of the feedstocks and cracking conditions, but invariably is a mixture of both the desired olefins and unwanted paraffins. Therefore, separation of olefins from paraffins is required in order to produce olefins of desired purity, recycling residual paraffins back into the cracking process.

Separation of olefins from paraffins is dominated by distillation, a thermally-driven phase-change based process. While distillation can be performed at ambient conditions, due to chemical similarities of light olefins and paraffins this is often not possible. For example, the similar critical temperatures of C_2H_4 and C_2H_6 (283 K and 306 K, respectively (*5*)) require a cryogenic distillation process with column temperatures of -23 °C and pressures of 320 psig, resulting in high capital and energy costs. A recent study reported that separating C_2 and C_3 olefins from paraffins uses approximately 0.3% of the global energy supply, highlighting the importance and scale of this separation (*6*).

From the examples given above, clearly there are opportunities for energy and cost reduction in large-scale gas separations. Due to the prevalence of traditional phase-change thermally-driven separation techniques, increased efficiency of electricity generation and use is an obvious area for process improvement; however, non-thermal separations, or techniques that do not depend upon a phase-change are of particular interest. Membrane-based separations represent a growing field for energy-efficient large-scale gas separations. While direct replacement of traditional absorption or distillation processes is currently not viable due to the relatively low separation efficiency

of current membrane materials, many variations of hybrid membrane-absorption and membrane-distillation systems have been proposed (*7–10*). In these processes, membrane modules are placed upstream of traditional thermally-driven separation operations, allowing for practical retro-fitting of existing infrastructure. In these systems the membrane acts as a first pass separator, with the subsequent unit operation acting as a "polishing" step, achieving the desired process specifications for the separation. This configuration allows for direct and immediate implementation of currently available membrane materials, provided the application is of economic and engineering viability. Therefore, it is not necessary to wait for the design of a "perfect membrane" that will allow for direct replacement of current absorption or distillation processes, as the associated energy-reductions with implementation of a complementary membrane unit can be realizable in the immediate future. Nevertheless, improved membrane materials and processes can lead towards increased efficiencies and is an area of significant research, both academically and industrially.

1.2 Membrane-based Gas Separations

Intrinsically energy efficient membrane-based processes are emerging as transformational tools for large-scale gas separations. Their simplicity and potential to reduce energy use, greenhouse gas emissions as well as operating and maintenance costs make them desirable, compared to current phase-change based separations. Membrane-based gas separations are not as well developed as water purification techniques (i.e. microfiltration, ultrafiltration, nanofiltration and desalination), partially due to the increased selectivity required and the challenges associated with achieving these selectivities. For example, reverse osmosis membranes are able to separate free water

(3 Å) from solvated cations and anions (~6 Å), an approximate 100% difference in effective size; however, the effective size difference between CO_2 (3.3 Å) and CH_4 (3.8 Å) is only ~15%, highlighting the challenges associated with gas separations (*11*).

Membrane-based gas separations involve passing a pressurized feed gas over the upstream side of the module, where one (or more) constituents passes through to the downstream side of the membrane forming a permeate stream, and the retained species of the feed exits the module as a retentate flow (cf. Figure 1.2). Manufacturing and engineering aspects such as: 1) development of high-efficiency modules; 2) advanced materials capable of high separation efficiency; 3) morphology control across multiple length scales; 4) high-speed processing allowing combination of factors 1-3 into defect-free modules, are of equal importance in development of successful membrane separation processes (*12*). Considering these factors, spiral wound and asymmetric hollow fiber modules have emerged as the most common morphologies for gas separation membrane packaging, schematics of which are shown in Figure 1.2. However, asymmetric hollow fibers have the distinct advantage of offering roughly 10X higher surface area-to-volume ratios compared to spiral wound, with 10,000 m^2/m^3 configurations possible (*11*). This fact, along with others, has identified asymmetric hollow fibers as the industrially preferred configuration, resulting in a number of commercialized spinning and module formation technologies.

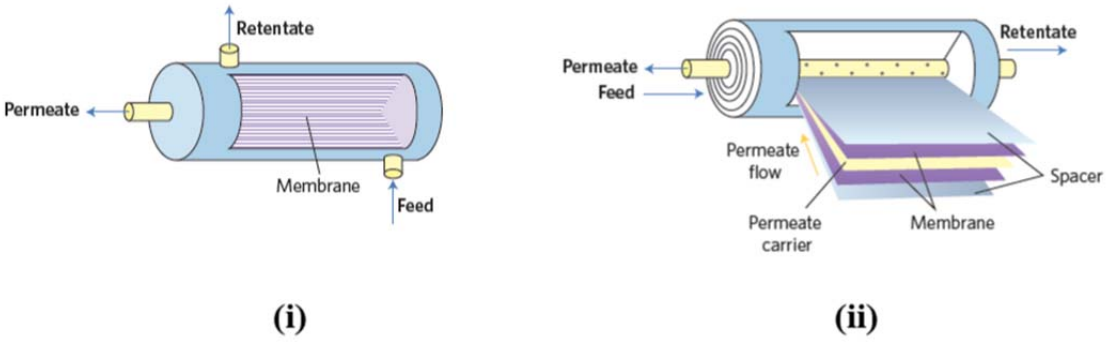

Figure 1.2. Schematic of (i) hollow fiber membrane module; and (ii) spiral wound membrane modules. Adapted from (*13*).

Transport within dense membranes or microporous membranes follow the sorption-diffusion model, of which details will be described in Chapter 2. Permeability (P_A) is a measure of the intrinsic productivity of a penetrant through a membrane, and depends upon the transmembrane driving force and membrane thickness (l_m) normalized flux of the penetrant of, via:

$$P_A = \frac{[\text{flux of A}]}{[\text{transmembrane driving force of A}]/[l_m]} = \overline{D}_A \times \overline{\mathbb{S}}_A \tag{1.1}$$

Permeability can also be described by a *multiplicative relationship* between both penetrant-material (sorption, $\overline{\mathbb{S}}_A$) interactions as well as kinetic (diffusion, $\overline{D}_A$) processes, allowing for a wide variety of materials exploration and development, enabling tuning of membrane material properties via these two "handles".

1.2.1 Flexible Polymeric Membranes

The most prevalent material for current gas separation membranes are polymers due to their relative low cost, attractive mechanical properties, and ease of processability into free-standing membranes. Much research has been devoted to characterizing gas transport through polymeric materials, seeking relationships between chemical structures and resulting separation performance. In flexible polymers (i.e traditional rubbery and glassy polymers), gas transport occurs via penetrant-scale gaps that are distributed throughout the material due to thermally-driven chain segmental motion. For most gas pairs, glassy polyimides have been identified as the preferred membrane material, as they possess attractive mechanical strength, high durability and desirable transport properties. Despite these advantages, one of the major challenges to widespread development of solution processable polymeric materials for gas separation membranes is the inherent trade-off between productivity and separation efficiency, commonly referred to as the upper-bound (*14–16*). This indicates that traditional polymer membranes may not have the desired high permeability and high selectivity required for use in large-scale gas separations. Additionally, exposure to high pressures (activities) of condensable components (e.g. CO_2 or hydrocarbons) leads to increased segmental motion, or plasticization, resulting in performance reductions. However, slight modifications in polymer structure, or post-treatments, have enabled suppression of the plasticization with addition of covalent crosslinking between polymer chains (*17*, *18*). These factors suggest that materials of increasing rigidity may result in attractive gas separation membranes.

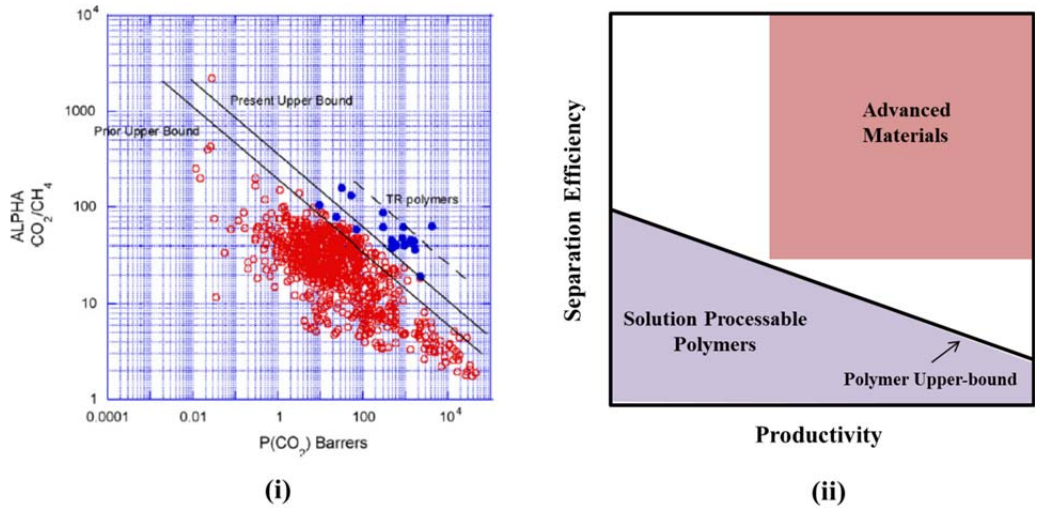

Figure 1.3. (i) 2008 Robeson upper-bound tradeoff for CO_2/CH_4 (*15*); (ii) representative upper-bound identifying region of combined separation efficiency and productivity that is desired.

1.2.2 Polymers of Intrinsic Microporosity

Considered a semi-rigid material, polymers of intrinsic microporosity (PIMs) have been recently introduced as a class between the previously mentioned flexible polymers and rigid molecular sieves that will be discussed later (*19*). These materials are typically hyper-rigid polymers with carefully selected "contortion points" that enable microporosity retention by preventing relaxation of the polymer chains (cf. Figure 1.4). These materials exhibit impressive combinations of productivity and selectivity for relatively dissimilar gas penetrant pairs (i.e. H_2 from CH_4 or air), even redefining the upper-bound relationships for a few gas pairs (*20*, *21*). However, due to the semi-rigid nature of the backbone, inefficient discrimination between similarly sized penetrants (i.e. olefins/paraffins) limits their applicability for these challenging separations (*22*, *23*). Although there has been a wide variety of PIM-based materials developed as gas separation membranes, to date, there is only one report of translation of a PIM into the

industrially preferred asymmetric hollow fiber morphology (*24*). Nevertheless, further investigation of these materials is warranted as gas separation membranes.

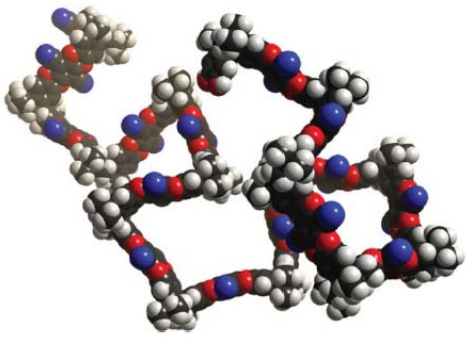

Figure 1.4. Molecular model of PIM-1 showing rigid segments connected by bulky contortion points (*19*).

1.2.3 Crystalline Molecular Sieves: Metal Organic Frameworks (MOFs) and Zeolites

Rigid molecular sieves have emerged as promising gas separation materials due to their relative chemical stability and lack of plasticization that is associated with traditional polymeric materials. Within this broad class there are two main subclasses: crystalline and amorphous sieves. Zeolites and metal organic frameworks (MOFs) comprise a majority of crystalline molecular sieving materials investigated for gas separations. MOFs are porous networks formed by metal ions/clusters connected by organic linkers, and provide an immense amount of structure tuning capability. However, with respect to a majority of gas separations of interest (CO_2/CH_4, C_2H_4/C_2H_6, C_3H_6/C_3H_8) few zeolite or MOF materials exist with pore sizes enabling efficient separations. Additionally, while a number of studies report ability to form supported defect-free supported zeolite and MOF membranes for gas separations (*25–27*), realistic

scalability to industrially relevant membrane surface areas (hundreds or thousands of m^2) is challenging.

1.2.4 Hybrid Materials

Hybrid materials, or alternatively mixed-matrix membranes, are formed by dispersion of a preformed rigid molecular sieving material (i.e. zeolite, MOF, CMS) within a continuous polymer matrix. Ideally, this configuration will result in both higher selectivity and permeability compared to the neat polymer matrix resulting in a performance surpassing the upper-bound. For such materials, relative ease of processability is retained owing to the polymer matrix, allowing use of traditional membrane formation techniques.

While hybrid materials are simple in theory, much research has shown that in order to attain attractive performance proper matching of the sieve and matrix is crucial. Considering ZIF-8 hybrid membranes for the C_3H_6/C_3H_8 separation, an optimal ratio of continuous phase (polymer) to dispersed (sieve) permeability is ~0.15, allowing for achievement of the highest combination of selectivity and permeability (*13*). However, this is not a unique ratio and needs to evaluated for each polymer-sieve combination for the gas pair of interest. It should be noted that addition of ZIF-8 does not increase the attraction between the hybrid membrane and C_3H_6/C_3H_8 penetrants, but rather the rigid sieve leads to an increased diffusional (kinetic) selectivity of the hybrid material over the neat polymer (*28*), typical of most hybrid membrane systems. A recent study showed that incorporation of a large pore MOF Ni_2(dobdc) resulted in increased C_2H_4/C_2H_6 selectivity due to attraction between the olefin and the open metal sites, driving performance of this hybrid membrane past the respective upper-bound (*29*). This is a

unique case, as addition of dispersed phases resulting in increased hybrid membrane sorption, not diffusion, selectivity are less common.

While these two cases show significant enhancement due to inclusion of rigid sieve dispersed phases, this is not always the case with hybrid membrane materials. Additionally, engineering proper adhesion between dispersed and polymer phases is crucial in order to form defect-free hybrid membranes. While asymmetric hybrid membranes have been reported (*30*, *31*), inclusion of rigid particles makes transformation from flat-sheet to defect-free hollow fibers non-trivial and is one of the factors currently limiting widespread application of hybrid materials.

1.2.5 Amorphous Molecular Sieves: Carbon Molecular Sieves

While supported MOF/zeolite membranes may not break through as industrial scalable gas separation materials, carbon molecular sieve (CMS) membranes have the ability for realization as large-scale gas separation materials. CMS membranes are usually formed by the high temperature pyrolysis of polymeric precursors, enabling synthesis of free-standing CMS membranes from a variety of materials. The resulting CMS materials are envisioned to be comprised of a slit-like pore structure consisting of a bimodal pore size distribution allowing for both high productivity and high selectivity (cf. Figure 1.5), and have proven to exhibit attractive performance for a variety of challenging gas separations (*32–36*). Additionally, as they are typically derived from polymeric precursors, asymmetric CMS hollow fiber membranes can be formed by the addition of a pyrolysis step. Being polymer derived positions CMS materials well for application to large-scale gas separations, as well known polymer membrane processing and module manufacturing techniques may be extended for use with CMS membranes.

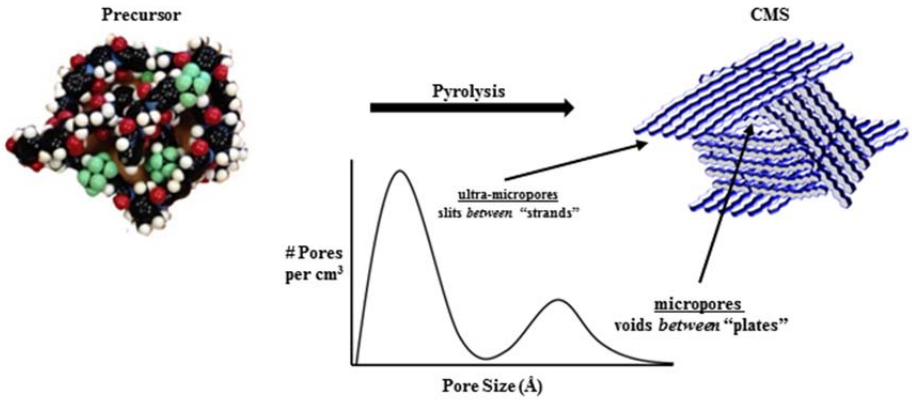

Figure 1.5. Schematic showing transition of flexible polymer precursor to rigid slit-like CMS structure with bimodal pore size distribution (*37*).

1.3 Research Objectives

Separation performance of CMS membranes is dependent upon many factors such as polymer precursor structure and pyrolysis conditions, from which various combinations allow for tailoring CMS structure and resulting performance. However, similar to their polymer precursors, CMS membranes are subject to a physical aging phenomenon, where it is envisioned that partial densification leads to minor changes in the structure, causing reduced membrane productivity coupled with increased selectivity (*38*, *39*). While this is not a "show stopper" for the advancement of CMS membranes as attractive gas separation materials, or feasibility of industrial application, attempts at understanding and suppressing this phenomenon may provide insight into both CMS structure and key material processing parameters.

Furthermore, while the amorphous bimodal structure of CMS materials results in attractive separation performance, traditional characterization techniques of microscopy, scattering and spectroscopy utilized for ordered materials fails to provide angstrom-level detail of the CMS structure. This highlights the need for additional characterization

approaches in order to facilitate directed engineering of CMS materials, enabling further enhancement in performance for challenging gas separations.

This thesis will focus on the advancement of fundamental understanding of CMS membranes by *developing methods for investigating and controlling separation performance of carbon molecular sieve membranes* in order to probe impacts of various formation and post-synthetic treatments upon resulting CMS membrane performance. The primary objectives of this dissertation are as follows:

1. **Development of post-synthetic modification of carbon molecular sieve membranes with diamine dopants. (Chapter 4)**

The first objective of this research outlines a new post-synthetic modification technique where CMS membranes are exposed to a solution containing parts per million (ppm) levels of amine dopants, with the original goal of preventing the "free volume" relaxation within CMS materials associated with physical aging. While long term CO_2 and CH_4 permeation experiments showed that aging-resistant membranes were not formed, attractive performance resulted from the amine doped materials. The results of these experiments suggest amine doping as a new technique to selectively modify the large pores present within the CMS microporous structure, resulting in increased size and shape based selectivity.

2. Investigation of size and functionality of amine dopants for modification of carbon molecular sieve membranes (Chapter 5)

Initial amine doping studies focused on *p*-phenylene diamine due to its rigid bulky structure. The interplay between amine dopant concentration and resulting performance suggested this approach as a new tuning tool for CMS membranes. This objective examines amine dopant size and reactivity to connect dopant type and resulting CMS membrane performance. Transport measurements of CO_2, CH_4, C_3H_6, and C_3H_8 were used to probe effects of amine dopants upon treated membranes, providing insights into how dopant structure impacts CMS microporosity. Additionally, nuclear magnetic resonance (NMR) measurements were employed to investigate the chemical reactions between amine dopant and CMS membranes.

3. Hypothetical transformation pathway from random coil precursor to rigid carbon molecular sieve matrix (Chapter 6)

Carbon molecular sieve materials display exquisite size and shape selectivity for a variety of penetrants; however, there is a non-trivial connection between precursor structure and resulting CMS performance. This work takes an initial step in connecting the transformation of a flexible random coil polyimide into an ultra-rigid CMS material with impressive separation performance for a variety of gas penetrants. A hypothetical CMS evolution pathway is proposed and discussed in a self-consistent manner with previously reported analyses for CMS materials derived from two heavily investigated polyimide precursors: Matrimid® and 6FDA:BPDA-DAM(1:1).

4. **Investigation of low-level oxygen doping of carbon molecular sieve membranes for olefin/paraffin separations (Chapter 7)**

Olefin/paraffin separations comprise a significant fraction of energy usage in the petrochemical industry; therefore, small enhancements in separation efficiency can result in large energy savings. Hybrid membrane-distillation systems have been proposed to reduce the energy consumption of existing units, but few membrane materials have shown separation performance worthy of implementation. This objective seeks to improve CMS separation efficiency by extension of previously developed oxygen doping for CO_2/CH_4 separations as an ultra-fine pore tuning technique for the challenging C_2H_4/C_2H_6 gas pair, which differ in effective sizes by 0.1 Å.

1.4 Dissertation Organization

Following this introductory chapter there are seven additional chapters within this dissertation. Chapter 2 will provide all the necessary theory and background for comprehension of the research presented in the following chapters. Chapter 3 describes the materials, experimental methods, equipment and characterization techniques used throughout this work. Chapters 4-7 will contain the main body of research presented, corresponding to the four research objectives outlined above. Finally, Chapter 8 will summarize the key findings of this work and recommend future paths of research relevant to this field of study. Appendices have been included as a means for complementary results, but are not critical to the main body of the work presented in this dissertation.

1.5 References

(1) *International Energy Outlook - 2016*; 2016, U.S. Energy Information Administration: Washington, D.C.

(2) Wilhelm, D.; Simbeck, D.; Karp, A.; Dickenson, R. Syngas production for gas-to-liquids applications: technologies, issues and outlook. *Fuel Process. Technol.* **2001**, *71*, 139–148.

(3) Wood, D. A.; Nwaoha, C.; Towler, B. F. Gas-to-liquids (GTL): A review of an industry offering several routes for monetizing natural gas. *J. Nat. Gas Sci. Eng.* **2012**, *9*, 196–208.

(4) Baker, R. W.; Lokhandwala, K. Natural Gas Processing with Membranes: An Overview. *Ind. Eng. Chem. Res.* **2008**, *47*, 2109–2121.

(5) Breck, D. W. *Zeolite Molecular Sieves: Structure, Chemistry, and Use*; Wiley & Sons: New York, NY, 1974.

(6) Sholl, D. S.; Lively, R. P. Seven chemical separations to change the world. *Nature* **2016**, *532*, 6–8.

(7) Freeman, B.; Hao, P.; Baker, R.; Kniep, J.; Chen, E.; Ding, J.; Zhang, Y.; Rochelle, G. T. Hybrid Membrane-absorption CO2 Capture Process. *Energy Procedia* **2014**, *63*, 605–613.

(8) Xu, L.; Rungta, M.; Brayden, M. K.; Martinez, M. V.; Stears, B. A.; Barbay, G. A.; Koros, W. J. Olefins-selective asymmetric carbon molecular sieve hollow fiber membranes for hybrid membrane-distillation processes for olefin/paraffin separations. *J. Memb. Sci.* **2012**, *423–424*, 314–323.

(9) Motelica, A.; Bruinsma, O. S. L.; Kreiter, R.; Den Exter, M.; Vente, J. F. Membrane retrofit option for paraffin/olefin separation-a technoeconomic evaluation. *Ind. Eng. Chem. Res.* **2012**, *51*, 6977–6986.

(10) Benali, M.; Aydin, B. Ethane/ethylene and propane/propylene separation in hybrid membrane distillation systems: Optimization and economic analysis. *Sep. Purif. Technol.* **2010**, *73*, 377–390.

(11) Koros, W. J.; Lively, R. P. Water and Beyond : Expanding the Spectrum of Large-Scale Energy Efficient Separation Processes. *AIChE J.* **2012**, *58*, 2624–2633.

(12) Koros, W. J. Evolving beyond the thermal age of separation processes: Membranes can lead the way. *AIChE J.* **2004**, *50*, 2326–2334.

(13) Koros, W. J.; Zhang, C. Materials for next-generation molecularly selective synthetic membranes. *Nat. Mater.* **2017**, *16*, 289–297.

(14) Robeson, L. M. Correlation of separation factor versus permeability for polymeric membranes. *J. Memb. Sci.* **1991**, *62*, 165–185.

(15) Robeson, L. M. The upper bound revisited. *J. Memb. Sci.* **2008**, *320*, 390–400.

(16) Freeman, B. D. Basis of Permeability/Selectivity Tradeoff Relations in Polymeric Gas Separation Membranes. *Macromolecules* **1999**, *32*, 375–380.

(17) Chen, C.-C.; Qiu, W.; Miller, S. J.; Koros, W. J. Plasticization-resistant hollow fiber membranes for CO2/CH4 separation based on a thermally crosslinkable polyimide. *J. Memb. Sci.* **2011**, *382*, 212–221.

(18) Qiu, W.; Chen, C.; Xu, L.; Cui, L.; Paul, D. R.; Koros, W. J. Sub-Tg Cross-Linking of a Polyimide Membrane for Enhanced CO2 Plasticization Resistance for Natural Gas Separation. *Macromolecules* **2011**, *44*, 6046–6056.

(19) McKeown, N. B.; Budd, P. M. Polymers of intrinsic microporosity (PIMs): organic materials for membrane separations, heterogeneous catalysis and hydrogen storage. *Chem. Soc. Rev.* **2006**, *35*, 675–683.

(20) Swaidan, R.; Ghanem, B.; Pinnau, I. Fine-Tuned Intrinsically Ultramicroporous Polymers Redefine the Permeability/Selectivity Upper Bounds of Membrane-Based Air and Hydrogen Separations. *ACS Macro Lett.* **2015**, *4*, 947–951.

(21) Ghanem, B. S.; Swaidan, R.; Ma, X.; Litwiller, E.; Pinnau, I. Energy-efficient hydrogen separation by AB-type ladder-polymer molecular sieves. *Adv. Mater.* **2014**, *26*, 6696–6700.

(22) Swaidan, R. J.; Ghanem, B.; Swaidan, R.; Litwiller, E.; Pinnau, I. Pure- and mixed-gas propylene/propane permeation properties of spiro- and triptycene-based microporous polyimides. *J. Memb. Sci.* **2015**, *492*, 116–122.

(23) Salinas, O.; Ma, X.; Litwiller, E.; Pinnau, I. Ethylene/ethane permeation, diffusion and gas sorption properties of carbon molecular sieve membranes derived from the prototype ladder polymer of intrinsic microporosity (PIM-1). *J. Memb. Sci.* **2016**, *504*, 133–140.

(24) Jue, M. L.; Breedveld, V.; Lively, R. P. Defect-free PIM-1 hollow fiber membranes. *J. Memb. Sci.* **2017**, *530*, 33–41.

(25) Caro, J.; Noack, M. Zeolite membranes – Recent developments and progress. *Microporous Mesoporous Mater.* **2008**, *115*, 215–233.

(26) Zong, Z.; Feng, X.; Huang, Y.; Song, Z.; Zhou, R.; Zhou, S. J.; Carreon, M. A.; Yu, M.; Li, S. Highly permeable N2/CH4 separation SAPO-34 membranes synthesized by diluted gels and increased crystallization temperature. *Microporous Mesoporous Mater.* **2016**, *224*, 36–42.

(27) Kwon, H. T.; Jeong, H.-K. In Situ Synthesis of Thin Zeolitic-Imidazolate Framework ZIF-8 Membranes Exhibiting Exceptionally High Propylene/Propane Separation. *J. Am. Chem. Soc.* **2013**, *135*, 10763–10768.

(28) Zhang, C.; Dai, Y.; Johnson, J. R.; Karvan, O.; Koros, W. J. High performance ZIF-8/6FDA-DAM mixed matrix membrane for propylene/propane separations. *J. Memb. Sci.* **2012**, *389*, 34–42.

(29) Bachman, J. E.; Smith, Z. P.; Li, T.; Xu, T.; Long, J. R. Enhanced ethylene separation and plasticization resistance in polymer membranes incorporating metal–organic framework nanocrystals. *Nat. Mater.* **2016**, 1–7.

(30) Dai, Y.; Johnson, J. R.; Karvan, O.; Sholl, D. S.; Koros, W. J. Ultem®/ZIF-8 mixed matrix hollow fiber membranes for CO2/N2 separations. *J. Memb. Sci.* **2012**, *401–402*, 76–82.

(31) Husain, S.; Koros, W. J. Mixed matrix hollow fiber membranes made with modified HSSZ-13 zeolite in polyetherimide polymer matrix for gas separation. *J. Memb. Sci.* **2007**, *288*, 195–207.

(32) Steel, K. M.; Koros, W. J. An investigation of the effects of pyrolysis parameters on gas separation properties of carbon materials. *Carbon.* **2005**, *43*, 1843–1856.

(33) Ning, X.; Koros, W. J. Carbon molecular sieve membranes derived from Matrimid® polyimide for nitrogen/methane separation. *Carbon.* **2014**, *66*, 511–522.

(34) Salinas, O.; Ma, X.; Litwiller, E.; Pinnau, I. High-performance carbon molecular sieve membranes for ethylene/ethane separation derived from an intrinsically microporous polyimide. *J. Memb. Sci.* **2016**, *500*, 115–123.

(35) Ma, X.; Swaidan, R.; Teng, B.; Tan, H.; Salinas, O.; Litwiller, E.; Han, Y.; Pinnau, I. Carbon molecular sieve gas separation membranes based on an intrinsically microporous polyimide precursor. *Carbon.* **2013**, *62*, 88–96.

(36) Tin, P. S.; Chung, T. S.; Kawi, S.; Guiver, M. D. Novel approaches to fabricate carbon molecular sieve membranes based on chemical modified and solvent treated polyimides. *Microporous Mesoporous Mater.* **2004**, *73*, 151–160.

(37) Rungta, M.; Wenz, G. B.; Zhang, C.; Xu, L.; Qiu, W.; Adams, J. S.; Koros, W. J. Carbon molecular sieve structure development and membrane performance relationships. *Carbon.* **2017**, *115*, 237–248.

(38) Xu, L.; Rungta, M.; Hessler, J. V.; Qiu, W.; Brayden, M.; Martinez, M.; Barbay, G.; Koros, W. J. Physical aging in carbon molecular sieve membranes. *Carbon.* **2014**, *80*, 155–166.

(39) Ma, X.; Williams, S.; Wei, X.; Kniep, J.; Lin, Y. S. Propylene/Propane Mixture Separation Characteristics and Stability of Carbon Molecular Sieve Membranes. *Ind. Eng. Chem. Res.* **2015**, *54*, 9824–9831.

CHAPTER 2. THEORY AND BACKGROUND

2.1 Overview

This chapter outlines the essential background knowledge and fundamental theories relevant to this research. The first section describes the currently accepted vision of carbon molecular sieve (CMS) membrane materials, after which a discussion of the fundamental transport theories of gas penetrants through both polymeric and CMS membrane materials will be covered. The last section will cover CMS membrane formation, important synthesis parameters and resulting impacts upon gas transport properties. This chapter provides the foundation necessary for interpretation of the remainder of the thesis.

2.2 Structure of Carbon Molecular Sieve Membranes

Carbon molecular sieve materials are usually formed by the high temperature pyrolysis of polymeric precursors. Specifics pertaining to polymeric precursor selection and resulting CMS properties will be saved for later; however, the discussion that follows is generally accepted to apply to all polymeric-derived CMS materials. The currently accepted view is that of a material comprised of turbostratic plate-like structures that result from the aggregation of entities formed during decomposition of polymeric precursors during the pyrolysis process (*1*, *2*). Figure 2.1 below is a popular representation of a CMS material derived from a hydrocarbon precursor, and serves as a

starting point for discussion of CMS materials derived from precursors of increasing complexity.

Figure 2.1. Schematic of turbostratic representation believed to represent some CMS materials (*2*).

The resulting CMS materials are envisioned to be comprised of a slit-like pore structure (cf. Figure 2.2) consisting of a distribution of larger micropores (7-20 Å) connected by a similar distribution of smaller ultramicropore (<7 Å) windows (*1*, *3–6*). The combination of micropores and ultramicropores result in CMS materials having high productivity, with exquisite size and shape selectivity for a variety of separations. Making a connection between this representation and the bimodal distribution of pores in Figure 2.2 and a more chemically-relevant structure such as that in Figure 2.1 is desirable—but challenging. It is reasonable to connect these two representations by attributing ultramicropores to defects *within the plates* shown in Figure 2.1, while attributing the micropores to the spaces *between the plates*. Of course, the details of the plate structure in such a picture will be different in a simpler hydrocarbon versus a CMS derived from a precursor of increased chemical complexity (e.g. polyimide); however, the general concepts and features should be similar.

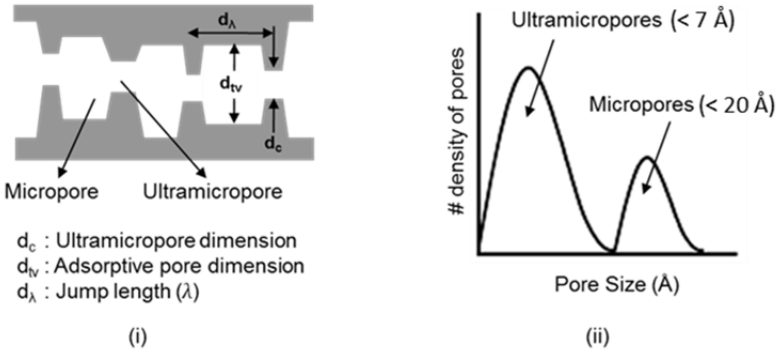

Figure 2.2. (i) Idealized "slit-like" representation of CMS materials and (ii) bimodal pore size distribution (*7*).

2.3 Fundamentals of Gas Transport

Membranes, in their simplest form, act as a selective barrier between two phases. Gas separation membranes involve contacting a feed gas to the upstream side, where one (or more) constituents of the feed passes through to the downstream side of the membrane forming a permeate stream. The retained species of the feed gas exits the upstream side of module as the retentate stream. Transport of a specific penetrant across a membrane depends upon many factors, involving characteristics of both the membrane material and the penetrant itself. Several mechanisms are associated with describing the transport of penetrants across a membrane surface: i) Knudsen diffusion; ii) selective surface adsorption with surface diffusion; iii) molecular sieving; iv) sorption-diffusion (*8*, *9*). A schematic of these four types of transport is reproduced below in Figure 2.3.

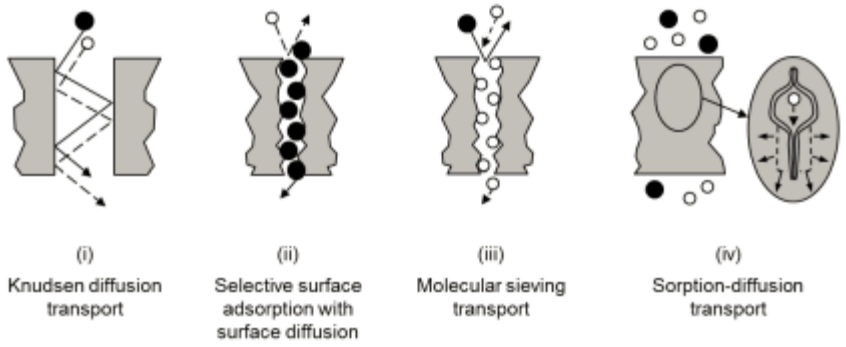

Figure 2.3. Schematic representation of common transport mechanisms within selective membrane materials (*8*, *9*).

While the details pertaining to mechanisms i-iii are of interest to research of porous membranes, they do not accurately describe penetrant transport through dense, non-porous polymeric or CMS materials which are at the center of this study. For both the polymeric precursor and the resulting CMS membranes within this work, the sorption-diffusion mechanism most accurately describes gas transport through these materials.

Sorption-diffusion transport of a penetrant across a dense, non-porous membrane occurs first by a penetrant sorbing to the high chemical potential side (upstream) of the membrane followed by diffusion through the material via a chemical potential gradient, and finally desorbing on the low chemical potential (downstream) side of the membrane. The sorption-diffusion model assumes equilibrium at both of the gas-membrane interfaces, allowing for a continuous chemical potential gradient throughout the membrane (*10*). Additionally, this model assumes a constant pressure, equal to the applied upstream pressure, throughout the membrane removing any pressure gradient. The underlying assumptions of the sorption-diffusion model are depicted in Figure 2.4 below.

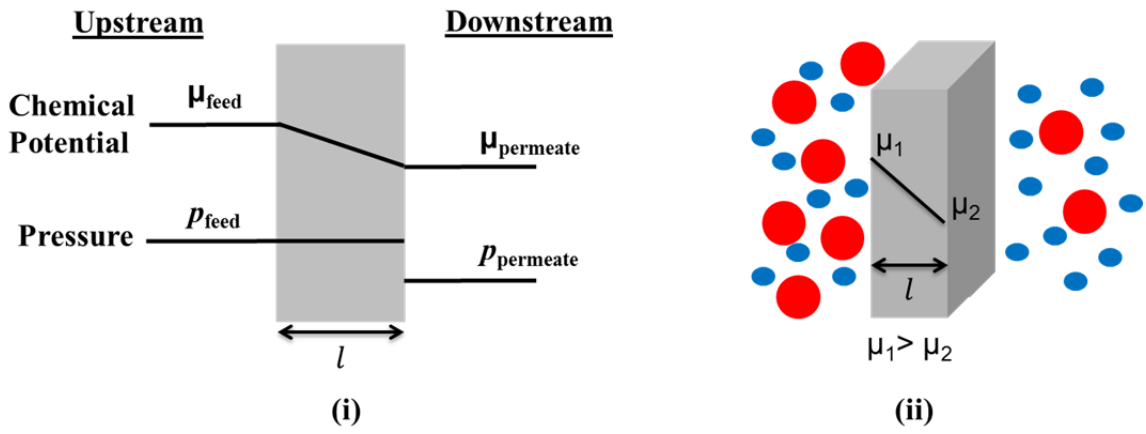

Figure 2.4. Schematic of solution-diffusion across a membrane, (i) Representation of underlying model assumptions, (ii) schematic of separation of two different penetrants across membrane via solution-diffusion model.

Permeability and selectivity, respectively, describe the productivity and separation efficiency of a membrane material. The permeability of penetrant A through a membrane is expressed by Equation 2.1:

$$P_A = \frac{N_A l}{\Delta p_A} \tag{2.1}$$

where N_A is the steady-state flux of penetrant A through a membrane of thickness l caused by partial pressure difference (Δp_A), or more precisely fugacity difference (Δf_A) of component A. Permeability may be expressed in various units, but is most commonly reported in the units of Barrer, where:

$$1 \text{ Barrer} = 10^{-10} \frac{\text{cc(STP)} \cdot \text{cm}}{\text{cm}^2 \cdot \text{s} \cdot \text{cmHg}} = 0.33 \text{ x } 10^{-15} \frac{\text{mol} \cdot \text{m}}{\text{m}^2 \cdot \text{s} \cdot \text{Pa}}$$

While membrane thickness measurements for dense, flat-sheet films are straightforward, determination of the separation layer l in asymmetric hollow fiber membranes usually cannot be unambiguously determined. In this case, membrane productivity is described

by permeance, given by Equation 2.2, which is simply the partial pressure difference normalized steady-state flux.

$$\frac{P_A}{l} = \frac{N_A}{\Delta p_A} \tag{2.2}$$

Permeances values are commonly expressed as Gas Permeation Units (GPU), where:

$$1 \text{ GPU} = 10^{-6} \ \frac{\text{cc(STP)}}{\text{cm}^2 \cdot \text{s} \cdot \text{cmHg}} = 3.35 \text{ x } 10^{-10} \ \frac{\text{mol}}{\text{m}^2 \cdot \text{s} \cdot \text{Pa}}$$

Based on the sorption-diffusion model, the permeability of a component (P_A) can be written as the product of the average kinetic (diffusivity, $\overline{D}_A$) and thermodynamic (sorption, $\overline{\mathbb{S}}_A$) coefficients, as shown in Equation 2.3:

$$P_A = \overline{D}_A \times \overline{\mathbb{S}}_A \tag{2.3}$$

Application of Fick's 1st Law, neglecting bulk flow, allows for the following analysis:

$$\overline{D}_A = \frac{\int_{C_{A,1}}^{C_{A,2}} D_A(C_A) dC_A}{\int_{C_{A,1}}^{C_{A,2}} dC_A} \tag{2.4}$$

$$\overline{\mathbb{S}}_A = \frac{C_{A,2} - C_{A,1}}{p_{A,2} - p_{A,1}} \tag{2.5}$$

where $\overline{D}_A$ and $\overline{\mathbb{S}}_A$ are the average transport diffusivity and sorption coefficient of penetrant A in the membrane, $C_{A,1}$ and $C_{A,2}$ are the concentration of penetrant A in the downstream and upstream side of the membrane, and $p_{A,1}$ and $p_{A,2}$ are the partial pressure of penetrant A in the downstream and upstream, respectively.

The separation efficiency, or ideal permselectivity, of a membrane with negligible downstream pressure (i.e. vacuum) is represented by the ratio of the pure component permeabilities or permeances:

$$\alpha_{A/B} = \frac{P_A}{P_B} = \frac{\left(P/l\right)_A}{\left(P/l\right)_B} \tag{2.6}$$

where in this case of separating arbitrary components A and B, A would be the faster permeating species.

When permeating a binary mixture of both penetrants A and B, the separation factor is:

$$\alpha_{A/B} = \frac{y_A / y_B}{x_A / x_B} \tag{2.7}$$

where the mole fractions y and x are the downstream (permeate) and upstream (feed) sides of the membrane.

Combination of Equations 2.3 and 2.6 allows for the permselectivity to be written as a product of the diffusion selectivity α_D and sorption selectivity α_S.

$$\alpha_{A/B} = \frac{\overline{D}_A}{\overline{D}_B} \times \frac{\overline{\mathbb{S}}_A}{\overline{\mathbb{S}}_B} = \alpha_D \times \alpha_S \tag{2.8}$$

Equation 2.8 shows that the membrane efficiency is dependent upon both kinetic and thermodynamic factors for a given separation. Thus, tuning membrane materials can be approached from two different routes, with the goals of optimizing both the kinetic and thermodynamic aspects of a separation material for a given separation.

2.3.1 Sorption

For materials governed by the sorption-diffusion model, a penetrant must first sorb at the high pressure (chemical potential) side of the membrane before it can diffuse across the membrane. The average sorption coefficient ($\bar{\mathbb{S}}_A$) is the pressure normalized concentration of a penetrant at an equilibrium pressure, and is strongly dependent upon the condensability of the penetrant and its interaction with the membrane surface, and can be written as:

$$\bar{\mathbb{S}}_A = \frac{C_A}{p_A} \tag{2.9}$$

where C_A is the equilibrium uptake of penetrant A by the material and p_A is the partial pressure of A.

For molecular sieving materials such as zeolites and CMS, with a finite number of available sorption sites, the Langmuir isotherm (Equation 2.10) is used to describe gas sorption where C'_{HA} is the Langmuir hole filling capacity, b_A is the Langmuir affinity constant, and p_A is the partial pressure of penetrant A, respectively (*11*, *12*).

$$C_A = \frac{C'_{HA} b_A p_A}{1 + b_A p_A} \tag{2.10}$$

It is generally believed that the majority of penetrant molecules sorb into the larger micropores within CMS materials (*13*). This is due to micropores having an appreciably larger capacity for gas sorption, when compared to the ultramicropores which are envisioned to comprise edges of aromatic plates, as was mentioned in Section 2.2. Additionally, the gas molecules sorbed in the micropores will reside in a lower energy

state, due to the reduction of the repulsive forces compared to a molecule residing in the tighter ultramicropore window.

For molecular sieving materials, with high surface areas and large sorption capacities like CMS, transport properties can become concentration dependent at high sorption loadings. In situations like this, it is convenient to express a fractional-site factor (θ_A) based on the Langmuir isotherm, to account for the uptake of the penetrant within the material, and can be described as:

$$\theta_A = \frac{C_A}{C'_{HA}} = \frac{b_A p_A}{1 + b_A p_A} \tag{2.11}$$

2.3.2 Diffusion

With respect to the sorption-diffusion mechanism, after initial sorption into the material the penetrant of interest diffuses across the membrane material due to a concentration (chemical potential) gradient. Diffusion of a penetrant through an isotropic medium can be described by the random walk theory in Equation 2.12, wherein a penetrant executes a series of random jumps from site to site. Here f_A and λ_A are the random walk jumping frequency, and jump length, respectively (*14*). The 1/6 factor relates to the equal chance for a diffusive jump to occur in a given direction within an isotropic medium.

$$D_A = \frac{f_A \lambda_A^2}{6} \tag{2.12}$$

Diffusion in polymers is envisioned to occur by an activated process wherein a 'gap' within the polymer matrix is created due to random, thermally driven segmental fluctuations. When a large enough gap occurs adjacent to a penetrant sorbed within the

polymer matrix the penetrant can execute a diffusional jump, as shown schematically in Figure 2.5 – (i) below. After a penetrant executes a diffusional jump, the volume previously occupied will be redistributed within the polymer matrix by segmental motions. The size and frequency of diffusional jumps within polymeric materials is dependent upon both the properties of the polymer (chain stiffness, chain packing, etc.) as well as specific properties of the penetrant of interest (size, condensability).

Similarly, sorption-diffusion in molecular sieving materials is typically described as an activated process, wherein the penetrant of interest is similar in size to that of the pore for which it must transport through (*12*). In the case of CMS materials, diffusion of a penetrant is envisioned to occur by an activated jump from a sorbed state in one micropore, through an ultramicropore window, to an adjacent micropore as shown in Figure 2.5 – (ii) (*12*, *13*, *15*). In order for a successful diffusional jump to occur, the penetrant must acquire sufficient energy to overcome the repulsive force between itself and the rigid CMS ultramicropore surface, known as the "energetic selectivity" (*13*, *15*). Unlike flexible polymer materials, the rigid CMS ultramicropore windows can also discriminate between differently shaped, yet similarly sized materials by restriction of various degrees of rotational and/or vibrational freedom during the activated diffusion process, which gives rise to "entropic selectivity" (*15*, *16*). While entropic selectivity is not unique to CMS materials, it is one of the factors contributing to their impressive performance for challenging gas separations. Small changes in the ultramicropore dimension allow for precise control of the size selective sieving nature of the CMS materials, allowing for truly engineering the separation performance of these materials.

Derivation and further description of the entropic selectivity within CMS materials will be discussed further in Section 2.3.4.

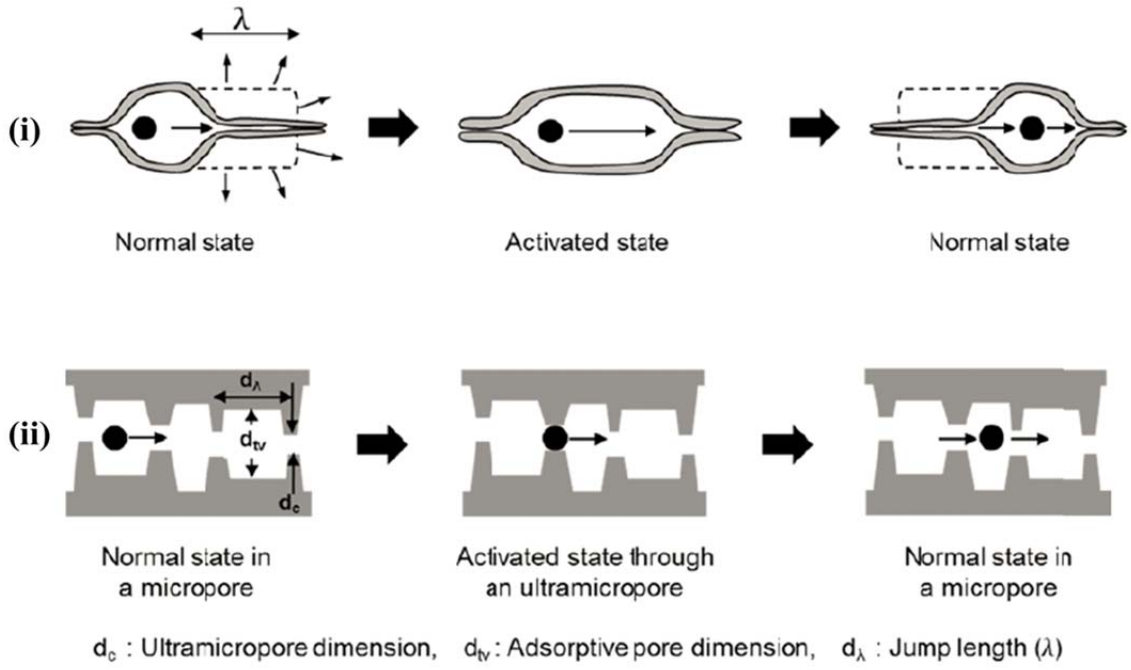

Figure 2.5. Schematic depictions of activated diffusion within (i) polymers, (ii) CMS materials (*16*).

The average transport diffusivity ($\overline{D}_A$) is commonly used as a measure of penetrant diffusivity through a CMS material. Since the local transport (Fickian) diffusivity D_A tends to be concentration dependent, it is best to characterize molecular sieving behavior based on a thermodynamically corrected (Maxwell-Stefan) diffusivity $Đ_A$ by accounting for gas loading (*12*, *17*). The Fickian diffusion coefficient, D_A, can be described by the product of a thermodynamically corrected diffusivity ($Đ_A$) and a thermodynamic correction factor (d ln$p$/ d ln$C$) accounting for the nonlinear relationship between chemical activity and concentration of penetrant gases, as shown below (*12*):

$$D_A = Đ_A \frac{d \ln p_A}{d \ln C_A} \tag{2.13}$$

Determination of the C_A in the thermodynamic correction factor above is performed by fitting gas sorption isotherms for CMS materials with the Langmuir model, as was described in Section 2.3.1. Using Equations 2.10 and 2.11, one can show that:

$$\frac{d \ln p_A}{d \ln C_A} = \frac{1}{1-\theta_A} \tag{2.14}$$

Combination of the Equations 2.13 and 2.14 allows for Equation 2.15 to accurately describe the method for determining the Maxwell-Stefan corrected diffusivity for CMS materials used in this and other work.

$$D_A = \frac{Đ_A}{1-\theta_A} \tag{2.15}$$

Thus, when the membrane downstream is at vacuum (C_A = 0), the average transport diffusivity ($\overline{D}_A$) can be correlated to the corrected diffusivity ($Đ_A$) and fractional site saturation (θ_A) as follows:

$$\overline{D}_A = \frac{\int_{C_A}^{0} D_A dC_A}{\int_{C_A}^{0} dC_A} = \frac{Đ_A}{\theta_A} \ln\left(\frac{1}{1-\theta_A}\right) \tag{2.16}$$

A detailed derivation of the Equation 2.16 can be found in (*12*, *16*, *17*) .

2.3.3 Temperature Effects of Transport Processes

As previously described, diffusion of a penetrant within CMS and polymeric materials occurs via an activated process. The diffusion coefficient of a penetrant within a given material increases with increasing temperature following an Arrhenius-type trend, provided in Equation 2.17 below. Conversely, equilibrium sorption of a penetrant within CMS and polymeric materials typically decreases with increasing temperature, following a van't Hoff relationship, provided in Equation 2.18 below:

$$D = D_0 \exp\left(\frac{-E_D}{RT}\right) \tag{2.17}$$

$$\mathbb{S} = \mathbb{S}_0 \exp\left(\frac{-H_{\mathbb{S}}}{RT}\right) \tag{2.18}$$

where D_0 and $\mathbb{S}_0$ are the diffusion and sorption pre-exponential factors, respectively, E_D is the activation energy of diffusion, $H_{\mathbb{S}}$ is the enthalpy of sorption, R is the universal gas constant and T is absolute temperature. Using Equations 2.17 and 2.18 allows for expression of the temperature dependence of permeation, via substitution into Equation 2.3, yielding an Arrhenius-type dependence shown in Equation 2.19:

$$P_A = \overline{D}_A \times \overline{\mathbb{S}}_A = D_0 \exp\left(\frac{-\Delta E_D}{RT}\right) \times \mathbb{S}_0 \exp\left(\frac{-H_{\mathbb{S}}}{RT}\right) = P_0 \exp\left(\frac{-E_P}{RT}\right) \tag{2.19}$$

$$P_0 = D_0 \times \mathbb{S}_0 \tag{2.20}$$

$$E_P = E_D + H_{\mathbb{S}} \tag{2.21}$$

where P_0 and E_P are the permeability pre-exponential factor and activation energy of permeation, respectively.

Values of permeation activation energy (E_P) are typically positive for most penetrants; however, a large negative H_S (which is possible with highly condensable components) can outweigh the positive value of E_D leading to an overall decrease in permeability with increasing temperature.

2.3.4 Diffusional Selectivity of CMS Materials: Entropic and Energetic Contributions

Recalling Equation 2.8, the overall permselectivity of a material can be described as a product of the diffusion and sorption selectivity. Sorption selectivity captures the thermodynamic aspects of a separation, which depend primarily upon penetrant condensability and attraction with the material of interest. Diffusional selectivity captures kinetic aspects of a separation, and is primarily a function of penetrant shape and size. Application of transition state theory to diffusion highlights the importance of dimensions of penetrants A and B upon membrane material selectivity. Specifically, the diffusion selectivity is dependent upon a quadratic ratio of jump lengths (λ) and an exponential difference in free energy of activation, $\Delta G^*_{D,A-B}$ (*15*, *18*, *19*):

$$\frac{\overline{D}_A}{\overline{D}_B} = \frac{\lambda_A^2}{\lambda_B^2} \exp\left(\frac{\Delta G^*_{D,A-B}}{RT} \right) \tag{2.22}$$

In Equation 2.22 $\Delta G^*_{D,A-B} = \Delta H^*_{D,A-B} - T\Delta S^*_{D,A-B}$, with $\Delta H^*_{D,A-B}$ and $\Delta S^*_{D,A-B}$ representing the difference in diffusion transition enthalpy (H^*) and entropy (S^*) for component A versus B, and R and T are the universal gas constant and absolute temperature,

respectively. Furthermore, the difference in diffusional transition enthalpy can be expanded as $\Delta H^*_{D,A-B} = \Delta E^*_{D,A-B} + \Delta PV^*_{D,A-B}$ where $\Delta E^*_{D,A-B}$ is the difference in diffusion transition activation energy (E^*) and $\Delta PV^*_{D,A-B}$ represents the difference in transition pressure and volume. As diffusion of a penetrant is accompanied by a negligible change in volume ($\Delta V^* \approx 0$) (*20*), it is possible to express Equation 2.22 as:

$$\frac{\overline{D}_A}{\overline{D}_B} = \frac{\lambda_A^2}{\lambda_B^2} \underbrace{\exp\left(\frac{\Delta S^*_{D,A-B}}{R}\right)}_{\text{Entropic}} \underbrace{\exp\left(\frac{-\Delta E^*_{D,A-B}}{RT}\right)}_{\text{Energetic}} \tag{2.23}$$

Equation 2.23 shows that diffusional selectivity of CMS materials can be factored into "energetic" and "entropic" contributions. The energetic contribution arises from the transition activation energy of diffusion (E^*_D) which is a measure of energy a penetrant must overcome in order to make a successful diffusive jump to an adjacent micropore, passing through an ultramicropore window. Entropic selectivity arises from the rigid ultramicropore windows, where transition entropy (S^*_D) controls size and shape discrimination between penetrants A and B.

An alternative transition state theory representation of the diffusion coefficient is provided in Equation 2.24 below (*20*):

$$D = \lambda^2 \frac{kT}{h} \frac{F^*}{F} \exp\left(\frac{-E^*_D}{RT}\right) \tag{2.24}$$

where λ is the average diffusion jump length, k is Boltzmann's constant, h is Planck's constant, F^* is the partition function of a penetrant in the transition state, F is the

partition function of the same penetrant in the ground state, and E_D^* is the transition activation energy of diffusion. The normal and transition (activated) states for polymeric and CMS membranes are illustrated in Figure 2.5. Considering separating penetrants of similar size (e.g. O_2/N_2, C_2H_4/C_2H_6) the average diffusive jump length (λ) will be similar, allowing for an alternative representation of entropic selectivity as:

$$\exp\left(\frac{\Delta S_{D,A-B}^*}{R}\right) = \frac{(F^*/F)_A}{(F^*/F)_B} \tag{2.25}$$

The partition function of a penetrant F is the product of the possible translational, rotational, vibrational, and electronic states a penetrant can occupy.

$$F = F_{trans} \cdot F_{rot} \cdot F_{vib} \cdot F_{elec} \tag{2.26}$$

In the case of CMS membranes, a gas molecule sorbed in the micropore is in the normal state, and a gas molecule passing through the ultramicropore window is in the transition state. The limiting dimensions of an ultramicropore window approaches the molecular size of a gas penetrant, and are analogous to the selective openings in zeolite and metal organic framework (MOF) materials. As a penetrant passes through an ultramicropore, certain degrees of rotational, translational, and vibration degrees of freedom will be restricted, allowing for subtle discriminations between similarly sized molecules. This enables CMS materials to have high entropic selectivities, compared to flexible-chain polymeric materials making them especially useful for separating penetrants that very little difference in size and shape (e.g. O_2/N_2, C_2H_4/C_2H_6 and C_3H_6/C_3H_8), having been highlighted before for select gas pairs (*15*, *21–23*).

2.4 Factors Controlling Carbon Molecular Sieve Structure and Performance

2.4.1 Polymeric Precursor

The choice of polymeric precursor is one of the most important factors in CMS membrane synthesis. A variety of polymeric materials have been utilized as precursors for CMS membranes including, but not limited to: cellulosic derivatives (*24*, *25*), poly(vinyilidine)-based polymers (*26*, *27*), phenolic resins (*28*), polyfurfuryl alcohols (*6*), polyimides (*16*, *29–31*), and additionally a newer class termed polymers of intrinsic microporosity (PIMs) (*32*, *33*). Despite the wide variety of polymeric precursors available, polyimides are among the most popular due to their high glass transition temperature, ease of processability, attractive mechanical properties and attractive gas separation performance (*34*).

Properties of polymeric precursors that have important implications upon the resulting CMS membrane material include: chemical structure, glass transition (T_g) and degradation (T_d) temperatures, and fractional free volume (FFV). Many studies have investigated the differences in polymeric structure by comparing performance of CMS membranes derived from two polyimide precursors: BTDA-DAPI (tradename Matrimid®) and a custom synthesized 6FDA:BPDA-DAM(1:1), chemical structures of which are reproduced below (*13*, *16*).

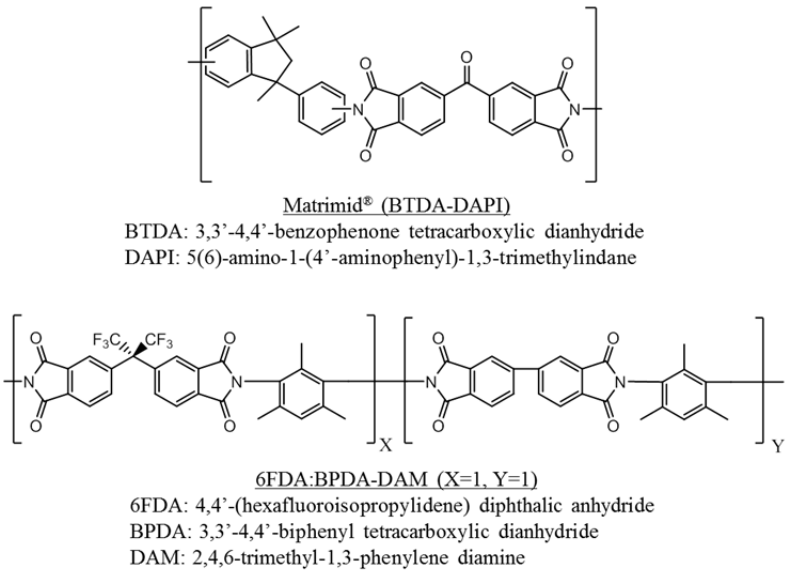

Figure 2.6. Chemical structure of Matrimid® and 6FDA:BPDA-DAM(1:1) polyimide precursors.

The most obvious distinguishing factor between these two polyimides lies in the bulky CF_3 groups of the 6FDA-unit of the second polyimide. These bulky CF_3 groups inhibit polymer chain packing, leading to higher FFV of 0.145, when compared to a FFV of 0.110 for Matrimid®. Regardless of the gas pair or pyrolysis temperature, CMS membranes derived under the same conditions from the 6FDA:BPDA-DAM(1:1) precursor exhibit higher permeabilities and lower selectivities, when compared to the Matrimid® derived CMS membranes (*7*, *22*). This performance is due, in part, to the larger pore volume within the CMS derived from the 6FDA:BPDA-DAM(1:1) precursor created by evolution of the bulky CF_3 groups as HF and HCF_3 during the pyrolysis process (*35*, *36*).

These facts motivated more recent work on 6FDA-based precursors of increasing complexity (*31*), with hopes of refining the structure-property relationships between polymeric precursors and resulting CMS membranes. The detailed characterization in this

study highlighted the disconnect between precursor physical properties (i.e. FFV) and resulting CMS performance. This fact should not be surprising, as there are many physical properties to consider during the pyrolysis of a polymer to a resulting CMS material.

Other important physical parameters for polymeric precursors of CMS membranes are both the glass transition (T_g) and decomposition (T_d) temperatures. While polyimides, a preferred class of CMS precursor polymers, exhibit high thermal stability there is a period of time during the pyrolysis process where the material will be above the glass transition but below the degradation temperature. While this does not matter for the formation of dense film membranes for fundamental studies, it has special implications during the pyrolysis of asymmetric hollow fiber polymeric precursors – the preferred morphology for industrial-scale gas separations, as will be discussed later. For example, the glass transition and degradation temperatures of Matrimid® are 318 °C and 490 °C, respectively. When asymmetric Matrimid® hollow fibers are pyrolyzed to temperatures above 500 °C the attractive asymmetric morphology is lost due to substructure collapse, resulting in completely dense hollow fibers with very low permeation rates (*37*). Contrasting with the pyrolysis of asymmetric hollow fibers of 6FDA:BPDA-DAM(1:1), which has glass and degradation temperatures of 424 °C and 492 °C, respectively, substructure collapse occurs; however, a *significant amount of asymmetry is retained* at pyrolysis temperatures above 500 °C. Substructure collapse occurs when the temperature surpasses the T_g as polymer chains gain enough thermal energy to enable long-range segmental mobility, resulting in collapse of the porous substructure before the polymer degradation begins. Therefore, from a purely thermal stability argument, polymeric

precursors with higher T_g, or preferably a smaller difference of (T_d-T_g) (e.g. 6FDA:BPDA-DAM) will retain most, *but not all*, of the asymmetry desired for industrial-scalable gas separation materials. However, as will be discussed later there are pre-treatment methods for polymeric materials that can arrest substructure collapse during pyrolysis.

The above discussions, while not exhaustive, highlight some of the important factors that must be considered when picking a polymer precursor for formation of CMS membranes. While some characteristics of the polymeric precursor are retained during transformation to CMS material as was mentioned before, *this is not always the case*. The connection between polymeric structure and resultant CMS membrane performance is non-trivial, and further attempts to establish this are considered further in Chapter 6.

2.4.2 Precursor Pretreatment

In addition to precursor material selection, pretreatment of the polymers can have important implications upon the resulting CMS membrane performance. One of the most common pretreatment techniques is pre-oxidation of the polymer, performed by heating the material to a desired temperature in air (or other oxidizing environment). It is thought that this pre-oxidation step aids in polymer chain stabilization, leading to an increased micropore volume in corresponding CMS membrane materials (*38*). Additionally, it can be used as a tool to prevent the aforementioned polymer chain softening and collapse by crosslinking, which aids in retention of asymmetry in resulting CMS hollow fibers (*39*, *40*).

Bhuwania *et. al.* recently developed a novel method for prevention of substructure collapse in asymmetric polymeric hollow fibers utilizing a pre-pyrolysis reaction between an organic-alkoxy silane (vinyltrimethylsilane) and moisture, forming a crosslinked sol-gel on the precursor (*41*). The sol-gel coats the polymer structure in a porous organo-silica layer, restricting polymer chain softening and flow that occurs when the material is heated above the T_g, but below T_d. Comparing treated to untreated polymer precursors, the treatment results in a 5-6 fold reduction in apparent membrane separation layer thickness, allowing for retention of the attractive asymmetric morphology (and associated high productivity) for the resulting CMS membranes.

Depending upon the chemical moieties contained within the precursor material, chemical modification of the polymers may be conducted in order to enhance the resulting CMS membrane performance. 6FDA-based copolyimides containing a DABA (3,5-diaminobenzoic acid) unit result in a pendant carboxylic acid group off of the polymer backbone, where thermally activated (sub-T_g) decarboxylation can result in covalent crosslinking between adjacent polymer chains leading to increased membrane productivity and stability, as developed by Qiu *et. al.* (*42*). This strategy was deployed on a novel 6FDA-DETDA:DABA(3:2) copolyimide, where prior to pyrolysis the polymer films were cross-linked at 370 ^{o}C for 90 minutes (*43*). The resulting pre-crosslinked CMS membranes displayed higher permeabilities, owing to a higher micropore volume due to the packing disruptions and microvoids created during the crosslinking reaction.

Chemical crosslinking agents have also been a method utilized to prevent substructure collapse in polymeric precursors for CMS membranes. A recent example

provided by Koh *et. al.* demonstrated that crosslinking PVDF with para-xylxylenediamine resulted in retention of the asymmetric structure after pyrolysis (*27*). While the membranes produced by Koh *et. al.* were for organic solvent reverse osmosis, similar techniques had previously been applied to gas separations by Tin *et. al.* where Matrimid® was crosslinked with the same para-xylxylenediamine (*44*). This study reported that CMS membrane permeation decreased with increasing crosslinking density, contrary to the results of the previously mentioned pre-crosslinked 6FDA-DETDA:DABA(3:2) derived CMS materials, further highlighting that techniques applied to one CMS may not display the same characteristics a CMS derived from a different polymeric precursor.

Within this current study, polymer pretreatment methods were not investigated. The goals of this work were to examine alternative methods to alter the resulting performance of CMS membranes through either modification of the pyrolysis process or development of novel post-synthesis treatments. Addition of pre-treatment methods would have increased the experimental complexity, as well as additional variables within the study.

2.4.3 The Pyrolysis Process

Pyrolysis refers to the high temperature heat treatment of a material under an inert atmosphere. Aside from the precursor selection, the pyrolysis process itself has arguably the most significant impact upon the resulting CMS structure and performance as a gas separation material. A general pyrolysis protocol, which will be described in detail in Chapter 3, is represented by Figure 2.7 showing three distinct phases: ramp, soak, and

cooling. The most important pyrolysis parameters are: final pyrolysis temperature, ramp rate, pyrolysis soak time, and pyrolysis atmosphere.

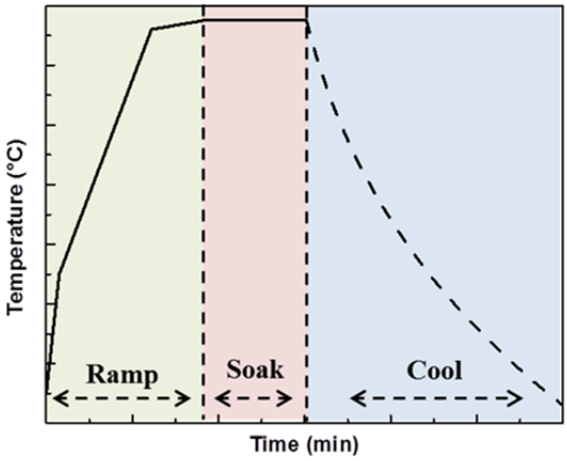

Figure 2.7. Typical pyrolysis protocol used for CMS formation within this work.

2.4.3.1 Effect of Pyrolysis Ramp Rate

In the context of the transformation of a random coil polymer precursor to the disrupted plate-like structure with slit-like ultramicropores, like that in Figure 2.2, the ramp rate controls the evolution rate of polymer degradation by-products, as well as the total pyrolysis time during the formation of a CMS material. These two factors can have significant impacts upon the pore structure formed, and the resulting performance of the CMS membranes. Considering the precursor materials Matrimid® and 6FDA:BPDA-DAM(1:1) in Figure 2.6, important pyrolysis by-products include CO_2, CO, and H_2 as well as CF_3H and HF for the fluorinated precursor (*36*). During the ramping process, once the temperature has passed the T_d of the polymer, aromatization begins to occur. Considering pathways consistent with loss of the previously mentioned by-products

suggests the possible formation of a rigid, highly aromatic strand as shown in Figure 2.8 in the context of a 6FDA:BDPA-DAM(1:1) precursor. Specific details of the strand structure, are purely hypothetical at this point and will be further discussed in Chapter 6, however the strand structure is not necessary for the high level CMS formation discussion that is being presented here.

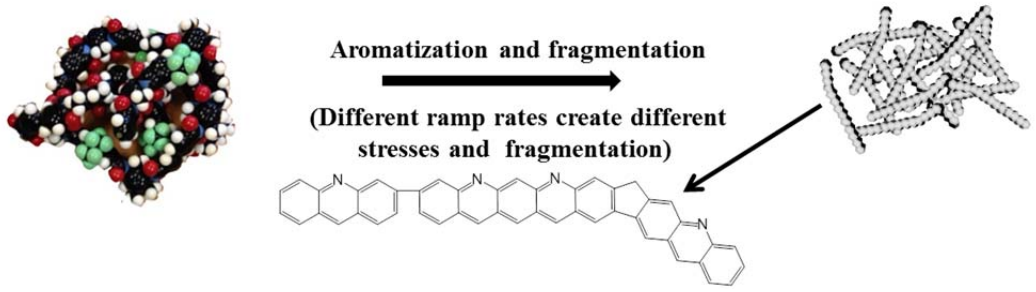

Figure 2.8. Fragmentation of polymeric chain during pyrolysis ramping process. Shown for pyrolysis of 6FDA:BPDA-DAM(1:1) but representative of degradation of other polyimide precursors.

Pyrolysis of a precursor consisting of entangled polymeric chains will undergo aromatization and linearization during the ramping phase of the pyrolysis process. It is envisioned that during this aromatization process, localized stresses will cause scissions along the backbone to form the strand-like structures. Increasing the ramp rate may result in increased stresses upon the polymer chain, resulting in increased scission and fragmentation rates forming smaller strands. Packing of these strands into plates, reminiscent to that of Figure 2.1, presents a solid state packing issue that will be addressed in detail in Chapter 6.

Considering an earlier study performed by Suda and Haraya (*29*), increased ramp rates between 1.33 - 13.3 ºC/min for CMS membranes derived at 1000 ºC from Kapton®

supports the previous strand formation argument. In this study, it was found that for the gases of interest (He, H_2, CO_2, O_2, and N_2), permeability increased with increasing ramp rate. These results attributed the slower ramp rate to formation of smaller pores within the CMS structure, consistent with the argument that slower ramp rates lead to larger strands that may enable closer packing resulting in tighter pore structures.

2.4.3.2 Pyrolysis Temperature

The final pyrolysis temperature is one of the most important parameters controlling the performance of a resulting CMS membrane. It refers to the maximum temperature that the material is heated to during the pyrolysis process. The pyrolysis temperature is chosen to lie above the precursor decomposition temperature, but below graphitization temperature (*1*), and typically ranges from ~500 – 1000 °C in the current literature. While there is still a large gap in fundamental understanding of the transformation of a high molecular weight polymeric precursor and the resulting CMS material, the general trend of increasing pyrolysis temperature resulting in a tighter, more compact pore structure holds. This tighter structure tends to yield less permeable, albeit more selective membranes.

A detailed study of the pyrolysis conditions and resulting performance of Kapton® derived CMS membrane material highlights the relationship between final pyrolysis temperature and gas permeation performance (*29*). Using final pyrolysis temperatures of 600, 800 and 1000 °C and performing permeation tests using He, H_2, CO_2, O_2, and N_2 it was shown that as final pyrolysis temperature increased, the permeability of all components decreased, meanwhile the permselectivity increased. Utilizing sorption characterization techniques, it was also shown that as the final pyrolysis temperature

increased, pore volumes and sizes of the resulting CMS materials decreased. The measured pore size distributions of these materials yielded a sharper distribution as pyrolysis temperature increased.

In the context of the precursors shown in Figure 2.6, a detailed study by Steel and Koros investigated the effects of final pyrolysis temperature on O_2/N_2, CO_2/CH_4, and C_3H_6/C_3H_8 gas separations (*7*, *45*). Similar trends for the O_2/N_2 and CO_2/CH_4 separations were seen when going from 550 °C to 800 °C final pyrolysis temperatures: as final temperature increased, permeability of the fast gases decreased while the permselectivity increased, placing the performance of these CMS materials well past their respective polymer precursor. However, this trend was not seen for the C_3H_6/C_3H_8 separation as CMS membranes from both precursors pyrolyzed at 800 °C displayed performance lower than their polymeric precursors. For the C_3H_6/C_3H_8 separation, Matrimid® derived CMS membranes 500 °C final pyrolysis temperature was found to have the highest performance, whereas the highest performance for CMS membranes derived from 6FDA:BPDA-DAM(1:1) was found to be at 550 °C final temperature. Similar to the previously mentioned study, investigation of these materials via porosity measurements showed a tightening of the size selective ultramicropores (< 7 Å) with increasing pyrolysis temperatures.

The above examples clearly highlight the importance of the final pyrolysis temperature upon the resulting CMS membrane performance. Additionally, CMS materials pyrolyzed under the same conditions but derived from different precursors can have drastically different results, which should not be surprising considering the complex degradation processes that occur during the pyrolysis process.

2.4.3.3 Pyrolysis Soak Time

Upon reaching the final pyrolysis temperature an extended soak typically occurs to complete the pyrolysis process. This thermal soak is thought of as a fine-tuning process, allowing minor changes within the CMS structure. In the context of the rigid, aromatic strands formed during the temperature ramp step (cf. Figure 2.8) it is envisioned that during the high temperature thermal soak, mobility of these strands will be high, allowing for rearrangement to form plate-like structures similar to Figure 2.1. Extended times at this high temperature will allow for tighter structures to be formed, reducing pore sizes and leading to lower permeability of penetrants.

The influence of pyrolysis soak time upon CMS membranes derived from Matrimid® and 6FDA:BPDA-DAM(1:1) was previously investigated by Steel and Koros (*7*), wherein CMS membranes formed at 550 and 800 °C were subject to 2 and 8 hour soaks at the final pyrolysis temperature. In the case of O_2, N_2, CO_2, and CH_4 regardless of precursor or formation temperature, all CMS membranes thermally soaked for 8 hours displayed a reduced permeability coupled with an increased selectivity, when compared to a 2 hour soak. Considering Matrimid® derived CMS membranes at 800 °C for the O_2/N_2 separation, increasing the soak time from 2 hours to 8 hours results in an order of magnitude drop in O_2 permeability and a slight increase in O_2/N_2 selectivity. Whereas, utilizing the same CMS formation conditions with 6FDA:BPDA-DAM(1:1) as the precursor, increasing the soak time from 2 to 8 hours had almost negligible effect on both O_2 permeability and O_2/N_2 selectivity. While the generic trends of increasing soak time leading to a tighter, more selective CMS pore structure hold, these findings suggest that

the effect of soak time depends greatly upon the gas pair, precursor, and final pyrolysis temperature investigated.

2.4.3.4 Pyrolysis Atmosphere

The pyrolysis atmosphere must be controlled in order to prevent unwanted degradation of the polymer precursor or resulting CMS membrane material. Pyrolysis of polymeric precursors is performed under vacuum or inert environments. Geiszler and Koros conducted a detailed study of the effects of the pyrolysis atmosphere upon resulting CMS membranes formed from asymmetric 6FDA:BPDA-DAM(1:1) hollow fibers (*46*). In this study they examined vacuum pyrolysis with an average vacuum level of 0.02-0.03 Torr, as well as argon and helium atmospheres with purge rates of 20 and 200 standard centimeters cubed per minute (sccm). Comparing vacuum to inert purge at 200 sccm, the CMS membranes formed under vacuum displayed higher selectivity with lower productivity. Geiszler suggested that the inert purge enhanced mass and heat transfer during the pyrolysis process, increasing the removal of volatile by-products during the degradation of the polymer. It should also be noted that little difference was seen between membranes formed under argon or helium atmosphere. CMS membranes formed under inert purge rates of 20 sccm yielded productivity values lower than that of a vacuum pyrolyzed sample with comparable selectivity, suggesting that pore blockage was occurring due to the low by-product removal rate. These trends were more pronounced at the lower pyrolysis temperature of 550 ºC compared to 800 ºC.

Further investigation of vacuum versus inert pyrolysis atmosphere effects on CMS membranes were performed by Williams (*36*). These studies identified that the presence of dilute oxygen within the pyrolysis atmosphere alters the resulting separation

properties of the CMS membranes. This development, referred to as oxygen doping, centers on the fact that oxygen present within the pyrolysis atmosphere at high temperatures will selectivity chemisorb to the ultramicropore sites, which have been shown to be ~17x more reactive than carbon basal planes (*47*). A schematic representation of oxygen doping is provided in Figure 2.9 below.

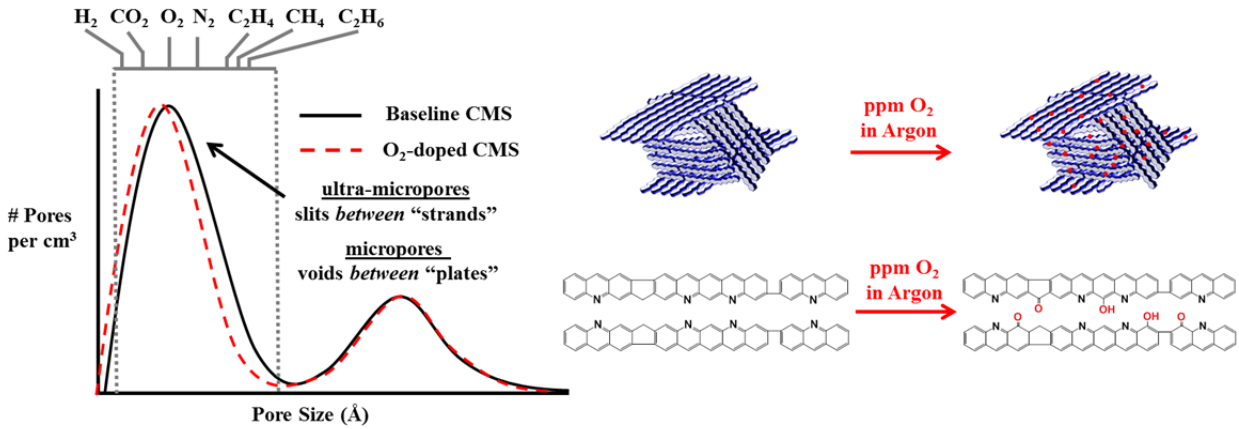

Figure 2.9. Schematic representation of oxygen doping of CMS membranes. Note selective oxygen chemisorption on the edge of the ultramicropore (strand) edges, leading to a shift in the ultramicropore size distribution.

Detailed studies of pyrolysis oxygen concentration and the impacts upon resulting CMS membranes were conducted by Kiyono *et. al.* (*48*, *49*). The results of this work showed that the oxygen doping, when carefully applied, can be used to fine-tune the resulting separation performance of CMS membranes derived from 6FDA:BPDA-DAM(1:1) and Matrimid® for CO_2/CH_4 separations. It was confirmed, via gas sorption measurements on Matrimid® derived CMS membranes, that oxygen doping selectively modifies the ultramicropores responsible for the molecular sieving nature of CMS materials, and not the micropores believed to be responsible for sorption within CMS membrane (*50*). A similar study for different 6FDA-based polyimide precursors showed

the same effect applies, suggesting this is general to all CMS materials (*43*). These results suggest a tightening of the ultramicropore size distribution without impacting the micropore distribution, allowing for the synthesis of highly selective, yet highly productive CMS membranes (cf. Figure 2.9). However, "over-doping" can occur at higher concentrations of oxygen in the pyrolysis atmosphere resulting in CMS membranes with undesirable performance (*49*). The resulting low productivity and selectivity due is due to an overly tight CMS microstructure that begins to exclude both penetrants equally due to the loss of size specificity. This suggests that optimum levels of oxygen doping will depend upon the polymer precursor, pyrolysis temperature, and gas separation of interest.

The discussions above show that pyrolysis atmosphere can have a significant impact upon the resulting structure, hence the performance of CMS membranes. However, comparing vacuum to inert gas purge atmospheres, more desirable performance is attained for CMS membranes formed under inert gas purge. Taking these facts into account, in the context of this work, all CMS membranes will be formed under an inert gas pyrolysis. Additionally, low level oxygen doping will be applied to CMS membranes for the C_2H_4/C_2H_6 separation, with the hopes of creating improved selectivity membranes for this challenging gas pair.

2.4.4 Carbon Molecular Sieve Membrane Post-treatment

Various methods for post-treatment of CMS membranes have been developed in order to perform a fine tuning of the resulting microporous structure. Common post-treatment methods include: post-oxidation, chemical vapor deposition, and coating applications.

Post-oxidation of CMS membrane involves an extended exposure to an oxidizing atmosphere, after CMS synthesis, and is commonly performed at a temperature lower than the CMS formation temperature. Kusakabe *et. al.* post-oxidized CMS membranes derived from BPDA-ODA in oxygen at 300 °C for 3 hours (*38*). The resulting membranes showed a significant increase in productivity but unchanged selectivity, attributed to an increase in micropore volume with minimal rearrangement of the CMS structure. Similar productivity enhancements were seen by Sofer *et. al.* after exposing their cellulose derived CMS hollow fibers to 400 °C air for 15 minutes (*4*).

Chemical vapor deposition (CVD) has also been utilized to selectively narrow the resulting pore size distributions within CMS membranes, increasing selectivity in the CVD treated membranes. Hayashi *et. al.* were able to increase permselectivity of CMS membranes formed from BPDA-ODA at 700 °C by CVD deposition of thin layers of carbon at 650 °C, using propylene as a carbon source (*51*). This selectivity enhancement was attributed to a narrowing of the microporous pore distribution within the CMS materials, due to the thin layers of pyrolytic carbon deposited during the CVD process.

Coatings as post-treatment methods for CMS membranes have been identified as attractive candidates for simple methods of increasing separation performance and robustness. In order to combat productivity losses when exposed to humidified gas feeds, Jones and Koros developed a Teflon® based hydrophobic coating treatment that allowed for retention of a majority of initial separation performance, even when subjected to feed streams up to 85% relative humidity (*52*, *53*). Petersen *et. al.* coated Kapton® derived CMS hollow fiber membraned with polydimethylsiloxane (PDMS) to seal small defects

present within their membranes, identical to a common procedure utilized in the manufacturing process of polymeric gas separation membranes (*54*).

The above discussions show that there are many different ways that CMS membranes can be post-treated in order to enhance or stabilize the resulting material performance. However, it seems that there has yet to be attempts at post-treatments involving chemical modifications of CMS membranes. This presents an avenue of investigation that motivated the research conducted in Chapters 4 and 5 of this work, where small molecule chemical dopants are utilized in a novel post-synthetic treatment for CMS membranes.

2.5 Physical Aging of Carbon Molecular Sieve Membranes

Post-formation, CMS materials are subject to a physical aging phenomenon envisioned to be similar to that experienced by their glassy polymeric precursors (*16*, *31*, *39*). Within glassy polymers, small-scale relaxation of chains leads to a reduction in free volume elements responsible for transport of a penetrant, causing a reduction in productivity of the material with time (*55*, *56*). While CMS materials are thought to be made from imperfect packing of aromatic plates and not chain-like structures (cf. Figure 2.1), it is envisioned that partial densification of these imperfectly stacked aromatic plates may occur, leading to reduction in the average micropore size (distance between plates, or the molecular jump length λ in Figure 2.10). This partial densification leads to reduced productivity, mainly by the reduction of sorption capacity, coupled with a minor increase in selectivity due to minor changes in the critical ultramicropore distribution (d_{um} in Figure 2.10). Additionally, physical aging cannot be reversed by high temperature

treatment, whereas heating a glassy polymer above the glass transition temperature can "reset" the material, restoring its original properties (*57*).

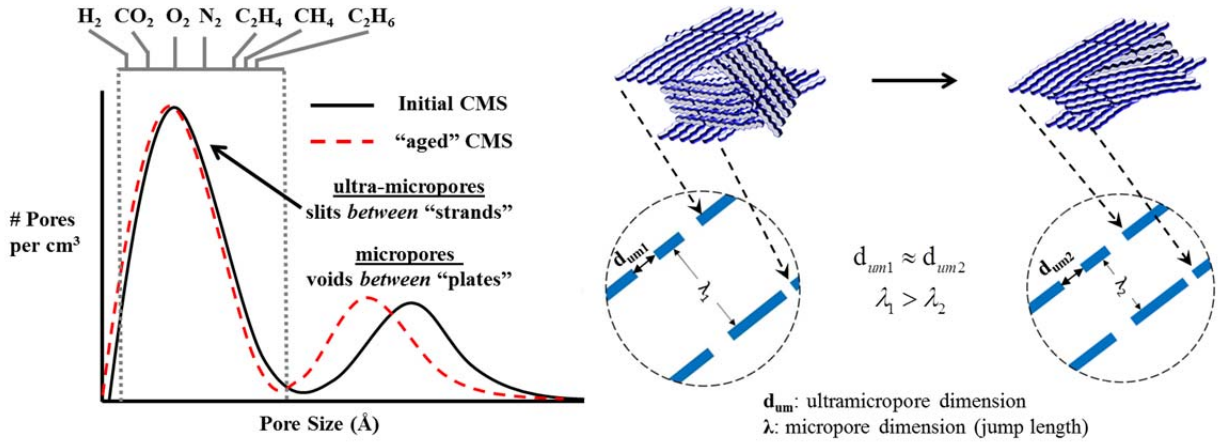

Figure 2.10. Schematic depicting physical aging within CMS materials results in micropore settling coupled with minor ultramicropore slit tightening.

Xu *et. al.* showed that when comparing "fresh" performance of 6FDA:BPDA-DAM(1:1) derived CMS membranes formed at 550 °C to membranes that had been stored in ambient conditions for 228 days, permeation rates of He exhibited a ~19% drop while C_2H_4 showed a ~75 % drop in productivity. These trends suggest that the larger end of the ultramicropore distribution, which has greater implications upon separation of larger gases like C_2H_4 (kinetic diameter of 3.75 Å vs 2.6 Å for He), were altered due to the minor rearrangement *within the aromatic sheets*. In the same study, C_2H_4 gas sorption within 6FDA-DAM derived CMS membranes formed at 675 °C was tracked as a function of aging time. These materials displayed an ~ 47% reduction in the Langmuir hole filling capacity ($C_{HA}^{'}$ in Equation 2.10), a measure of the sorption sites available within a CMS material, over 65 days of aging time. Similar trends have emerged in various other 6FDA-based CMS materials with applications for O_2/N_2 and CO_2/CH_4

separations (*31*), as well as supported CMS membranes for C_3H_6/C_3H_8 separations (*58*), suggesting this is a phenomenon experienced by all CMS materials.

While physical aging is an aspect of CMS membranes that needs to be further investigated, exposure to continuous active feed or storage under moderate pressure CO_2 allows for arresting the relaxation of the aromatic sheets (*37*, *39*). It is believed that presence of either actively permeating species, or the highly condensable CO_2, saturates the volume between the aromatic sheets (i.e. micropores) preventing rearrangement; however, further investigation of these hypotheses is required, and will be considered within this work. Additionally, other solutions aside from active feed or pressurized storage of CMS membranes are desired in terms of deploying CMS materials into production-scale gas separations, as time-dependent material performance is undesirable from a process engineering standpoint, will also be addressed in this work.

2.6 Formation of Asymmetric Hollow Fibers: Dry-Jet/Wet-Quench Spinning

A majority of fundamental membrane research, especially on the laboratory scale, is performed in the flat sheet, or dense film, morphology, owing to ease of both testing and manufacture. However, these methods limit testable (active) membrane areas to ~ 1 in^2, and practical gas separations require active areas orders of magnitude larger than that. This is especially true for bulk gas separations to be performed in upstream oil and gas or downstream petrochemical applications. Designing membranes is not only a function of material permeability and selectivity, but also the ability to form high surface area/low volume modules in which to package the membranes (*59*). Hollow fiber membranes, depending upon the diameter, can offer up to one order of magnitude

increase in available packing density when compared to the less desirable spiral wound and plate-and-frame configurations.

Within the hollow fiber membrane morphology, asymmetric structures are particularly desired as they have a decreased transport resistance due to the small, thin dense layer that performs the separation (l in Equations 2.1 and 2.2). Figure 2.11 below shows the structure of an asymmetric hollow fiber, wherein the thin, dense separation skin layer is supported upon a porous substructure. The dense skin layer is typically <1% of the total fiber thickness, and is responsible for the separation performance of the membrane. The porous substructure provides mechanical strength for the membrane and preferentially provides little to no transport resistance, owing to its high porosity. Hollow fiber membranes can be formed by either single-layer or dual-layer fiber spinning processes. Single-layer hollow fibers are formed by the co-extrusion of a polymer solution (dope) with a bore fluid, using co-annular die (spinneret) with two channels: one for the dope and one for the bore fluid (cf. Figure 2.12). In this method the dense skin layer and porous substructure are made from the same material. In the case of a dual-layer fiber, two polymer dopes (sheath and core) are coextruded with a bore fluid through a more complex co-annular die with three channels: sheath, core, and bore. While significantly more complex, dual-layer fiber spinning allows for the option of the sheath and core layers to be made from different materials. For example, a high performance, expensive polymer can be utilized as the sheath layer with a lower performing, less expensive polymer as the core layer providing mechanical support and minimal transport resistance. This morphology can allow for significant savings in membrane module construction costs, but is a non-trivial process and an area of significant research.

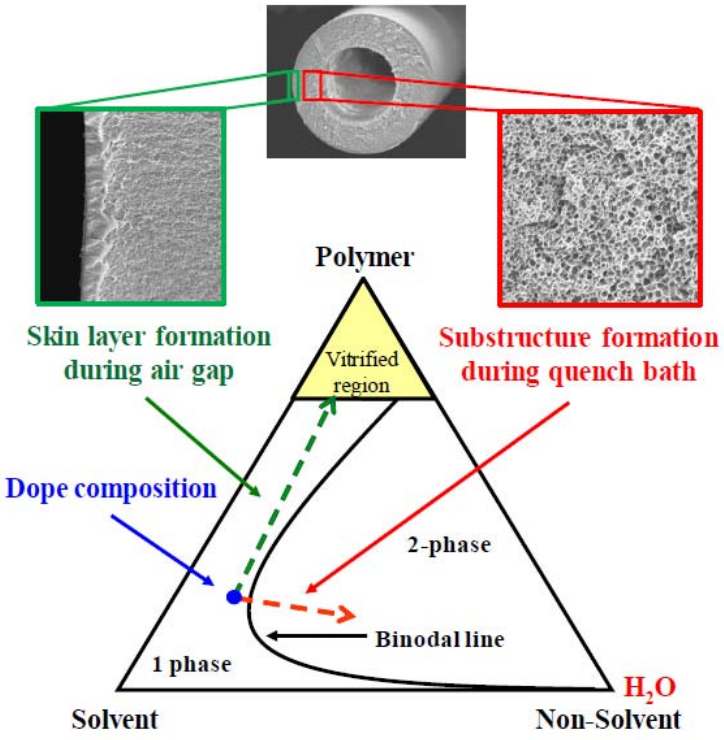

Figure 2.11. Ternary phase diagram and images of asymmetric hollow fiber morphology. Adapted from (*39*).

Asymmetric hollow fibers can be produced via the dry-jet/wet-quench fiber spinning process, schematically represented in Figure 2.12 below. In this process the spin dope (polymer solution) and bore fluid are coextruded through the spinneret fluid into the air gap (dry-jet) and then phase separated in the aqueous bath (wet-quench) before being collected on a take-up drum.

Table 2.1. Important spinning parameters for dry-jet/wet-quench fiber spinning.

Solution Parameters	**Spinning Process Parameters**
Dope composition	Environmental conditions
Bore fluid composition	Spinning temperature
Quench bath composition	Air gap
	Dope/bore extrusion rate
	Quench bath temperature
	Take-up rate

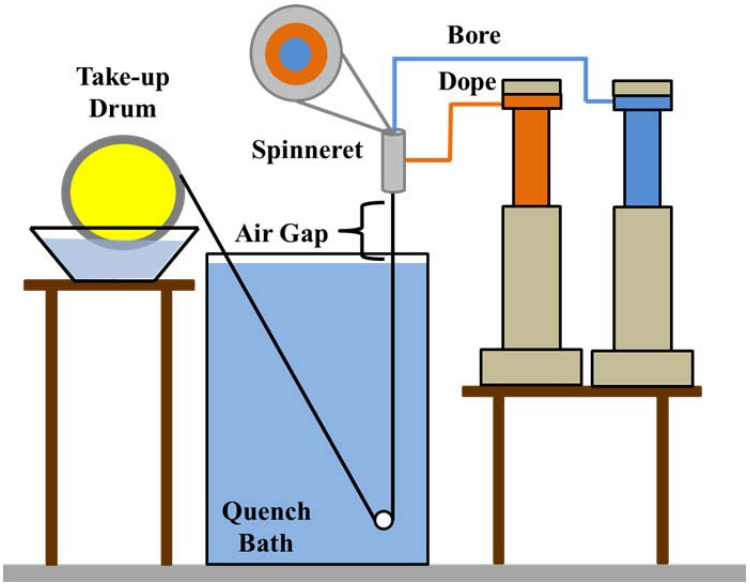

Figure 2.12. Schematic of dry-jet/wet-quench fiber spinning process to form single-layer hollow fiber membranes.

Hollow fiber spinning is a complex process in which many variables control the morphologies and transport properties of the resulting membranes. Detailed studies of asymmetric hollow fiber spinning have been previously reported (*39*, *60–62*), and Table 2.1 summarizes the important parameters identified from these studies. The polymer solution (dope) is generally a mixture of polymer, solvent, and non-solvent. The dope composition and qualitative composition trajectories for skin and substructure formation are noted in Figure 2.11 on the isothermal ternary phase diagram. The ternary phase diagram is typically constructed via the cloud point technique where the binodal line may be determined by increasing non-solvent composition in experimental dope solutions, upon which the dope will transition from the one-phase regime to two-phase regime. The solutions made at varying polymer concentrations that lie on the phase boundary are called “cloud points” which together form the binodal line. Once the binodal line is determined, the spin dope composition is chosen to lie within the one-phase regime, but

sufficiently close to the binodal line to enable efficient phase separation when quenched in the aqueous bath.

When the dope is extruded into the air gap, solvent and non-solvent evaporation will drive the composition of the outermost region of the nascent fiber towards vitrified polymer (green pathway in Figure 2.11) forming the dense, thin separation skin layer. As the fiber travels into the aqueous quench bath, water (non-solvent) will diffuse into the polymer fiber causing phase separation in the substrate under the skin layer (red pathway in Figure 2.11), forming the porous support without disruption of the previously vitrified skin layer. The bore of the hollow fiber is created by the presence of the bore fluid, for which the composition is chosen such that it acts as a "neutral" fluid as to not promote phase separation on the bore side of the nascent fiber. Once the phase separated fiber has travelled through the quench bath, it is collected on a take-up drum. The take-up drum is typically operated at a linear velocity greater than that of the dope/bore extrusion rate from the spinneret (known as the draw ratio) in able to form hollow fibers with significantly smaller dimensions than that of the spinneret dimensions.

The above method was followed for the formation of asymmetric polymeric hollow fibers utilized within this work, with the specific spin details outlined in Chapter 3. Upon successful formation of polymer hollow fibers, they were used as precursor materials in the formation of asymmetric hollow fiber CMS membranes, for which important parameters have already been discussed.

2.7 References

(1) Jenkins, G. M.; Kawamura, K. *Polymeric Carbons -- Carbon Fibre, Glass and Char*; Cambridge University Press, 1976.

(2) Pierson, H. O. *Handbook of carbon, graphite, diamond and fullerenes: Properties, Processing, and Applications*; Noyes Publications: Park Ridge, NJ., 1993.

(3) Koresh, J. E. On the flexibility of the carbon skeleton. *J. Chem. Soc. Faraday Trans.* **1993**, *89*, 935.

(4) Koresh, J. E.; Sofer, A. The Carbon Molecular-sieve Membranes: General Properties and Permeability of CH4/H2 Mixtures. *Sep. Sci. Technol.* **1987**, *22*, 973–982.

(5) Rouqurol, J.; Avnir, D.; Fairbridge, C.; Everett, D.; Haynes, J.; Pernicone, N.; Ramsay, J.; Sing, K.; Unger, K. Recommendations for the characterization of porous solids. *Pure Appl. Chem.* **1994**, *66*, 1739–1758.

(6) Mariwalat, R. K.; Foley, H. C. Evolution of Ultramicroporous Adsorptive Structure in Poly (furfuryl alcohol) - Derived Carbogenic Molecular Sieves. *Ind. Eng. Chem. Res.* **1994**, *33*, 607–615.

(7) Steel, K. M.; Koros, W. J. An investigation of the effects of pyrolysis parameters on gas separation properties of carbon materials. *Carbon N. Y.* **2005**, *43*, 1843–1856.

(8) Koros, W. J. Membranes: Learning a lesson from nature. *Chem. Eng. Prog.* **1995**, *91*, 68–81.

(9) Koros, W. J.; Fleming, G. K. Membrane-based gas separation. *J. Memb. Sci.* **1993**, *83*, 1–80.

(10) Wijmans, J. G.; Baker, R. W. The Solution-Diffusion Model: a Review. *J. Memb. Sci.* **1995**, *107*, 1–21.

(11) Breck, D. W. *Zeolite Molecular Sieves: Structure, Chemistry, and Use*; Wiley & Sons: New York, NY, 1974.

(12) Ruthven, D. M.; Karger, J. *Diffusion in Zeolites and Other Microporous Solids*; Wiley & Sons: New York, NY, 1992.

(13) Steel, K. M. Carbon Membranes for Challenging Gas Separations, The University of Texas at Austin, 2000. Ph.D. Thesis.

(14) Petropoulos, J. H. Some fundamental approaches to membrane gas permeability and permselectivity. *J. Memb. Sci.* **1990**, *53*, 229–258.

(15) Singh, A.; Koros, W. J. Significance of entropic selectivity for advanced gas separation membranes. *Ind. Eng. Chem. Res.* **1996**, *35*, 1231–1234.

(16) Rungta, M. Carbon Molecular Dense Film Membranes for Ethylene/Ethane Separations, Georgia Institute of Technology, 2012. Ph.D. Thesis.

(17) Ruthven, D. M.; Reyes, S. C. Adsorptive separation of light olefins from paraffins. *Microporous Mesoporous Mater.* **2007**, *104*, 59–66.

(18) Koros, W. J.; Zhang, C. Materials for next-generation molecularly selective synthetic membranes. *Nat. Mater.* **2017**, *16*, 289–297.

(19) Ning, X.; Koros, W. J. Carbon molecular sieve membranes derived from Matrimid® polyimide for nitrogen/methane separation. *Carbon.* **2014**, *66*, 511–522.

(20) Glasstone, S.; Laidler, K.; Eyring, H. *Theory of Rate Processes*; 1st ed.; McGraw-Hill: New York, NY, 1941.

(21) Xu, L.; Rungta, M.; Brayden, M. K.; Martinez, M. V.; Stears, B. A.; Barbay, G. A.; Koros, W. J. Olefins-selective asymmetric carbon molecular sieve hollow fiber membranes for hybrid membrane-distillation processes for olefin/paraffin separations. *J. Memb. Sci.* **2012**, *423–424*, 314–323.

(22) Rungta, M.; Zhang, C.; Xu, L.; Koros, W. J. Membrane-Based Ethylene/Ethane Separation: The Upper Bound and Beyond. *AIChE J.* **2013**, *59*, 3475–3489.

(23) Salinas, O.; Ma, X.; Litwiller, E.; Pinnau, I. High-performance carbon molecular sieve membranes for ethylene/ethane separation derived from an intrinsically microporous polyimide. *J. Memb. Sci.* **2016**, *500*, 115–123.

(24) Koresh, J. E.; Sofer, A. Molecular-sieve Carbon Permselective Membrane: 1. Presentation of New Device for Gas-Mixture Separation. *Sep. Sci. Technol.* **1983**, *18*, 723–734.

(25) Campo, M. C.; Magalhães, F. D.; Mendes, A. Carbon molecular sieve membranes from cellophane paper. *J. Memb. Sci.* **2010**, *350*, 180–188.

(26) Centeno, T. A.; Fuertes, A. B. Carbon molecular sieve gas separation membranes based on poly(vinylidene chloride-co-vinyl chloride). *Carbon.* **2000**, *38*, 1067–1073.

(27) Koh, D.-Y.; McCool, B. A.; Deckman, H. W.; Lively, R. P. Reverse osmosis molecular differentiation of organic liquids using carbon molecular sieve membranes. *Science.* **2016**, *353*, 804–807.

(28) Centeno, T.; Vilas, J.; Fuertes, A. Effects of phenolic resin pyrolysis conditions on carbon membrane performance for gas separation. *J. Memb. Sci.* **2004**, *228*, 45–54.

(29) Suda, H.; Haraya, K. Gas Permeation through Micropores of Carbon Molecular Sieve Membranes Derived from Kapton Polyimide. *J. Phys. Chem. B* **1997**, *101*, 3988–3994.

(30) Ma, X.; Lin, B. K.; Wei, X.; Kniep, J.; Lin, Y. S. Gamma-Alumina Supported Carbon Molecular Sieve Membrane for Propylene / Propane Separation. *Ind. Eng. Chem. Res.* **2013**, *52*, 4297–4305.

(31) Fu, S.; Sanders, E. S.; Kulkarni, S. S.; Koros, W. J. Carbon molecular sieve membrane structure–property relationships for four novel 6FDA based polyimide precursors. *J. Memb. Sci.* **2015**, *487*, 60–73.

(32) Ma, X.; Swaidan, R.; Teng, B.; Tan, H.; Salinas, O.; Litwiller, E.; Han, Y.; Pinnau, I. Carbon molecular sieve gas separation membranes based on an intrinsically microporous polyimide precursor. *Carbon.* **2013**, *62*, 88–96.

(33) Salinas, O.; Ma, X.; Litwiller, E.; Pinnau, I. Ethylene/ethane permeation, diffusion and gas sorption properties of carbon molecular sieve membranes derived from the prototype ladder polymer of intrinsic microporosity (PIM-1). *J. Memb. Sci.* **2016**, *504*, 133–140.

(34) Saufi, S.; Ismail, A. Fabrication of Carbon Membranes for Gas Separation—a review. *Carbon.* **2004**, *42*, 241–259.

(35) Fu, Y.-J.; Liao, K.-S.; Hu, C.-C.; Lee, K.-R.; Lai, J.-Y. Development and characterization of micropores in carbon molecular sieve membrane for gas separation. *Microporous Mesoporous Mater.* **2011**, *143*, 78–86.

(36) Williams, P. J. Analysis of Factors Influencing The Performance of CMS Membranes for Gas Separations, Georgia Institute of Technology, 2006. Ph.D. Thesis.

(37) Bhuwania, N. Engineering The Morphology of Carbon Molecular Sieve (CMS) Hollow Fiber Membranes, Georgia Instititue of Technology, 2014. Ph.D. Thesis.

(38) Kusakabe, K.; Yamamoto, M.; Morooka, S. Gas permeation and micropore structure of carbon molecular sieving membranes modified by oxidation. *J. Memb. Sci.* **1998**, *149*, 59–67.

(39) Xu, L. Carbon Molecular Sieve Hollow Fiber Membranes for Olefin/Paraffin Separations, Georiga Institute of Technology, 2012. Ph.D. Thesis.

(40) Okamoto, K.; Kawamura, S.; Yoshino, M.; Kita, H.; Hirayama, Y.; Tanihara, N.; Kusuki, Y. Olefin/Paraffin Separation through Carbonized Membranes Derived from an Asymmetric Polyimide Hollow Fiber Membrane. *Ind. Eng. Chem. Res.* **1999**, *38*, 4424–4432.

(41) Bhuwania, N.; Labreche, Y.; Achoundong, C. S. K.; Baltazar, J.; Burgess, S. K.; Karwa, S.; Xu, L.; Henderson, C. L.; Jason Williams, P.; Koros, W. J. Engineering substructure morphology of asymmetric carbon molecular sieve hollow fiber membranes. *Carbon.* **2014**, *76*, 417–434.

(42) Qiu, W.; Chen, C.; Xu, L.; Cui, L.; Paul, D. R.; Koros, W. J. Sub-Tg Cross-Linking of a Polyimide Membrane for Enhanced CO2 Plasticization Resistance for Natural Gas Separation. *Macromolecules* **2011**, *44*, 6046–6056.

(43) Fu, S.; Wenz, G. B.; Sanders, E. S.; Kulkarni, S. S.; Qiu, W.; Ma, C.; Koros, W. J. Effects of pyrolysis conditions on gas separation properties of 6FDA/DETDA:DABA(3:2) derived carbon molecular sieve membranes. *J. Memb. Sci.* **2016**, *520*, 699–711.

(44) Tin, P. S.; Chung, T.-S.; Kawi, S.; Guiver, M. D. Novel approaches to fabricate carbon molecular sieve membranes based on chemical modified and solvent treated polyimides. *Microporous Mesoporous Mater.* **2004**, *73*, 151–160.

(45) Steel, K. M.; Koros, W. J. Investigation of Porosity of Carbon Materials and Related Effects On Gas Separation Properties. *Carbon.* **2003**, *41*, 253–266.

(46) Geiszler, V. C.; Koros, W. J. Effects of Polyimide Pyrolysis Conditions on Carbon Molecular Sieve Membrane Properties. *Ind. Eng. Chem. Res.* **1996**, *35*, 2999–3003.

(47) Grisdale, R. O. The Properties of Carbon Contacts. *J. Appl. Phys.* **1953**, *24*, 1288.

(48) Kiyono, M.; Williams, P. J.; Koros, W. J. Generalization of effect of oxygen exposure on formation and performance of carbon molecular sieve membranes. *Carbon.* **2010**, *48*, 4442–4449.

(49) Kiyono, M.; Williams, P. J.; Koros, W. J. Effect of Pyrolysis Atmosphere on Separation Performance of Carbon Molecular Sieve Membranes. *J. Memb. Sci.* **2010**, *359*, 2–10.

(50) Kiyono, M. Carbon Molecular Sieve Membranes For Natural Gas Separations, Georgia Institute of Technology, 2010. Ph.D. Thesis.

(51) Hayashi, J.; Mizuta, H.; Yamamoto, M.; Kusakabe, K.; Morooka, S. Pore size control of carbonized BPDA-pp′ ODA polyimide membrane by chemical vapor deposition of carbon. *J. Memb. Sci.* **1997**, *124*, 243–251.

(52) Jones, C. W.; Koros, W. J. Characterization of ultramicroporous carbon membranes with humidified feeds. *Ind. Eng. Chem. Res.* **1995**, *34*, 158–163.

(53) Jones, C. W.; Koros, W. J. Carbon Composite Membranes: A Solution to Adverse Humidity Effects. *Ind. Eng. Chem. Res.* **1995**, *34*, 164–167.

(54) Petersen, J.; Matsuda, M.; Haraya, K. Capillary carbon molecular sieve membranes derived from Kapton for high temperature gas separation. *J. Memb. Sci.* **1997**, *131*, 85–94.

(55) Huang, Y.; Paul, D. R. Effect of Temperature on Physical Aging of Thin Glassy Polymer Films. *Macromolecules* **2005**, *38*, 10148–10154.

(56) Huang, Y.; Paul, D. R. Physical aging of thin glassy polymer films monitored by gas permeability. *Polymer.* **2004**, *45*, 8377–8393.

(57) Huang, Y.; Paul, D. R. Experimental methods for tracking physical aging of thin glassy polymer films by gas permeation. *J. Memb. Sci.* **2004**, *244*, 167–178.

(58) Ma, X.; Williams, S.; Wei, X.; Kniep, J.; Lin, Y. S. Propylene/Propane Mixture Separation Characteristics and Stability of Carbon Molecular Sieve Membranes. *Ind. Eng. Chem. Res.* **2015**, *54*, 9824–9831.

(59) Baker, R. W. Future Directions of Membrane Gas Separation Technology. *Ind. Eng. Chem. Res.* **2002**, *41*, 1393–1411.

(60) Clausi, D. T.; Koros, W. J. Formation of defect-free polyimide hollow fiber membranes for gas separations. *J. Memb. Sci.* **2000**, *167*, 79–89.

(61) Zhang, C. Zeolitic Imidazolate Framework (ZIF) -Based Membranes and Sorbents for Advanced Olefin / Paraffin Separations, Georiga Institute of Technology, 2014. Ph.D. Thesis.

(62) Chen, C. Thermally Crosslinked Polyimid Hollow Fiber Membranes for Natural Gas Purification, Georgia Institute of Technology, 2011. Ph.D. Thesis.

CHAPTER 3. MATERIALS AND EXPERIMENTAL METHODS

3.1 Overview

This chapter is an overview of the different materials and experimental procedures used throughout this work. The first section outlines the different polymers and chemicals used to synthesize membrane materials, after which detailed dense film and asymmetric hollow fiber polymer and CMS membrane formation techniques are discussed. The following section describes gas penetrants used within this work, as well as experimental gas transport analysis techniques. Lastly, additional characterization techniques applied to the membrane materials used in this work will be discussed.

3.2 Materials

3.2.1 Polymeric Precursors

As was previously mentioned in Chapter 2, polyimides have been identified as attractive gas membrane materials, and the preferred precursor material for CMS formation (1–3). Two different polyimides were used in this work: BTDA-DAPI a commercially available polyimide often referred to by its tradename Matrimid® (Huntsman International, LLC), and 6FDA:BPDA-DAM(1:1) an in-house synthesized copolyimide. The 6FDA:BPDA-DAM copolyimide was synthesized via a condensation reaction between 4,4'-(Hexafluoroisopropylidene) diphthalic (6FDA) and 3,3'-4,4'-biphenyl tetracarboxylic acid (BPDA) dianhydrides with 2,4,6-trimethyl-1,3-diaminobenzene (DAM) diamine. The two step synthesis involves first forming a high molecular weight polyamic acid at low temperatures (~5 ^{0}C) and performing a second

chemical imidization step, the specifics of which are described elsewhere (4). The chemical structures and names of the polymers used are shown below in Figure 3.1.

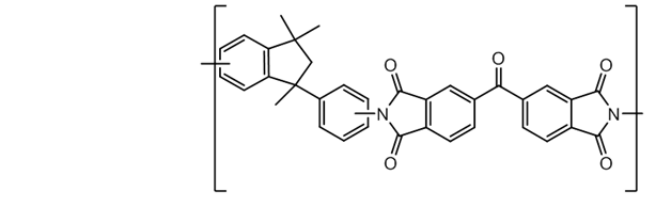

Matrimid® (BTDA-DAPI)
BTDA: 3,3'-4,4'-benzophenone tetracarboxylic dianhydride
DAPI: 5(6)-amino-1-(4'-aminophenyl)-1,3-trimethylindane

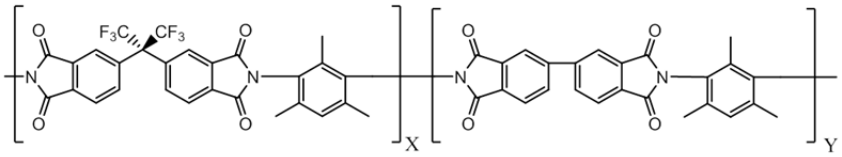

6FDA:BPDA-DAM (X=1, Y=1)
6FDA: 4,4'-(hexafluoroisopropylidene) diphthalic anhydride
BPDA: 3,3'-4,4'-biphenyl tetracarboxylic dianhydride
DAM: 2,4,6-trimethyl-1,3-phenylene diamine

Figure 3.1. Chemical structure of semi-flexible precursor polyimides Matrimid® and 6FDA:BPDA-DAM(1:1).

3.3 Membrane Formation

3.3.1 Polymeric Membranes

3.3.1.1 Dense Films

In order to synthesize a dense film (flat sheet) membrane, first the polymer powder of interest was dried in a vacuum oven at 120 ^{0}C overnight to remove any excess moisture. The dried powder was dissolved in dichloromethane (DCM, >99.8% purity, Sigma-Aldrich) to form a 2-5 wt% polymer solution and placed on a roller for at least 6 hrs to ensure a homogeneous solution. The polymer solution was used to prepare

polymeric dense films via solution casing method at room temperature as shown in Figure 3.2.

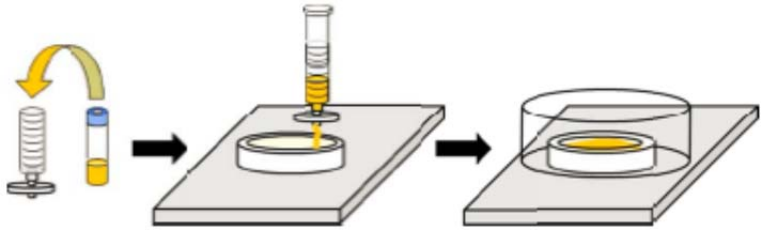

Figure 3.2. Schematic of solution casting process for polymer dense films (*5*).

A leveled stage was placed inside a plastic glove bag to ensure a flat and uniform surface for the Teflon® dish used as the casting substrate. The previously prepared polymer solution, 30 mL syringe with 0.45 μm filter, an empty 40 mL glass vial, and two jars containing excess DCM were placed into the glove bag. The glove bag was sealed and purged with N_2 and allowed to saturate with DCM for at least 4 hours. The prepared polymer dope was filtered through the syringe into the empty vial and allowed to rest while the glove bag atmosphere was saturating with DCM, in order to allow removal of gas bubbles introduced during the filtering process. After DCM atmosphere saturation, the filter polymer solution was slowly poured into the Teflon® dish and covered with a crystallization dish to facilitate a slow DCM evaporation rate over 3-4 days. The vitrified polymer film was removed from the casting dish and dried at 120 ^{0}C overnight to remove any residual solvent prior to use.

3.3.1.2 Asymmetric Hollow Fibers

Asymmetric hollow fibers of were formed with a dry-jet/wet-quench fiber spinning process, as was previously described in Chapter 2 Section 6. A composite spinneret (Extended) was used for the spinning of single layer fibers for this work. Specific details of spinning of 6FDA:BPDA-DAM(1:1) asymmetric hollow fibers may be found elsewhere (*6*). Minor changes were made to dope composition and spinning parameters were made for this specific polymer batch, which are shown in Table 3.1 below. All dry additives were vacuum dried at 120 °C overnight before use, and all solvents were of anhydrous purity (Sigma-Aldrich, >95%) and were used without further purification.

Table 3.1 Spinning conditions of 6FDA:BPDA-DAM (1:1) asymmetric hollow fibers.

Spinning Parameters	**6FDA:BPDA-DAM(1:1)**
Dope composition (wt%)	20 wt% polymer, 47.5 wt% NMP, 10 wt% THF, 16 wt% EtOH, 6.5 wt% $LiNO_3$
Bore fluid composition (wt%)	85 wt% NMP, 15 wt% H_2O
Dope/bore fluid flow rate (mL/hr)	180/60
Spinneret temperature (^{0}C)	70
Water quench bath temperature (^{0}C)	50
Air gap (cm)	10-20
Take-up rate (m/min)	20-30

Fibers collected on the take-up drum were allowed to solvent exchange on the drum for at least 10 minutes during the spinning process, after which the fibers were cut

off the drum and placed into fresh DI (deionized) water that was changed four separate times over 72 hours. The fibers were then solvent exchanged in three separate 20 minute methanol baths followed by three separate 20 minute hexanes baths. After the last hexanes bath, the fibers were allowed to air dry for an hour prior to a one hour vacuum drying at 120 °C.

3.3.2 Carbon Molecular Sieve Membrane Formation

3.3.2.1 Pyrolysis Furnace Setup

The pyrolysis system used for this work is identical to that of which was previously reported, shown in Figure 3.3 below (*5*, *6*).

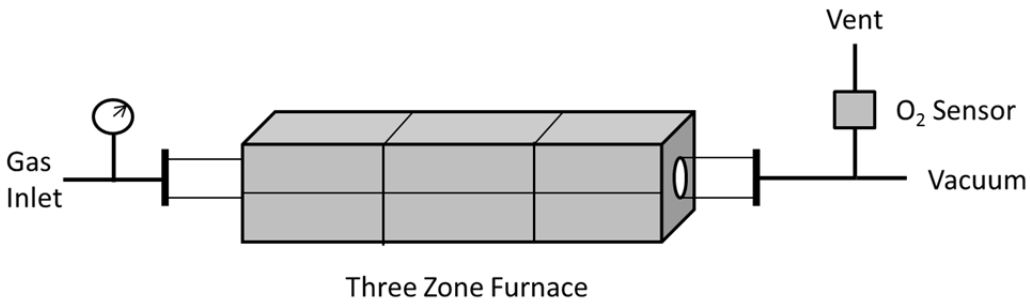

Figure 3.3. Pyrolysis furnace setup for three zone furnace.

The currently used system consists of a three zone furnace (Thermcraft, Inc. Model XST-3-0-24-3C, Winston-Salem, NC) with control of each zone by a multi-channel temperature controller (Omega Engineering, Inc., Model CN1507TC, Stamford, CT), allowing for accurate and uniform control of the desired temperature protocol. A quartz tube (55 mm I.D. x 4 ft length, National Scientific Company, GE Type 214 quartz, Quakertown, PA) was used to contain desired pyrolysis atmosphere, sealed on each side

with an assembly of metal flanges and silicon O-rings (MTI Corporation, Richmond, CA). A mass flow controller (MKS Instruments, MA) was used to maintain accurate control of the desired pyrolysis purge gas during the pyrolysis process. The pyrolysis atmosphere was monitored with an oxygen analyzer (Rapidox 2100, Cambridge Sensotec, Ltd., Cambridge, England) to ensure the desired concentration was achieved prior to execution of the pyrolysis procedure.

Dense polymeric films were pyrolyzed on a custom made channeled quartz plate (United Silica Products, Franklin, NJ), shown in Figure 3.4, allowing for diffusion of volatile pyrolysis by-products.

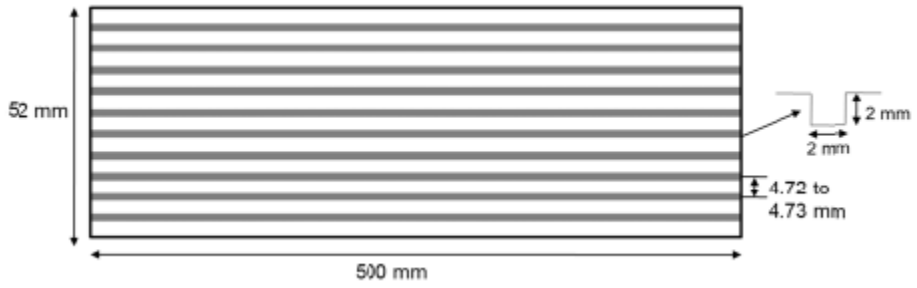

Figure 3.4. Custom quartz plate for dense film pyrolysis (*5*).

Asymmetric hollow fibers were pyrolyzed on a stainless steel mesh support (McMaster Carr, Robbinsville, NJ), as shown in Figure 3.5. Stainless steel wire was utilized to create loose loops, which the hollow fibers were threaded through, in order to prevent fibers from touching during the pyrolysis process.

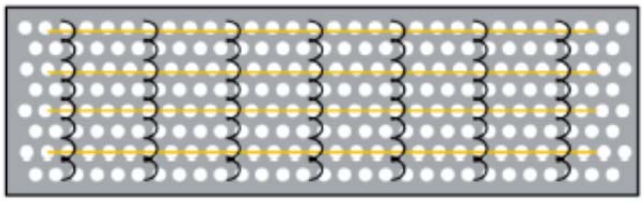

Figure 3.5. Custom made stainless steel mesh support for pyrolysis of asymmetric hollow fibers (*7*).

3.3.2.2 Pyrolysis Protocol

Both dense film and asymmetric hollow fiber polymeric precursors were pyrolyzed under consistent heating protocols, regardless of final temperature or pyrolysis atmosphere. Prior to pyrolysis the desired atmosphere was achieved by purging with the desired gas (e.g. UHP Argon) at 200 sccm for at least 12 hours, while monitoring the atmosphere with the oxygen sensor. In this work the final pyrolysis temperature (T_{pyro}) was varied from 550 – 800 ^{0}C with a soak time of 120 minutes at the final temperature, unless otherwise specified. The heating protocol used in this work is listed below:

1. 50 ^{0}C – 250 ^{0}C at 13.3 ^{0}C/min
2. 250 ^{0}C – (T_{pyro} – 15) ^{0}C at 3.85 ^{0}C/min
3. (T_{pyro} – 15) ^{0}C – T_{pyro} at 0.25 ^{0}C/min
4. 120 min. soak at T_{pyro}

After completing the pyrolysis protocol, the furnace was allowed to cool naturally to room temperature under inert flowing gas. The resulting CMS membranes were removed from the furnace and used in subsequent characterization. After each pyrolysis, the quartz tube and support were rinsed with acetone and heated to 800 ^{0}C with a 120 minute soak under 500 sccm air flow to remove any residue that might affect subsequent pyrolysis runs.

3.3.3 Post-synthetic Amine Doping Treatment of Asymmetric Hollow Fiber CMS Membranes

Tetrahydrofuran (THF, Sigma-Aldrich, >99.9%, inhibitor free) was chosen as the treatment solvent due to the ease of solubility of amine dopants, while the small molecular size facilitates transport of the solvated amine dopants into the CMS structure. Another advantage of THF, described in Chapter 4, is that exposing CMS membranes to pure THF has no effect upon the separation performance. Anhydrous, inhibitor-free THF was utilized to prevent any possible interaction between the common peroxide inhibitor dibutylhydroxytoluene and the CMS materials.

During the course of this work various dopants were used to investigate the role of amine dopant size, reactivity, and functionality and the resulting CMS membrane performance, results of which will be discussed in detail later. Table 3.2 below shows all of the dopants (Sigma-Aldrich, >99%) used in this study.

Table 3.2. Summary of reactive and non-reactive molecular dopants used in this work.

Dopant	Chemical Structure
***p*-phenylenediamine (PPDA)**	
1,4-cyclohexanediamine (PCDA)	
Ethylene diamine (EDA)	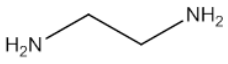
Aniline	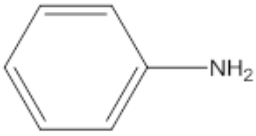
***p*-xylene**	

Once fresh CMS fibers were prepared, they were immediately placed into a graduated cylinder filled with the desired concentration of amine dopant dissolved in THF. The cylinder was capped and the headspace was purged with nitrogen gas to displace any residual air. The fibers were allowed to soak in the solution for 24 hours, removed and prepared for characterization by:

1. Rinsing three times with fresh, inhibitor-free THF.
2. Air dry for 20 minutes.
3. Vacuum dry at 120 ^{0}C for 20 minutes.

Once CMS fibers had been removed from the vacuum oven they were immediately prepared for gas permeation or pressure decay sorption measurements.

3.4 Membrane Characterization

3.4.1 Gases

Pure gases used throughout this study to characterize permeation and sorption measurements included helium (He, UHP Grade, Airgas), nitrogen (N_2, UHP Grade, Airgas), oxygen (O_2, UHP Grade, Airgas), carbon dioxide (CO_2, Research Grade, Airgas), methane (CH_4, Research Grade, Airgas), ethylene (C_2H_4, Chemical Purity, Airgas), and ethane (C_2H_6, Chemical Purity, Airgas).

Binary mixtures of CO_2/CH_4 (50/50 mol%) and C_3H_6/C_3H_8 (50/50 mol%) were acquired from Nexair and used for mixture gas permeation experiments.

Different grades of argon were used for the pyrolysis atmosphere during CMS membrane formation. Pure argon (Ar, UHP Grade, Airgas) and specialty mixtures of 10 ppm, 20 ppm, and 30 ppm O_2 in balance Ar (Nexair) were used in this work.

3.4.2 Permeation

3.4.2.1 Dense Film Masking

Both single-gas and mixed-gas permeation measurements were performed on CMS dense films at 35 ^{0}C, following previously described methods (*8*). A permeation cell, constructed of stainless steel, is used to sandwich a film between the upstream (feed) and downstream (collection) sides of a permeation system, shown in Figure 3.6 below.

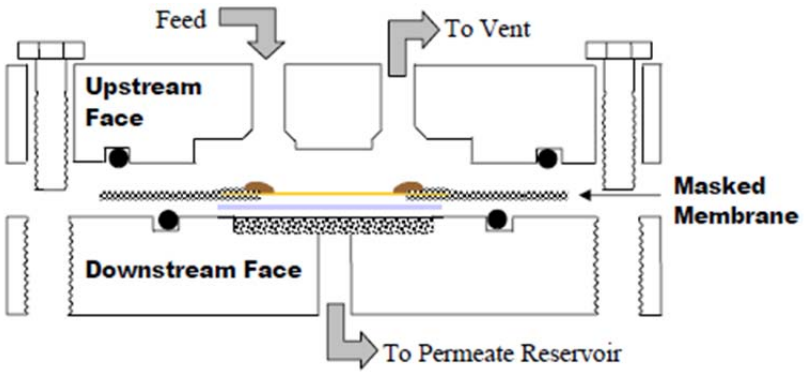

Figure 3.6. Schematic of masking technique used for dense film permeation measurements (*9*).

A schematic of the film masking technique is also provided in Figure 3.6, where the CMS films are sandwiched between two pieces of impermeable aluminum tape (Intertape ALF200L). Special care must be taken throughout this entire process, as the CMS materials are brittle and may crack, yielding an untestable membrane. The sandwiched film, along with 3 pieces of filter paper (Whatman), are placed on top of the sintered metal support and masked onto the permeation cell using another piece of aluminum tape. The CMS/tape interface was sealed with DP-100 epoxy (3M, Minneapolis, MN) to minimize any gas leak between the upstream and downstream sides of the membrane. Upon completion of membrane masking, the assembled cell is loaded into the constant-volume permeation system, described in Section 3.4.2.4. The available area for permeation of each film was determined via computer imaging software (ImageJ) of scanned films, and the membrane thickness was determined via multiple measurements with a digital micrometer.

3.4.2.2 Hollow Fiber Module Construction

Permeation measurements of hollow fiber membranes were performed at 35 ^{0}C using either a constant volume or a constant permeation system, depending upon the

materials being tested. A schematic of a laboratory-scale hollow fiber module is shown in Figure 3.7 below, for which details of construction and membrane potting are described elsewhere (*10*, *11*).

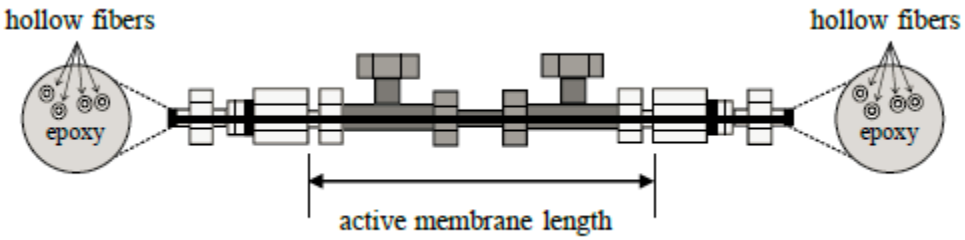

Figure 3.7. Schematic of laboratory-scale hollow fiber membrane module (8).

Pure-gas permeation of polymeric precursor fibers was performed on modules containing 3-6 fibers, with active lengths of 15 – 20 cm and permeation measurements collected via constant pressure system, owing to the ease of fabrication of multi-fiber modules with large active membrane areas. While multi-fiber CMS membranes are possible to make, due to the more delicate nature pure and mixed-gas permeation measurements were performed on single CMS membrane fiber modules with active lengths 10 – 15 cm and tested in at least triplicate to assess experimental uncertainty. Due to the relatively low flux of a single fiber module, CMS modules were tested in a constant volume permeation system with a sensitive vacuum pressure transducer downstream.

3.4.2.3 Constant Pressure Permeation

Pure-gas permeation measurements of asymmetric polymeric precursor fibers were performed using a constant pressure permeation system, details of which are described elsewhere (*10*). Bore-side feed of 100 psig of O_2, N_2, and He was used to

characterize precursor fiber permeation performance. The permeate flow was measured via bubble flow meter at atmospheric pressure from the shell-side of the module depicted in Figure 3.7 above.

3.4.2.4 Isochoric Permeation

Pure and mixed-gas permeation measurements of CMS dense film and hollow fiber membranes were performed utilizing an isochoric (constant volume/variable pressure) permeation system at 35 ^{0}C unless otherwise specified, details of which are described elsewhere (*5*, *6*, *12*).

Specifically for CMS dense films, the upstream and downstream sides of the membrane were degassed for 18 hours prior to introduction of feed gas to the upstream side of the membrane to ensure an apparent outgassing or leak rate <1% of the permeation of the slowest gas of interest. Special care was taken to introduce feed gas slowly to a CMS dense film as to not break the film during testing. Upstream feed pressures of 50 psia were utilized for all gases, unless otherwise specified.

After module construction and fiber potting, per Section 3.4.2.2, hollow fiber CMS membrane modules were loaded into the constant volume permeation system and degassed for ~30 minutes, ensuring the apparent outgassing or leak rate <1% of the slowest permeating species (analogous to CMS dense film testing procedures). Upon completion of a successful leak test, feed gas was slowly introduced to the shell-side of the hollow fiber while the bore-side pressure rise was monitored via pressure transducer (MKS Baratron®).

Mixed gas permeation was performed with the desired mixture with an upstream pressure of 50 psia, unless otherwise specified. For mixed-gas permeation measurements,

retentate flow over the feed side of the membrane was controlled with a needle valve. The stage cut, which is the percentage of the feed that permeates through the membrane, was kept less than 1% to avoid concentration polarization. Permeate compositions were analyzed with a gas chromatograph (Bruker 450) using a TCD detector with He as the carrier gas.

3.4.3 Sorption

3.4.3.1 Pressure Decay Sorption

Gas sorption measurements were made using a dual volume pressure decay method, shown in Figure 3.8 (*13*). Once the samples were loaded, the entire system was degassed for 12 hours. To start a run the reservoir was filled with a known amount of the gas of interest and thermally equilibrated for 20 minutes. The entire system was kept in a heated oil bath with a circulator to maintain a constant temperature. The valve between the reservoir and sample cell was quickly opened and closed to introduce gas to the sample. Pressure in both chambers was monitored with pressure transducers through LabView until equilibrium was achieved, at which time the run was stopped and the amount of sorbed gas was calculated with a mole balance. All isotherms were measured at 35 ^{0}C with sample cell pressures ranging from 15 psia to 250 psia. Compressiblity factor equations were calculated using the NIST SUPERTRAPP software and are listed in Appendix A.

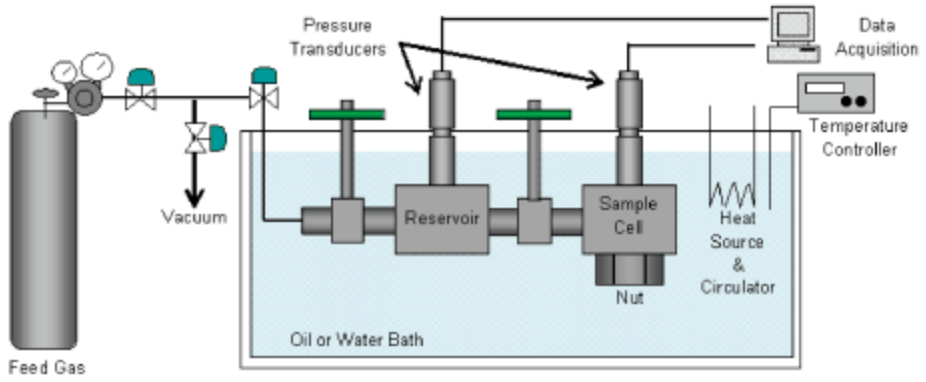

Figure 3.8. Schematic of dual-volume pressure decay sorption apparatus (*14*).

3.4.3.2 CO_2 Physisorption

Pore size distributions and pore volumes of CMS materials were determined using CO_2 uptake measurements at 0 ^{0}C (273 K) on a Micromeritics ASAP 2020 instrument. Pore size distributions were generated using density functional theory analysis (MicroActive Software Version 3.00) of experimentally measured CO_2 uptake curves in order to probe the microporous structure present in CMS materials (*15*, *16*).

3.4.4 Complementary Characterization Techniques

3.4.4.1 Series TGA-FTIR

Stability of the treated CMS membrane materials was investigated with thermogravimetric analysis (TGA, TA Instruments, Q50) combined with a Fourier transform infrared spectrometer (FTIR, Thermo Scientific, iS50) for analysis of the evolved gases. All samples were heated under a 90 cc/min argon (Ultra High Purity, Airgas) purge, following the heating protocol:

1. RT to 110 ^{0}C at a ramp rate of 10 ^{0}C/min
2. Isothermal at 110 ^{0}C for 30 minutes
3. 110 ^{0}C – 550 ^{0}C at a ramp rate of 10 ^{0}C/min
4. Isothermal at 550 ^{0}C for 120 minutes.

3.4.4.2 Nuclear Magnetic Resonance (NMR)

Solid state nuclear magnetic resonance (NMR) was performed by Dr. Johannes Leisen (Georgia Institute of Technology NMR Center) on a Bruker AV3-400 spectrometer used in conjunction with magic-angle spinning (MAS) with cross-polarization (CP) variable contact-time measurements. Due to the low natural abundance of the ^{15}N isotope, CMS membranes were treated with ^{15}N-enriched samples of PPDA and aniline (98 atom % ^{15}N, 99% purity, Sigma Aldrich), identical to the method outlined in Section 3.3.3. Analysis of both ^{13}C and ^{15}N MAS-CP solid-state NMR of amine doped CMS membranes is discussed in Chapter 5.

3.4.4.3 Scanning Electron Microscopy (SEM)

CMS fiber samples were fractured in liquid nitrogen before being mounted onto the sample holder. Samples were imaged using a Zeiss Ultra 60 field image scanning electron microscope.

3.4.4.4 Elemental Analysis

Elemental analysis of CMS membranes were performed by ALS Environmental (Tuscon, AZ). Carbon, nitrogen, and hydrogen contents were determined via combustion analysis, whereas oxygen content was determined via IR pyrolysis analysis.

3.5 References

(1) Jones, C. W.; Koros, W. J. Carbon molecular sieve gas separation membranes-II. Regeneration following organic exposure. *Carbon.* **1994**, *32*, 1427–1432.

(2) Saufi, S.; Ismail, A. Fabrication of Carbon Membranes for Gas Separation—a review. *Carbon.* **2004**, *42*, 241–259.

(3) Sanders, D. F.; Smith, Z. P.; Guo, R.; Robeson, L. M.; McGrath, J. E.; Paul, D. R.; Freeman, B. D. Energy-efficient polymeric gas separation membranes for a sustainable future: A review. *Polymer.* **2013**, *54*, 4729–4761.

(4) Qiu, W.; Chen, C.; Xu, L.; Cui, L.; Paul, D. R.; Koros, W. J. Sub-Tg Cross-Linking of a Polyimide Membrane for Enhanced CO2 Plasticization Resistance for Natural Gas Separation. *Macromolecules* **2011**, *44*, 6046–6056.

(5) Rungta, M. Carbon Molecular Dense Film Membranes for Ethylene/Ethane Separations, Georgia Institute of Technology, 2012. Ph.D. Thesis.

(6) Xu, L. Carbon Molecular Sieve Hollow Fiber Membranes for Olefin/Paraffin Separations, Georiga Institute of Technology, 2012. Ph. D. Thesis.

(7) Ning, X. Carbon Molecular Sieve Membranes for Nitrogen / Methane Separation, Georgia Institute of Technology, 2014. Ph.D. Thesis.

(8) Moore, T. T.; Damle, S.; Williams, P. J.; Koros, W. J. Characterization of low permeability gas separation membranes and barrier materials; design and operation considerations. *J. Memb. Sci.* **2004**, *245*, 227–231.

(9) Williams, P. J. Analysis of Factors Influencing The Performance of CMS Membranes for Gas Separations, Georgia Institute of Technology, 2006. Ph.D. Thesis.

(10) Chen, C. Thermally Crosslinked Polyimid Hollow Fiber Membranes for Natural Gas Purification, Georgia Institute of Technology, 2011. Ph. D. Thesis.

(11) Vu, D. Q.; Koros, W. J.; Miller, S. J. High Pressure CO 2 / CH 4 Separation Using Carbon Molecular Sieve Hollow Fiber Membranes. *Ind. Eng. Chem. Res.* **2002**, *41*, 367–380.

(12) Pye, D. G.; Hoehn, H. H.; Panar, M.; Nemours, E. I. P. De. Measurement of Gas Permeability of Polymers . I . Permeabilities in Constant Volume / Variable Pressure Apparatus. *J. Appl. Polym. Sci.* **1976**, *20*, 1921–1931.

(13) Koros, W. J.; Paul, D. R. Design considerations for measurement of gas sorption in polymers by pressure decay. *J. Polym. Sci. Polym. Phys. Ed.* **1976**, *14*, 1903–1907.

(14) Kiyono, M. Carbon Molecular Sieve Membranes For Natural Gas Separations, Georgia Institute of Technology, 2010. Ph.D. Thesis.

(15) Amico, A. D.; Jiang, Y. Carbon Dioxide Characterization of Carbons with the TriStar II 3020. *23*, 2–3.

(16) Lozano-Castelló, D.; Cazorla-Amorós, D.; Linares-Solano, A. Usefulness of CO2 adsorption at 273 K for the characterization of porous carbons. *Carbon.* **2004**, *42*, 1233–1242.

CHAPTER 4. AMINE DOPING OF CARBON MOLECULAR SIEVE MEMBRANES

Parts of this chapter are reproduced from "Wenz, G.B.; Koros, W.J., Tuning Carbon Molecular Sieve Membranes for Natural Gas Separations: a Diamine Molecular Approach. *AIChE J.,* **2017**, *63*, 751-760.

4.1 Overview

Current CMS material based research has primarily focused on tailoring the membrane materials and formation protocols to achieve higher permeability and selectivity, but there are few studies addressing the long-term stability of CMS membranes (*1–4*). Recent findings by Xu *et. al.*, demonstrated that CMS materials exhibit a time-dependent physical aging, analogous to that of their glassy polymeric precursors (*5*). This phenomenon is hypothesized to be the relaxation of the imperfectly packed turbostratic plate-like structures that give CMS materials their molecular sieving structure. While such aging has been shown to be readily suppressed under active feeds in practical applications, eliminating complexities of such additional procedures would be attractive (*5*, *6*). Presented here is a new methodology, initially intended to suppress CMS physical aging, but which instead provides a new tool for engineering the CMS separation performance.

4.2 Physical Aging of Carbon Molecular Sieve Hollow Fiber Membranes

As noted earlier, there has been very little work regarding the characterization of physical aging within CMS membranes. Xu *et. al.* were of the first to highlight the important phenomena in 6FDA-DAM, 6FDA:BPDA-DAM(1:1), and Matrimid® derived CMS membranes, hypothesizing processes somewhat similar to time-dependent aging like that seen in glassy polymers (*5*). As previously described in Chapter 2 Section 2, CMS materials can be idealized as having "slit-like" pores and represented by a bimodal distribution (*7*, *8*). CMS physical aging is hypothesized to be caused by the relaxation of the graphene-like sheets, resulting in elimination of free volume primarily related to micropores, with a reduction in permeability and some increase in selectivity due to changes in the selective ultramicropore edges. The schematics in Figure 4.1 can be used to illustrate the CMS aging process, where "d_y" and "d_a" refer to the size discriminating ultramicropore dimensions of a "young" and "aged" CMS structures, respectively.

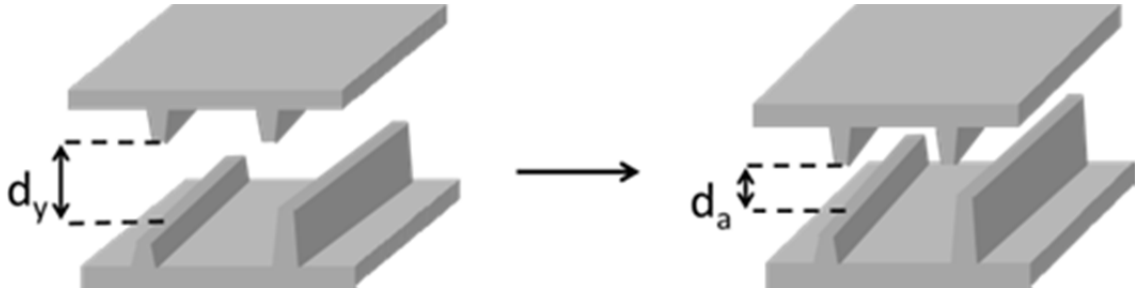

Figure 4.1. Schematic representation of physical aging within CMS structures. The dimensions d_y and d_a correspond to the ultramicropore dimensions of "young" and "aged" CMS, respectively.

A key difference between glassy polymer and CMS materials is that the physical aging in CMS cannot be reversed by high temperature treatment, whereas heating a polymer above the glass transition temperature can "erase" any physical aging, restoring

its original properties (*9*). This fact notwithstanding, obvious similarities exist between the two types of amorphous materials.

While previous aging work focused on both dense and hollow fiber CMS membranes for the challenging ethylene/ethane separation, the current work focuses on the aging of a 6FDA:BPDA-DAM(1:1) hollow fiber CMS membranes formed at a pyrolysis temperature of 550 ^{0}C for the CO_2/CH_4 separation. The higher free volume 6FDA-precursor, compared to Matrimid®, and a low pyrolysis temperature were chosen to form "open" CMS pore structures resulting in the most extreme changes in separation parameters in order to observe the physical aging most readily.

Constant volume permeation measurements were utilized in order to eliminate the chances for adsorptive-based aging. Figure 4.2 summarizes the pure gas permeation experiments used to characterize the physical aging of CMS hollow fiber membranes used in this work for CO_2/CH_4 separations. The initial CO_2/CH_4 separation performance of these CMS membranes is a CO_2 permeance of 273 GPU and an ideal selectivity of 32. After true steady-state permeation was achieved, both the upstream and downstream sides of the membrane module were evacuated for 24 hours, after which permeation measurements were repeated on the aged membrane. Note that after achieving steady-state, as in the case of C_2H_4/C_2H_6, further aging is suppressed as long as the active feed is maintained. Evacuation and exposure to active vacuum amplifies the physical aging phenomena, while eliminating adsorptive-based aging due to any contaminants (*5*). After the initial 24 hour aging period, CO_2 permeance dropped from 273 GPU to 208 GPU, and the selectivity rose from 32 to 37. This process was repeated for another 24 hours, bringing the cumulative aging time to 48 hours, resulting in a CO_2 permeance of 189

GPU and an ideal selectivity of 38. Further exposure of the membrane to active vacuum for a cumulative 22 days results in a CO_2 permeance of 139 GPU and selectivity over methane of 53. Continuing the aging to 4 months (120 days) it is clear that the permeance continues to drop over this time period with the CO_2 permeance dropping to 76 GPU and the ideal selectivity rising to 71. Again, if maintained under active feed, the original performance (273 GPU and selectivity 32) should be essentially maintained, represented by the horizontal dash-dot lines in Figure 4.2 (*5*, *6*), as will be addressed later in Section 4.3.1.

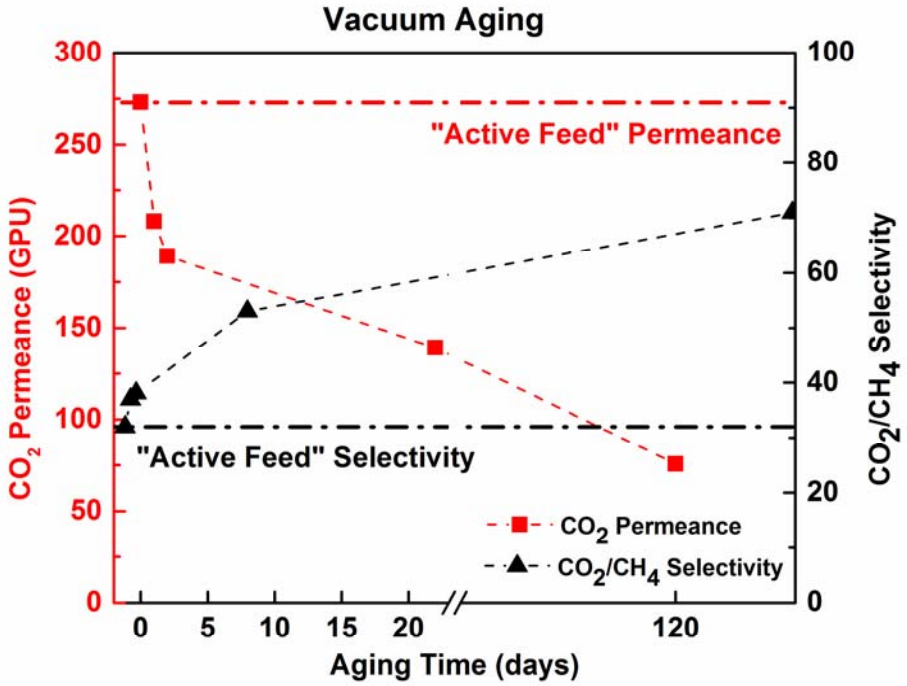

Figure 4.2. Aging of 6FDA:BPDA-DAM 550 ^{0}C CMS fibers under vacuum. Pure gas permeation at 35 ^{0}C, 50 psia. Horizontal dash-dot lines indicate the approximate permeance (red, upper) and selectivity (black, lower) values for a CMS fiber under "active feed" conditions.

4.3 Amine Doping of Carbon Molecular Sieve Membranes

As noted above, when a CMS membrane ages, the relaxation of the plate-like sheets are believed to result in a reduction in the micropore volume and some reduction in ultramicropore dimensions. The CMS post-fabrication are present in a non-equilibrium state, where trapped free volume can decrease over time resulting in a denser packing of the aromatic plates that give rise to micropores, as well as minor changes in the size selective ultramicropore distribution (*10*). Impeding the relaxation of this "nascent" CMS structure should allow for the suppression of the physical aging of the CMS materials.

Previous work showed that CMS membranes exposed to diethylamine (DEA) resulted in almost complete loss of membrane productivity, even after a so-called propylene regeneration method that worked for non-reactive sorbents (*4*). The details of the DEA treated membranes were not explained, but it is hypothesized that the amines may have reacted with the CMS structure forming new covalent bonds that prevented their removal by propylene cleaning.

Combining and extending the findings from these previous studies allows for the conjecture that selective placement of small molecules within the CMS structure may allow for stabilization of the aromatic plates. Exploration of the idea that introduction of small bifunctional amine dopants into the CMS structure may suppress, or even prevent the relaxation of the CMS microstructure was performed in this work. An analogy can be drawn between cross-linking in polymers and amine doping, where formation of covalent bonds between amine dopants and CMS plates may retard rearrangements of the "glassy" CMS structure. An approach that targets the larger ultramicropores (~7 Å) and the

smaller micropores (7-10 Å) should result in CMS materials with essentially unchanged selectivity, leaving the ultramicropores responsible for the CO_2/CH_4 separation unchanged. Control of this treatment could, in principle, prevent large decreases in membrane productivity due to "plugging" of the ultramicropores. We sought to produce doped CMS materials that exhibited similar selectivities with respect to untreated materials, and slightly lower productivities due to the small fraction of ultramicropores being modified by the dopant. As noted later in Section 4.3.1, this vision was found to be different than the ultimate outcome; however, desirable results were found.

This initial study of amine doping uses *p*-phenylene diamine (PPDA), where R = phenyl in Figure 4.3, because of the rigid structure and molecular length of 8.5 Å and cross-section of ~3.4 Å. The thin cross-section allows easy penetration into the CMS structure, while the length is on the order of the large ultramicropores and small micropores that are being targeted with this modification. The rigid structure of PPDA is also attractive to promote modification of adjacent CMS plates, preventing any "back-bonding" that may be associated with a flexible dopant molecule (e.g. aliphatic diamine).

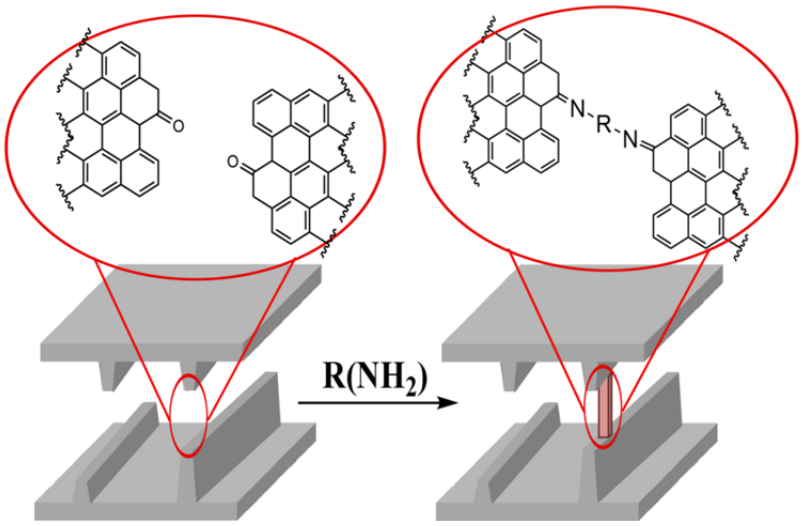

Figure 4.3. Schematic of amine doping concept, using the carbonyl functional groups as example reaction site.

While the specific reactive sites require further clarification, it is hypothesized that primary amines can react with groups likely to be present on the ultramicropore edges, thereby forming new covalent bonds. Figure 4.4 depicts two separate possible reaction schemes for amine doping of CMS materials. The first possible reaction (Figure 4.4-(i)) involves addition of the primary amine to a carbonyl group, resulting in the formation of an imine bond. All CMS materials formed in this study were pyrolyzed to 550 ^{0}C, during which previous studies on similar materials show CO and CO_2 are just starting to be evolved during the pyrolysis process (*11*). It is believed that the materials used in this study will have residual carbonyl functionalities resulting from the low temperature pyrolysis of the polyimides, which may react with the primary amines of the dopant.

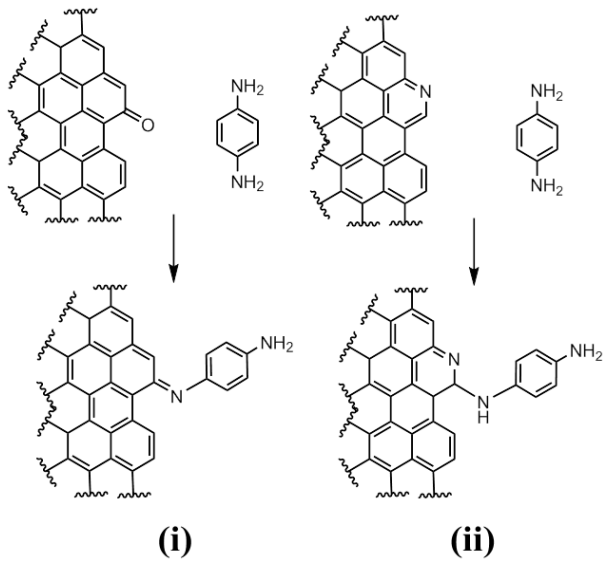

Figure 4.4. Proposed reactions of primary amine dopant with CMS ultramicropore edges. Half reactions shown for brevity, but pendant primary amine will react with another functional group on adjacent CMS ultramicropore edge.

The second hypothetical reaction (Figure 4.4-(ii)) comprises reaction of the amine with a pyridinic moiety in the aromatic CMS structure. Previous studies on the pyrolysis of polyimides showed nitrogen evolution in temperatures >700 ^{0}C, implying that most of the nitrogen from the polymeric backbone remains within CMS material formed at lower temperatures (*11*). Again, with the low pyrolysis temperature used here, it is a reasonable assumption that most, if not all, of the nitrogen from the polyimide precursor will remain in the CMS materials. While determining the exact chemical state of the nitrogen within the CMS will be considered later, many states are clearly possible; pyridinic, pyrollic, and graphitic nitrogen may be present and the example given is only for illustrative purposes. Pyridinic rings can undergo electrophilic substitution at the 2-position, due to the increased electron density near the nitrogen atom. While only strong nucleophiles (e.g. primary amines) will react with pyridine rings, pyridinic rings fused within aromatic

systems lose less aromaticity allowing for a more facile reaction with nucleophiles, as shown in Figure 4.4 (*12*). Work focusing on elucidating the exact chemical species involved in the amine doping of CMS materials will be addressed in Chapter 5.

4.3.1 Permeation Results of Amine Doped Carbon Molecular Sieve Hollow Fiber Membranes

CMS hollow fiber membranes were prepared and treated under three different conditions: 1000 ppm, 100ppm, 10 ppm, and 0 ppm (control) PPDA in THF. Direct comparison of the treatment concentration and effect upon permeation results is compiled and represented in Figure 4.6, where the 2008 Robeson upper bound for CO_2/CH_4 was transformed from Barrer to GPU using a 20 μm separation layer thickness, the average dense skin layer thickness of 6FDA/BPDA-DAM hollow fibers pyrolyzed to 550 ^{0}C in UHP Argon (cf. Figure 4.5). The point labeled "control" represents the CMS fiber that was brought through the doping treatment with only THF, 0 ppm PPDA present. This data shows that the baseline treatment scheme itself has no effect on the change in permeance and selectivity as it falls within the variability envelope of "baseline" or untreated CMS fibers. All the points in Figure 4.6 correspond to the initial, unaged permeance and selectivity values. For the 100 and 10 ppm cases the variability in permeance is very small and not easily distinguished from the markers on the figure.

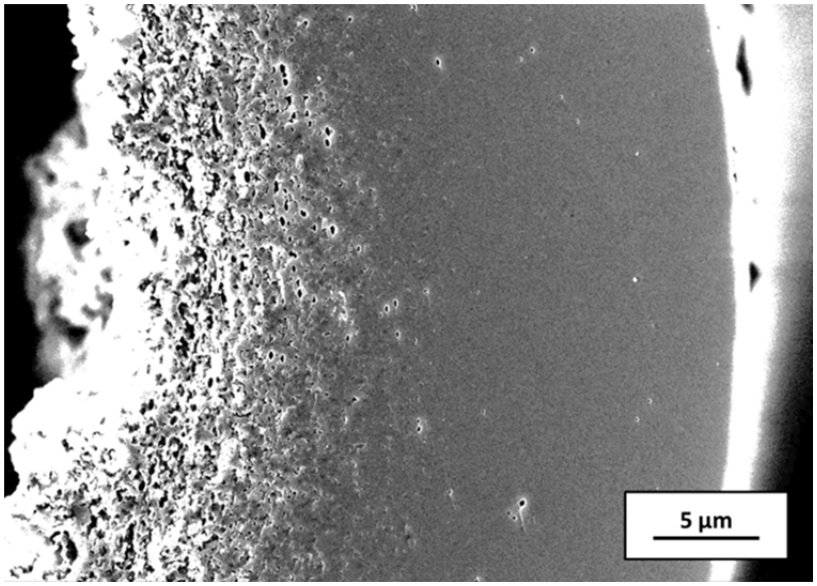

Figure 4.5. Cross section of 6FDA/BPDA-DAM 550 ^{0}C CMS hollow fiber showing an approximate 20 µm skin layer thickness used to convert CO_2/CH_4 upper bound from Barrer to GPU.

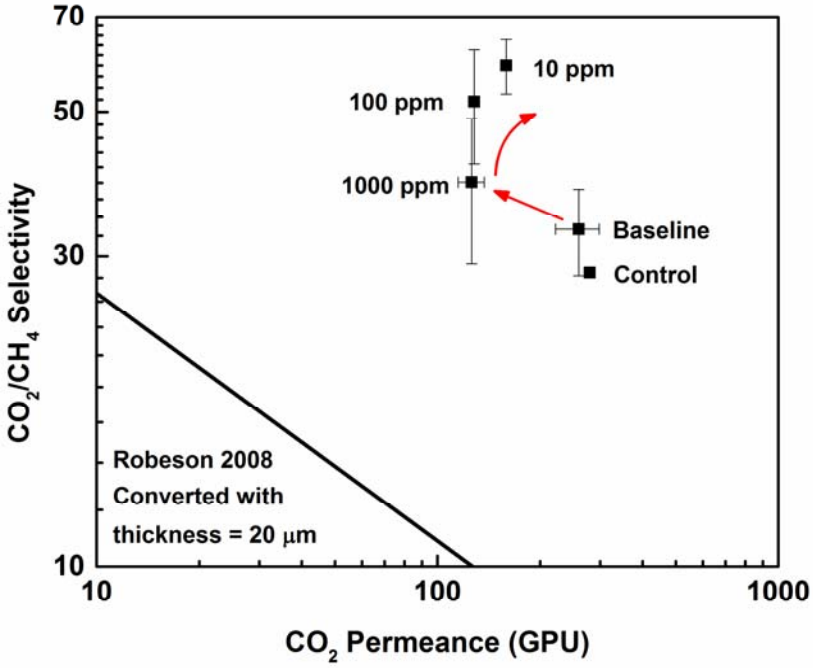

Figure 4.6. Upper-bound performance of PPDA treated CMS materials. Upper-bound transformed from Barrer to GPU by normalizing with a 20 µm thick separation layer.

There is a clear trend between membrane performance and PPDA concentration; as the concentration is reduced both the permeance and selectivity increase. Surprisingly, Figure 4.6 shows there is a significant reduction in permeance with the addition of 1000 ppm PPDA in the treatment solution, but relatively small effect on the selectivity – as expected. Reducing the PPDA concentration allows for the recovery of most of the initial permeance, but is accompanied by an increase in selectivity. As noted, these results were unexpected, as functionalization at the ultramicropores ideally should yield membranes with similar selectivities but with slightly reduced productivities if the simple picture of the CMS morphology is accepted.

Doping at the ultramicropores was hypothesized to result in aged CMS that was permeable, but less-selective, due to the ultramicropores being kept open by the dopant, dimension d_u in Figure 4.7. On the other hand, presence of dopants within the micropore "galleries" was envisioned to result in slightly less permeable, more selective membranes due to the decreased ultramicropore spacing, dimension d_m in Figure 4.7-(ii).

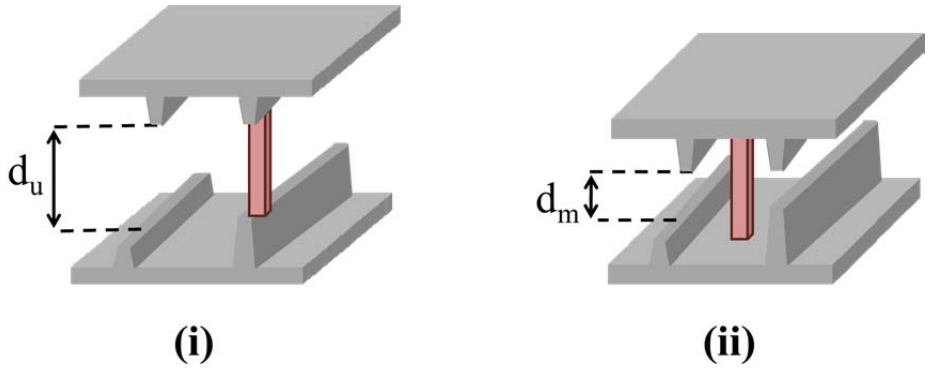

Figure 4.7. Cartoons comparing dopant sites within CMS structure (i) at ultramicropore edges, (ii) within CMS micropore "galleries".

Figure 4.8 show the aging performance of the best performing (10 ppm PPDA treated) CMS membrane. The data represented are the average of at least three separate CMS hollow fiber modules for each condition, except the "baseline 4 months" aged sample is a single module data point. The "baseline initial" column refers to the permeance and selectivity of a CMS fiber that has not been treated with any diamine dopant, and is presented for comparison of the treatment effect upon initial permeance and selectivity values.

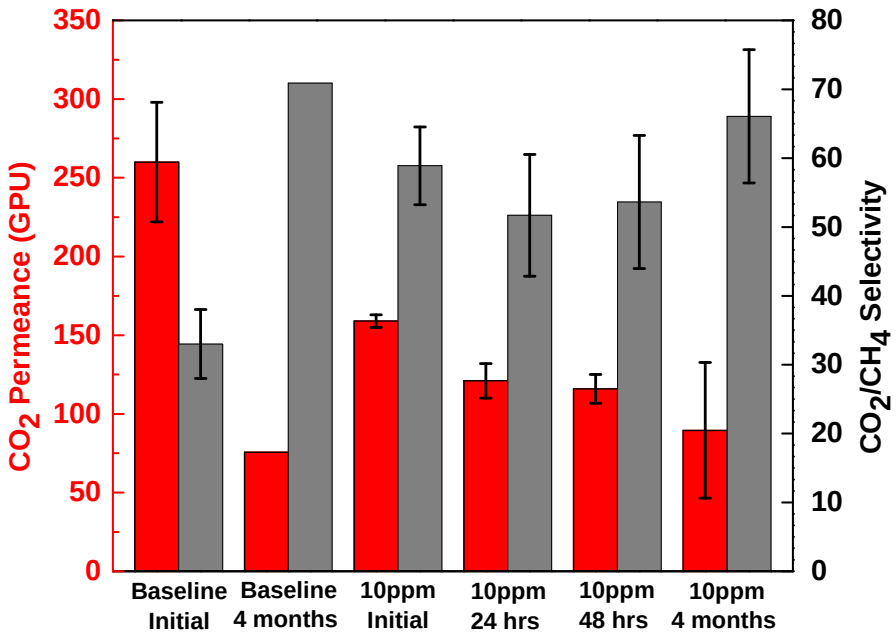

Figure 4.8. Aging of 10 ppm PPDA treated CMS fiber. Pure gas permeation at 35 ^{0}C, 50 psia. Time elapsed refers to exposure periods of active vacuum aging.

The initial permeance is reduced compared to the "baseline" permeance value, but this decrease in permeance for the doped materials is coupled with the unexpected increase in selectivity. When doped CMS fibers are vacuum aged for 24 hours, the typical

decrease in permeance and increase in selectivity occurs, which is characteristic of physical aging of CMS materials. This initial behavior is attributed to the relaxation of the CMS structure that has not been affected by the doping treatment. Upon exposure to another 24 hours of vacuum aging, bringing the cumulative aging time to 48 hours, results in essentially no loss of permeance or gain in selectivity in the doped material. However, further testing of the 10 ppm membranes shows that the treated CMS still physically ages. After exposure to active vacuum for a cumulative 4 months, the CO_2 permeance drops to 90 GPU, while the CO_2/CH_4 selectivity rises to 66. These results show that the amine doping *does not suppress the physical aging*, as was the original goal of this work; after 4 months of vacuum aging the CO_2 permeance and CO_2/CH_4 selectivity of the "baseline" untreated and 10 ppm PPDA treated CMS membranes are comparable. Instead, the amine doping technique acts as a new tool for engineering the separation properties of CMS membranes to achieve a desired separation performance.

The stability of the 10 ppm PPDA treated CMS membrane was observed under a continuous active feed of 50 psia mixed gas of 50% CO_2/50% CH_4 and is presented in Figure 4.9. It is clear from Figure 4.9 that after an initial stabilization period of ~50 hrs, the separation performance of the 10 ppm PPDA treated CMS fibers is essentially stable. After 290 hours of continuous testing the treated fiber retained >85% of the initial permeance while exhibiting a corresponding 9% increase in permselectivity. It is hypothesized that the highly condensable CO_2 in the mixed gas feed has sorbed into the microporous structure, preventing any large-scale relaxation within the CMS structure allowing for suppression of the physical aging. While the mixed gas configuration is not as selective as the pure gas, this fact may be attributed to the competitive adsorption

between the two permeating species in the mixture. Also, due to the high CO_2 permeance, bulk flow effects may come into play reducing the selectivity, which has been shown to be an issue in glassy polyimide membranes with highly condensable penetrants (*13*).

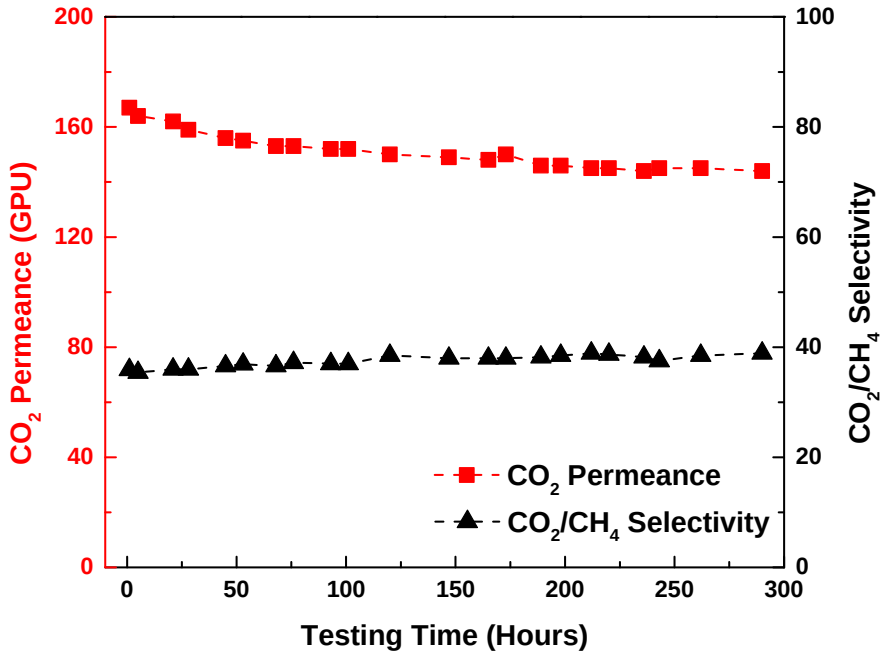

Figure 4.9. Long term mixed gas permeation results of 10 ppm PPDA treated CMS fiber under continuous active feed of 50 psia of mixed gas 50% CO_2/50% CH_4 at 35 ^{0}C.

4.3.2 CO_2 and CH_4 Gas Sorption within Amine Doped Carbon Molecular Sieve Hollow Fiber Membranes

Evidence of amine dopants present within the micropores was probed by performing pressure decay sorption on PPDA treated CMS materials. Materials with dopants present in the micropores will exhibit some reduction in Langmuir sorption capacity caused by the dopant reducing the volume available to the sorbing gas.

Figures 4.10 and 4.11 show the gas sorption isotherms for CO_2 and CH_4, respectively, on CMS materials treated with varying concentrations of the PPDA dopants and the values of Langmuir isotherm parameters fitted are summarized in Table 4.1.

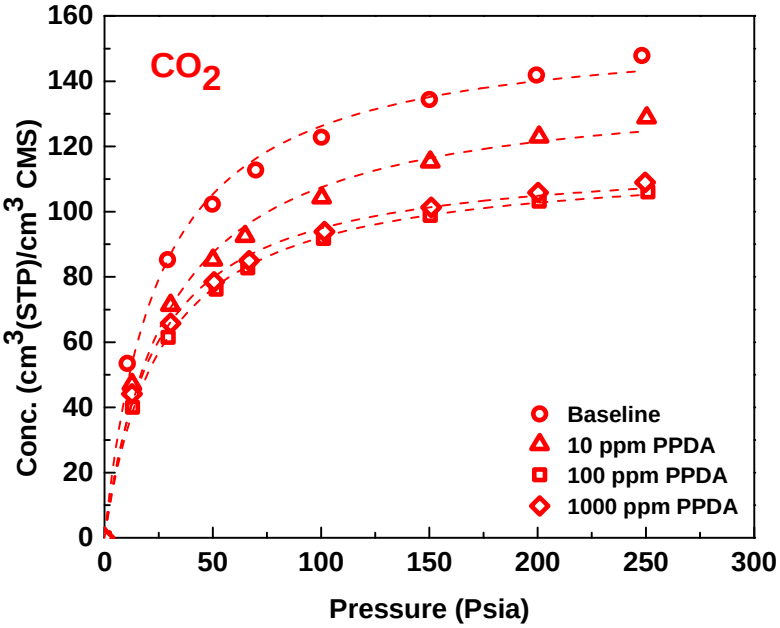

Figure 4.10. Pressure decay sorption isotherms of carbon dioxide on PPDA treated fibers, all tests performed at 35 ^{0}C.

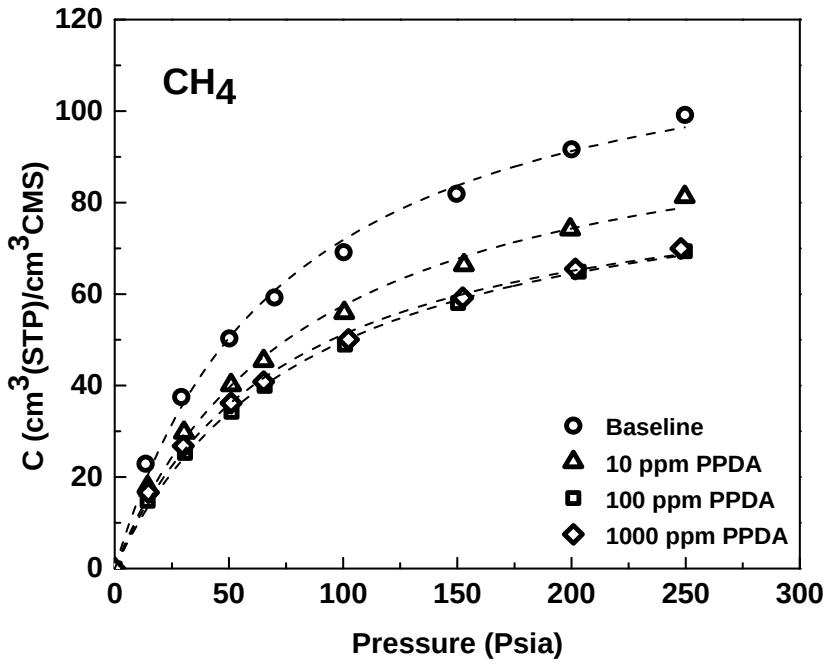

Figure 4.11. Pressure decay sorption isotherms of methane on PPDA treated fibers, all tests performed at 35 ^{0}C.

Table 4.1. Langmuir isotherm parameters of 550 ^{0}C CMS hollow fibers treated with PPDA.

Gas	Concentration	C_H' [cm^3 (STP)/cm^3 CMS]	*b* [1/psia]
CO_2	**Baseline (0 ppm)**	157.35 ± 3.40	0.041 ± 0.004
	10 ppm	139.57 ± 3.28	0.033 ± 0.003
	100 ppm	116.11 ± 0.76	0.038 ± 0.001
	1000 ppm	117.23 ± 1.54	0.042 ± 0.002
CH_4	**Baseline (0 ppm)**	125.08 ± 4.13	0.013 ± 0.001
	10 ppm	105.22 ± 3.31	0.012 ± 0.001
	100 ppm	91.62 ± 1.63	0.011± 0.001
	1000 ppm	89.31 ± 2.16	0.013 ± 0.001

As expected, CO_2 shows a higher hole filling capacity C_H' and higher affinity constant *b* than CH_4, due to the condensability of CO_2, reflected by the relative critical temperatures (304 K for CO_2 and 191 K for CH_4). This trend is true across all of the CMS materials in this study, independent of PPDA doping conditions. The hole filling capacity (C_H') decreases with increasing PPDA concentration, an indication of amine dopants present

within the micropore galleries. The sorption of both CO_2 and CH_4 is essentially identical for the 100 ppm and 1000 ppm cases, suggesting that the 100 ppm condition saturates the CMS structure with PPDA dopants. This trend is also supported by the permeation data presented in Figure 4.7, where the CO_2 permeance of 100 ppm and 1000 ppm PDDA lie within the experimental uncertainty of the data.

The sorption coefficients of PPDA treated CMS hollow fibers are shown in Table 4.2. The sorption selectivity of PPDA treated CMS membranes remains unchanged with increasing PPDA concentration. This is believed to be due to the presence of the PPDA dopant within some of the micropores, thereby equally preventing the sorption of both penetrants. These results show that the amine doping treatment is much more complex than originally hypothesized; that there appear to be dopants present in both ultramicropores and micropores, which will be addressed later.

Table 4.2. Sorption of 550 ^{0}C CMS hollow fibers treated with PPDA at 35 ^{0}C, 50 psia.

Concentration	$\mathbb{S}_{CO_2}$ **[cm^3 (STP)/ (cm^3 CMS-psia)]**	$\mathbb{S}_{CH_4}$ **CH4[cm^3 (STP)/ (cm^3 CMS-psia)]**	$\alpha_{\mathbb{S}}$
Baseline (0 ppm)	2.11 ± 0.28	1.00 ± 0.13	2.09 ± 0.38
10 ppm	1.75 ± 0.23	0.79 ± 0.09	2.21 ± 0.38
100 ppm	1.53 ± 0.36	0.68 ± 0.09	2.24 ± 0.17
1000 ppm	1.59 ± 0.13	0.72 ± 0.07	2.22 ± 0.27

Application of Equation 4.1 allows for estimation of diffusional selectivity for the PPDA amine doped CMS membranes, and is shown in Figure 4.12. The increase in diffusional selectivity with reduced PPDA concentration is attributed to a CMS structure with increased micropore volume available for the gas sorption, leading to higher permeation rates. The changes in diffusional selectivity with amine doping may allow

this treatment to act as a tool to engineer the separation properties of a given CMS material.

$$\alpha_{A/B} = \frac{\overline{D}_A}{\overline{D}_B} \times \frac{\overline{\mathbb{S}}_A}{\overline{\mathbb{S}}_B} = \alpha_D \times \alpha_S \tag{4.1}$$

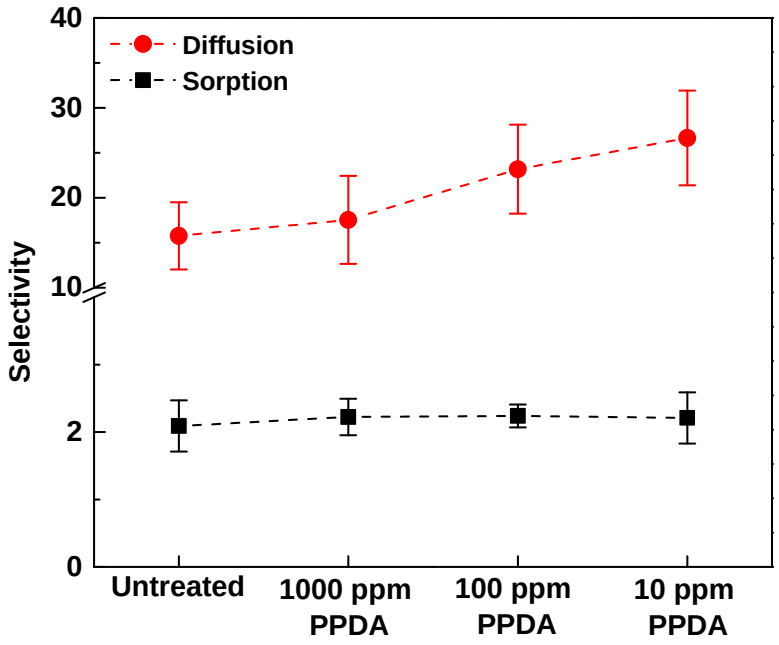

Figure 4.12. Sorption and Diffusional Selectivity of PPDA doped CMS. Diffusional selectivity estimated via Equation 2.1 from experimentally measured permselectivity and sorption selectivity.

4.4 Amine Doping as a New Modification Technique for Carbon Molecular Sieve Membranes

The permeation and gas sorption analysis presented above indicate that the amine doping technique is more complex than initially hypothesized. The reduction in sorption capacity for both penetrant gases and increased diffusional selectivity does not follow the

simple originally suggested selective modification of the ultramicropore edges shown in Figure 4.7-– (i).

The turbostratic structure of amorphous carbon materials, like CMS, have been previously described as aggregates of sp^2-hybridized entities (*14*). The packing imperfections between these crystallites give rise to the rather simplistic dual mode pore size distribution that is responsible for the molecular sieving nature of CMS membranes. A cartoon schematic of the aromatic plates is represented in the bottom middle of Figure 4.13 below, reminiscent of the currently accepted view of the CMS structure discussed in Chapter 2.

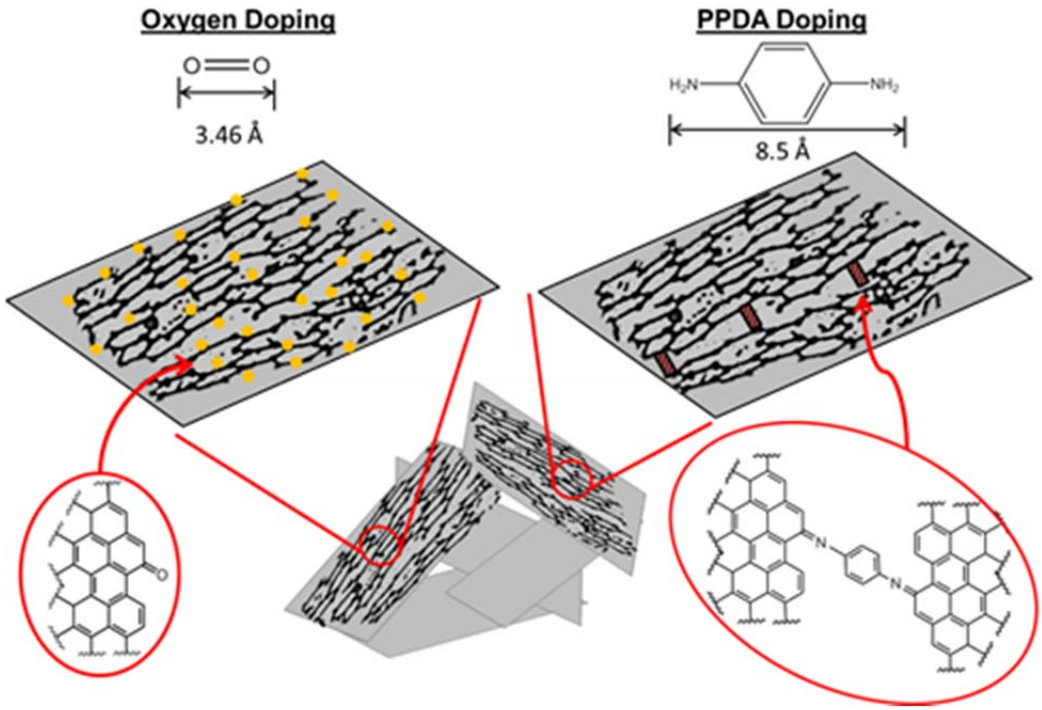

Figure 4.13. Comparison of oxygen and amine doping in CMS membranes. Molecular oxygen can sample more pore space due to a smaller kinetic diameter. PPDA molecules will be restricted to functionalization of larger ultramicropores because of the larger, bulkier molecule being used.

It is apparent from the permeation results summarized in Figure 4.6, that the amine doping is a new technique for the selective tuning of membrane separation parameters, similar to that of previously reported oxygen doping in CMS membranes (*15–17*). Oxygen doping appears to decorate the CMS ultramicropore edges by the dissociation of trace amounts of oxygen present within the pyrolysis atmosphere, which can even be generated during decomposition of the imide link. The resulting carbonyl groups lead to a reduction in the average ultramicropore distance, causing the membranes to be more selective, but less productive. Kiyono *et. al.* established that there is a fine balance between oxygen exposure and membrane performance, showing that high oxygen concentrations can result in undesirable performance (*16*). Oxygen and related H_2O or CO decomposition products have access to more ultramicropore volume, owing to their small molecular size. Clearly molecular oxygen has access to much smaller ultramicropores than a larger doping agent, and higher concentrations of oxygen result in a higher degree of molecular doping.

Amine doping can be envisioned to be analogous, and possibly complementary, to oxygen doping, but utilizing a larger dopant molecule and different chemistry. Figure 4.13 schematically differentiates oxygen and amine doping. As mentioned previously, oxygen can access the smaller ultramicropores due to its small kinetic diameter; meanwhile the larger PPDA molecule will not be able to access these smaller ultramicropores. If this simple reasoning is accepted, it can be envisioned that the amine dopants will act as a means for selectively modifying “large” ultramicropores and “small” micropores, schematically represented in Figure 4.14 below. Recalling that ultramicropores are defined as having sizes <7 Å, removal of “large” ultramicropores

(e.g. 5-7 Å) in the scope of CO_2/CH_4 separation, would eliminate pores that are not adding any significant transport resistance to either molecule. Elimination of these pathways would reduce the overall productivity of the membrane by forcing penetrants to travel through more selective pathways, increasing the overall membrane selectivity. The amine dopants are not creating a more tortuous path per se, but rather selectively removing high throughput, less selective channels present within the CMS structures along with some sorption capacity reduction. Placement of an amine dopant within a large ultramicropore or small micropore will result in removal of these paths of little transport resistance or selectivity, and is schematically represented by the shaded blue area in Figure 4.14 below. This idea is further supported by the data represented in Figure 4.6, where adding small amounts of PPDA leads to a reduction in permeance and increase in selectivity, while still maintaining attractive performance.

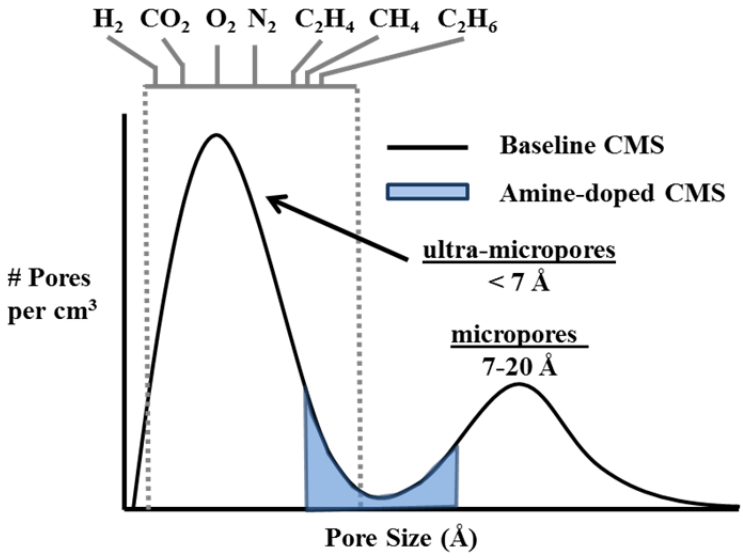

Figure 4.14. Idealized bimodal pore size distribution present within CMS materials. Blue shaded region corresponds to cross-over regime of "large" ultramicropores and "small" micropores.

Further clarification of the amine doping technique will be discussed in Chapter 5; however, the sorption results above suggest that there are dopant molecules present within micropores responsible for gas sorption. Extending the arguments used above for modification of "large" ultramicropores, a similar analysis can be applied to "small" micropores, where micropores on the order of 7-10 Å may be functionalized by the PPDA molecule (molecular dimension ~8.5 Å). Provided this reasoning is correct, amine doping provides a new technique to tune the pores present within the "cross-over" of micropore to ultramicropore regime. These pores, while not selective enough for molecular sieving of CO_2 or CH_4, may be more important in separations of larger penetrants (e.g. light olefins and paraffins) which lie on the upper end of the ultramicropore distribution, as illustrated in Figure 4.14.

4.5 TGA-IR Analysis of Amine Doped Carbon Molecular Sieve Hollow Fiber Membranes

To test the stability of the PPDA dopants within the CMS hollow fiber structures, the PPDA treated samples were reheated to the final pyrolysis temperature (550 ^{0}C) while analyzing the evolved gas with a FTIR spectrometer. Figure 4.15 shows the TGA-IR analysis of the 10 ppm PPDA treated CMS fibers. This trace shows two prevalent mass losses: the first corresponding to the removal of adsorbed atmospheric CO_2 and H_2O while heating the sample to 110 ^{0}C, the second mass change occurs during the second heating phase at approximately 220 ^{0}C. Examining Figure 4.16, the time-lapsed IR spectra of the evolved gases, shows the presence of an IR-active species evolved from the CMS material. Focusing on the IR spectra at 57 minutes, Figure 4.17 shows the

characteristic peaks of trace tetrahydrofuran (THF), the solvent used for the treatments (*18*).

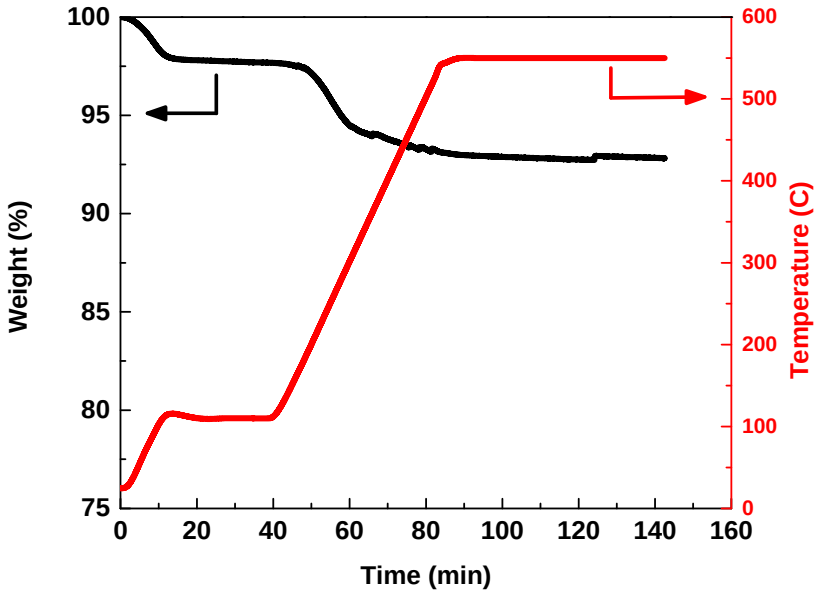

Figure 4.15. TGA Profile for 10 ppm PPDA treated CMS fibers reheated to 550 ^{0}C.

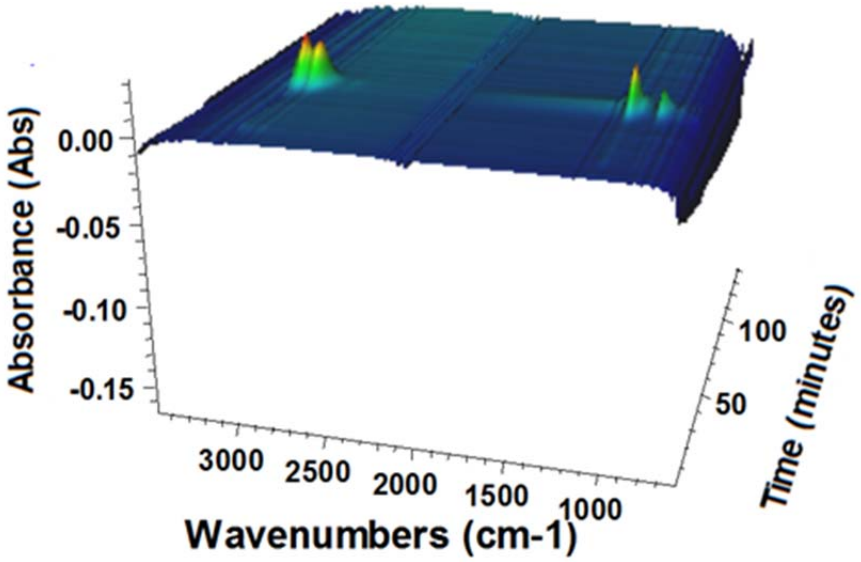

Figure 4.16. TGA-IR 3D spectra of 10 ppm PPDA treated CMS fibers.

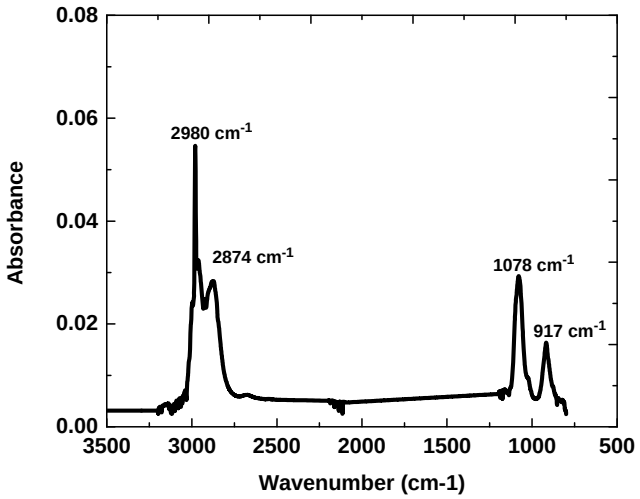

Figure 4.17. FTIR Spectra of peak at 57min in TGA-IR Run corresponding to the spectra of THF: C-H Stretches at 2980 and 2874 cm^{-1}, C-O-C stretch at 1078 cm^{-1} (asymmetric) and 917 cm^{-1} (symmetric).

The lack of IR active species in later times of the TGA reheating of the treated CMS fibers suggest that the PPDA dopant has formed a new covalent bond with the CMS structure.

4.6 Summary and Conclusions

This study has addressed the physical aging of CMS hollow fiber membranes for natural gas separations and introduces a new post-synthetic amine doping modification technique with the original goal of suppressing the physical aging. Exposing CMS membranes to a THF solution containing small amounts of PPDA resulted in an unexpected increase in CO_2/CH_4 selectivity, coupled with a small decrease in productivity. Long term exposure of the amine doped membranes to active vacuum demonstrated that the treatment did not suppress the physical aging. While the doped

membranes are lower in productivity than an untreated membrane they still have attractive separation performance, lying above a pseudo upper-bound line developed for hollow fiber membranes. The reduced productivity, coupled with an increase in selectivity, shows that the doping mechanism is more complex than originally hypothesized, with doping likely taking place at both the ultramicropore and micropore sites. Thermogravimetric analysis of the samples and the evolved gas shows that only the THF treatment solvent is evolved from the doped CMS membranes, suggesting the amine dopants are covalently bonded within the CMS structure.

4.7 References

(1) Lagorsse, S.; Magalhães, F. D.; Mendes, A. Aging study of carbon molecular sieve membranes. *J. Memb. Sci.* **2008**, *310*, 494–502.

(2) Menendez, I.; Fuertes, A. B. Aging of carbon membranes under different environments. *Carbon* **2001**, *39*, 733–740.

(3) Jones, C. W.; Koros, W. J. Characterization of ultramicroporous carbon membranes with humidified feeds. *Ind. Eng. Chem. Res.* **1995**, *34*, 158–163.

(4) Jones, C. W.; Koros, W. J. Carbon molecular sieve gas separation membranes-II. Regeneration following organic exposure. *Carbon* **1994**, *32*, 1427–1432.

(5) Xu, L.; Rungta, M.; Hessler, J. V.; Qiu, W.; Brayden, M.; Martinez, M.; Barbay, G.; Koros, W. J. Physical aging in carbon molecular sieve membranes. *Carbon* **2014**, *80*, 155–166.

(6) Fu, S.; Sanders, E. S.; Kulkarni, S. S.; Koros, W. J. Carbon molecular sieve membrane structure–property relationships for four novel 6FDA based polyimide precursors. *J. Memb. Sci.* **2015**, *487*, 60–73.

(7) Steel, K. M.; Koros, W. J. Investigation of Porosity of Carbon Materials and Related Effects On Gas Separation Properties. *Carbon* **2003**, *41*, 253–266.

(8) Steel, K. M.; Koros, W. J. An investigation of the effects of pyrolysis parameters on gas separation properties of carbon materials. *Carbon* **2005**, *43*, 1843–1856.

(9) Huang, Y.; Paul, D. R. Experimental methods for tracking physical aging of thin glassy polymer films by gas permeation. *J. Memb. Sci.* **2004**, *244*, 167–178.

(10) Oberlin, A. Carbonization and graphitization. *Carbon* **1984**, *22*, 521–541.

(11) Hatori, H.; Yamada, Y.; Shiraishi, M.; Yoshihara, M.; Kimura, T. The mechanism of polyimide pyrolysis in the early stage. *Carbon* **1996**, *34*, 201–208.

(12) Katritzky, A. R.; Ramsden, C. A.; Joule, J. A.; Zhdankin, V. V. *Handbook of Heterocyclic Chemistry (3rd Edition)*; Elsevier, 2010.

(13) Das, M.; Koros, W. J. Performance of 6FDA-6FpDA polyimide for propylene/propane separations. *J. Memb. Sci.* **2010**, *365*, 399–408.

(14) Pierson, H. O. *Handbook of carbon, graphite, diamond and fullerenes: Properties, Processing, and Applications*; Noyes Publications: Park Ridge, NJ., 1993.

(15) Kiyono, M.; Williams, P. J.; Koros, W. J. Generalization of effect of oxygen exposure on formation and performance of carbon molecular sieve membranes. *Carbon* **2010**, *48*, 4442–4449.

(16) Kiyono, M.; Williams, P. J.; Koros, W. J. Effect of Pyrolysis Atmosphere on Separation Performance of Carbon Molecular Sieve Membranes. *J. Memb. Sci.* **2010**, *359*, 2–10.

(17) Kiyono, M.; Williams, P. J.; Koros, W. J. Effect of polymer precursors on carbon molecular sieve structure and separation performance properties. *Carbon* **2010**, *48*, 4432–4441.

(18) Kilimov, A. P.; Svechnikova, M. A.; Shevchenko, V. I.; Smirnov, V. V.; Zotov, S. B.; Kvasnyuk-Mudryi, F. V. Infrared spectra of cyclic ethers and their derivatives. *Chem. Heterocycl. Compd.* **1967**, *3*, 579–584.

CHAPTER 5. ROLE OF SIZE AND FUNCTIONALIITY OF AMINE DOPANTS FOR MODIFICATION OF CARBON MOLECULAR SIEVE STRUCTURE

5.1 Overview

The work in this chapter seeks to extend the amine doping treatment introduced in Chapter 4, where dopant size and reactivity will be examined to connect amine dopant type and performance of resulting carbon molecular sieves (CMS). The preliminary work in Chapter 4 focused on *p*-phenylenediamine (PPDA), selected due to its rigid aromatic structure, promoting modification of adjacent CMS plates and preventing possible "back bonding" that may be associated with more flexible amine dopants (e.g. aliphatic diamines). While a variety of structures could be used in expansion of this technique, dopants similar in size to PPDA were chosen as to target functionalization of pores that lie in the "cross-over" regime between ultramicropores and micropores, as shown in the blue area in Figure 5.1 below.

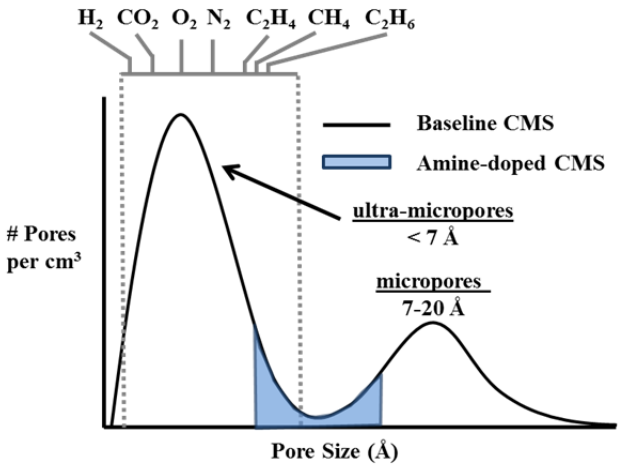

Figure 5.1. Idealized bimodal pore size distribution of CMS materials where shaded area identifies the "cross-over" regime between ultramicropores and micropores.

This area is of particular interest as these pores are not directly responsible for molecular sieving of smaller gases like CO_2 and CH_4 (kinetic diameters of 3.3 Å and 3.8 Å, respectively); however, modification could result in sharpening of the upper end of the ultramicropore distribution and lower end of the micropore distribution, leading to enhancements in separation performance for smaller penetrants. Additionally, this methodology could be of particular interest for tuning CMS materials for larger gas penetrants, which rely heavily on the upper end of the ultramicropore distribution. Separation of larger penetrants depends on successful engineering of CMS materials to allow diffusional jumps by larger more compact penetrants without losing size and shape selectivity over less compact penetrants. Therefore, tuning of these larger diffusion-controlling pores may give insight into this complex regime, noted in Figure 5.1. In fact, the larger ultramicropores may not be “slits” but rather small packing imperfections associated with the aromatic plates that comprise a CMS material and will be discussed later.

In this work, CMS membranes will be treated with a small collection of carefully selected amine dopants. Transport measurements of CO_2, CH_4, C_3H_6, and C_3H_8 will be utilized in hopes of establishing a relationship between dopant structure and resulting amine treated CMS membrane performance.

5.2 Dopant Selection: Structure and Reactivity

Figure 5.2 – (i) presents *p*-phenylenediamine (PPDA) and will serve as the base structure from which complementary amine dopant molecules were selected for this study. In order to test the effects of increased amine reactivity, while maintaining similar overall structure, 1,4-diaminocyclohexane (Figure 5.2 – (ii), PCDA) was selected. Additionally, while the PCDA has a 6-membered ring like PPDA, the more flexible aliphatic ring may allow for penetration farther into smaller pore regimes than available to the rigid aromatic ring.

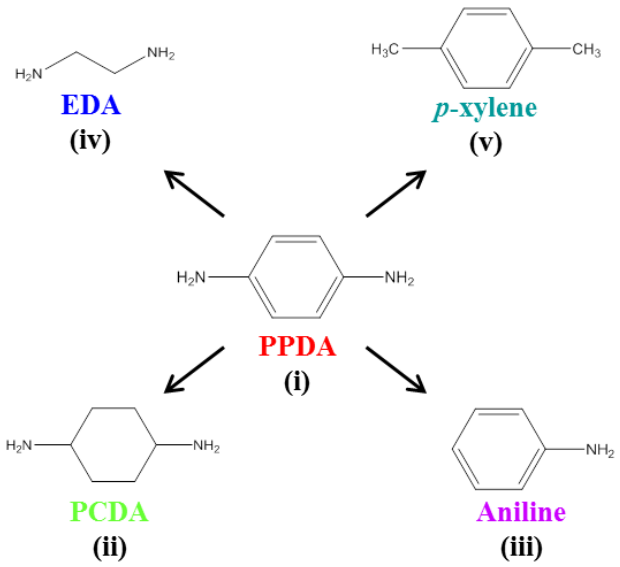

Figure 5.2. Amine dopants selected for this study: (i) *p*-phenylenediamine (PPDA), (ii) 1,4-diaminocyclohexane (PCDA), (iii) aniline, (iv) ethylene diamine (EDA), and (iv) *p*-xylene.

Recalling the interplay between dopant concentration and resulting performance suggested this approach as a new tuning tool for CMS membranes, similar to that of previously developed oxygen doping (*1*). As a modification technique, diamine dopants may not be necessary, as a mono-amine will contain the same functionality believed to chemically react with the CMS structure. Results from Jones and Koros, which in part initially motivated this work, showed that exposure of CMS membranes to an air stream saturated with diethylamine (single, secondary amine) caused complete loss of membrane performance (*2*). While they did not speculate on the nature of the amine within the CMS structure, it is suggested here that the amine was covalently bound to the CMS membrane. Treating CMS membranes with aniline (Figure 5.2 – (iii)), the mono-amine analogue to PPDA, will allow for comparison in separation performance of mono versus diamine dopants.

To this point, all of the selected amines are similar 6-membered ring structures, allowing for comparison between reactivity and flexibility. However, it can be envisioned that a small flexible amine dopant, like ethylene diamine (Figure 5.2 – (iv), EDA), can sample a population of pores not accessible to the larger dopants (i.e. PCDA and PPDA), resulting in increased separation efficiency compared to materials treated with larger dopants.

Finally, a "control" dopant has been selected to investigate the role of the reactive amine functionality present within all the previously mentioned dopants. *P*-xylene (Figure 5.2 – (v)) serves as an ideal candidate for this purpose, as it is identical in molecular size and rigidity with the base PPDA diamine dopant, but lacks the reactive amine groups.

Table 5.1. Table summarizing physical and chemical parameters of dopants investigated in this work.

Chemical Name (Abbreviation)	**Length[1] (Å)**	**Thickness[1] (Å)**	**pKa[2]**
p-phenylenediamine (PPDA)	8.5	3.4	6.17
1,4-diaminocyclohexane (PCDA)	8.5	4.0	10.78
Ethylenediamine (EDA)	5.6 - 6.7	3.6	9.98
Aniline	7.8	3.4	4.61
p-xylene	8.5	3.4	--

[1]Estimated via CPK models with calibrated ruler. [2]Predicted with ACD Software V11.02.

5.3 Permeation Results of Amine Doped Carbon Molecular Sieve Membranes for the CO_2/CH_4 Separation

In this section, results of treatments with reactive amine dopants (Figure 5.2 - (i)-(iv)) on gas separation performance of CMS membranes for CO_2/CH_4 will be investigated. Performance relating to treatments with the *p*-xylene "control" will be covered later in this discussion. For all cases investigated CMS membranes were prepared from 6FDA:BPDA-DAM(1:1) pyrolyzed under UHP Ar to 550 °C and treated with the desired amine dopant. Recalling in Chapter 4 that CMS membranes treated with 10 ppm PPDA in THF were found to provide the most attractive performance of conditions tested, identical conditions were used in this study in order to investigate the roles of dopant size and reactivity, not concentration. In other words, molar concentrations of the complementary amine dopants studied here were chosen to be equivalent to the molar concentration corresponding to 10 ppm PPDA in THF. Results from these treatments are reported in Figure 5.3 below, plotted against the Robeson 2008 upper-bound for CO_2/CH_4 which has been converted from Barrer to GPU as previously described in Chapter 4 (*3*).

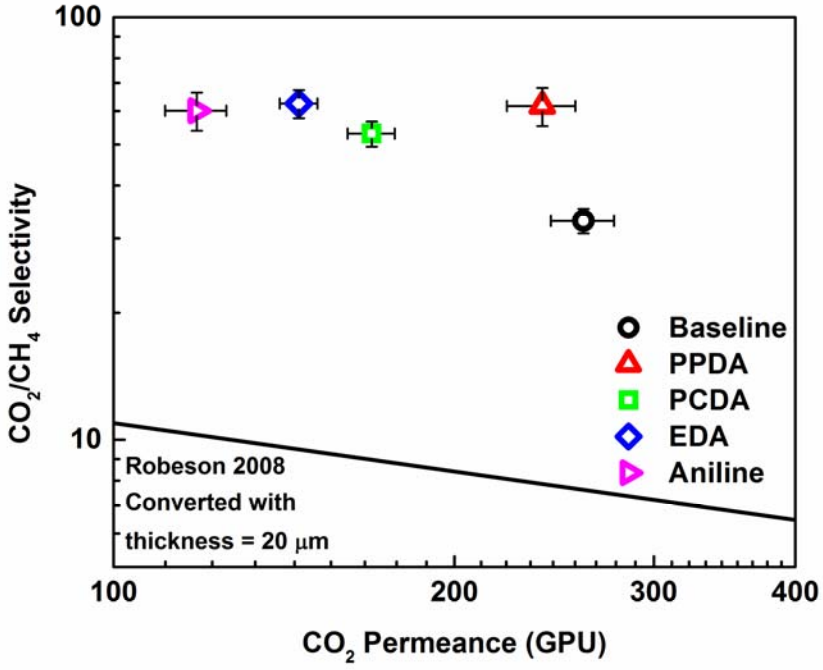

Figure 5.3. Pure gas CO_2 and CH_4 permeation results of CMS hollow fiber membranes treated different amine dopants, tests performed at 50 psia and 35 ºC. Solid line represents the 2008 CO_2/CH_4 Robeson upper-bound transformed from Barrer to GPU using a 20 μm separation skin layer thickness (*3*).

Examining Figure 5.3 shows that regardless of amine dopant structure, treated membranes exhibit higher selectivities coupled with a lower permeance values compared to the untreated baseline material. CMS membranes treated with the more flexible PCDA dopant exhibit ~30% decrease in CO_2 permeance compared to PPDA treated CMS, suggesting increased flexibility leads to higher accessibility of pores within the cross-over regime highlighted in Figure 5.1. However, the increased accessibility of PCDA does not significantly impact CO_2/CH_4 selectivity when compared to PPDA treated CMS.

Treatment of CMS membranes with the smaller more compact EDA results in a ~40% lower CO_2 permeance compared to PPDA treated membranes. This result is not

surprising, as the small flexible EDA (cf. Table 5.1) should be able to access smaller pores within the CMS structure than any other material. While the permeance for the EDA treated CMS is lower than PCDA ("large" cyclic aliphatic amine) treated CMS, the CO_2/CH_4 selectivity shows minimal improvement over either PCDA or PPDA treated CMS. While unexpected, this result may be explained by the linear aliphatic EDA having a significantly smaller cross-section for the penetrant gases (CO_2 and CH_4) to encounter compared to the 6-membered ring dopants. Clearly the more compact EDA is able to access smaller ultramicropores versus the larger 6-membered ring dopants. This capability may allow EDA to tune membrane selectivity with moderate permeance reductions, similar to previously described oxygen doping.

Impacts of mono versus diamine dopant structure can be examined by comparison of CMS membranes treated with aniline and PPDA. Of the dopants investigated in this study, aniline treated CMS membranes exhibit the lowest productivity showing a ~50% drop in CO_2 permeance compared to PPDA treated membranes. Due to its smaller size, aniline is able to sample more pores within the large ultramicropore cross-over regime, similar to the small flexible EDA. However, its bulkier cross-section will result in more transport resistance for both molecules, causing this further reduction in productivity.

5.4 Impacts of Amine Dopants on CO_2 and CH_4 Gas Sorption within Carbon Molecular Sieve Membranes

Further investigation of amine dopant structure upon CMS membrane performance were examined via gas sorption measurements, where Figure 5.4 and Figure 5.5 present the sorption isotherms for CO_2 and CH_4 on CMS materials treated with the different amine dopants, respectively.

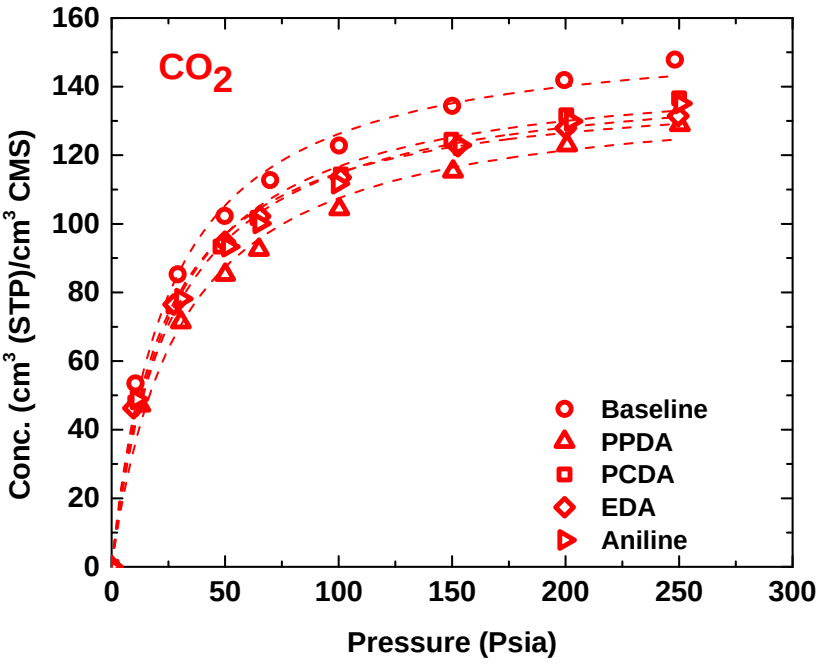

Figure 5.4. Pressure decay sorption isotherms of CO_2 on amine treated CMS hollow fibers, all tests performed at 35 °C. Dashed lines represent Langmuir fit.

Table 5.2. Langmuir isotherm parameters of 550 ^{0}C CMS hollow fibers treated with varying amine dopants.

Gas	Dopant	C_H' [cm^3 (STP)/cm^3 CMS]	*b* [1/psia]
CO_2	**Baseline**	157.35 ± 3.40	0.041 ± 0.004
	PPDA	139.57 ± 3.28	0.033 ± 0.003
	PCDA	146.69 ± 2.78	0.039 ± 0.003
	EDA	140.90 ± 2.02	0.044 ± 0.003
	Aniline	145.00 ± 3.06	0.038 ± 0.003
CH_4	**Baseline**	125.08 ± 4.13	0.013 ± 0.001
	PPDA	105.22 ± 3.31	0.012 ± 0.001
	PCDA	109.62 ± 2.64	0.014 ± 0.001
	EDA	104.33 ± 2.19	0.015 ± 0.001
	Aniline	108.56 ± 2.58	0.014 ± 0.001

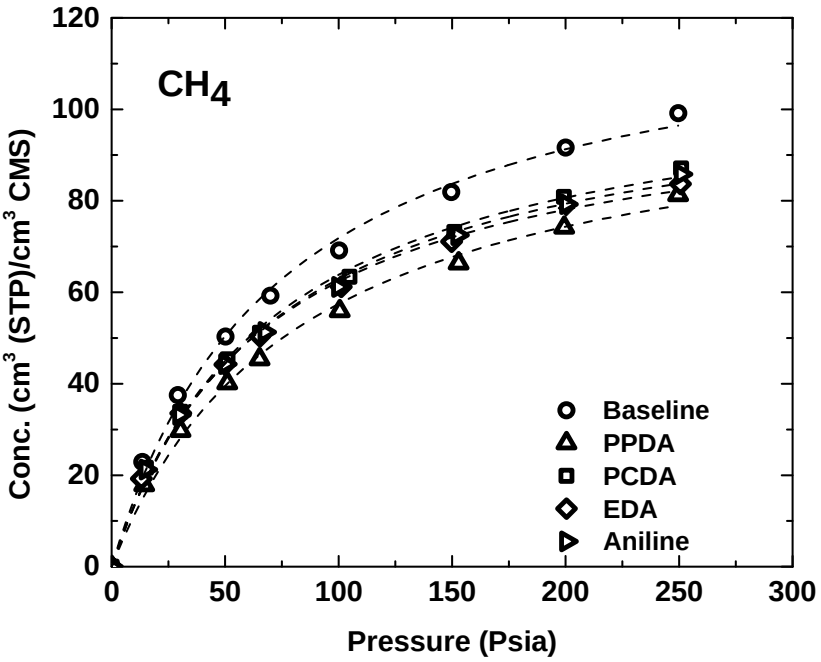

Figure 5.5. Pressure decay sorption isotherms of CH_4 on amine treated CMS hollow fibers, all tests performed at 35 °C. Dashed lines represent Langmuir fit.

As expected, the more condensable CO_2 shows a higher equilibrium sorption uptake than CH_4, where condensability is reflected by the critical temperatures of 304 K 191 K for CO_2 and CH_4, respectively. This is further supported by the Langmuir fit parameters shown in Table 5.2, where higher $C_H^{'}$ and b values for CO_2 indicate both increased volume sorbed within the material and increased affinity, respectively, compared to CH_4. These trends hold for all CMS materials tested in this work, regardless of the presence or structure of amine dopants. Addition of amine dopants results in some reductions of $C_H^{'}$ for both CO_2 and CH_4 regardless of amine structure, indicating amine dopants are present within a small population of the micropore galleries.

Table 5.3. Sorption coefficients and sorption selectivity of CMS hollow fibers treated with varying amine dopants at 35 ^{0}C, 50 psia.

Amine Dopant	$\mathbb{S}_{CO_2}$ [cm^3 (STP)/ (cm^3 CMS-psia)]	$\mathbb{S}_{CH_4}$ [cm^3 (STP)/ (cm^3 CMS-psia)]	$\alpha_{\mathbb{S}}$
Baseline	2.11 ± 0.28	1.00 ± 0.13	2.09 ± 0.38
PPDA	1.75 ± 0.23	0.79 ± 0.09	2.21 ± 0.38
PCDA	1.94 ± 0.22	0.90 ± 0.08	2.15 ± 0.31
EDA	1.94 ± 0.17	0.89 ± 0.07	2.18 ± 0.27
Aniline	1.90 ± 0.23	0.90 ± 0.08	2.11 ± 0.33

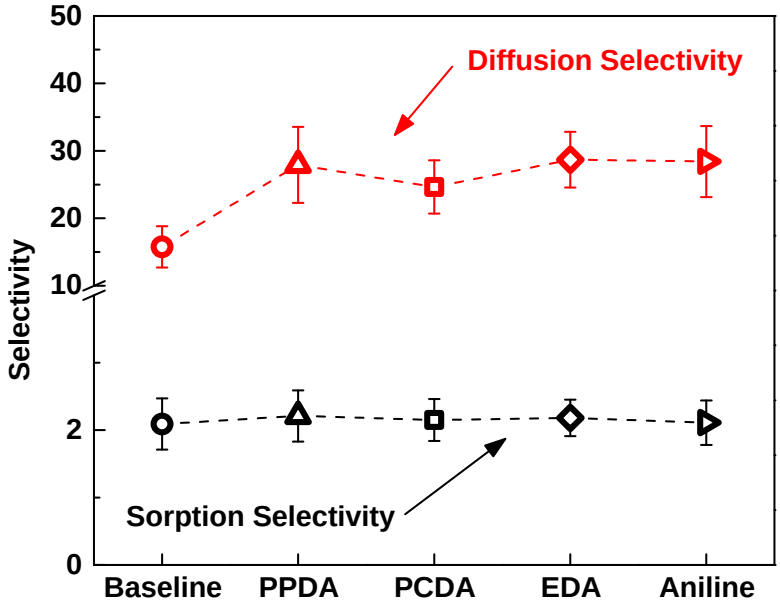

Figure 5.6. Sorption and diffusional selectivity of CMS membranes treated with varying amine dopants.

Table 5.3 summarizes sorption coefficients and sorption selectivity for CMS membranes treated with different amine dopants for the CO_2/CH_4 gas pair. Due to the reduction in measured sorption capacity for both gases, sorption coefficients are also reduced, regardless of the presence or structure of amine dopant. Sorption selectivity for the treated CMS membranes is essentially identical to that of the untreated baseline

material, indicating that amine dopants are not enhancing the attraction between CO_2 and modified membranes but rather altering the porosity of the CMS materials. As permeation performance is dependent upon both sorption and diffusion, this suggests the permselectivity enhancement shown in Figure 5.3 is due to increased diffusional selectivity within treated materials. Diffusional selectivities for amine treated CMS membranes can be estimated from experimentally measured permeation and sorption selectivities, and are presented in Figure 5.6. As expected, amine treated CMS membranes exhibit increased diffusional selectivities; however, regardless of amine dopant used in this study, treated membranes exhibit similar diffusional selectivities. This result is consistent with Figure 5.3 that shows the CO_2/CH_4 permeation performance of amine doped CMS displays similar permselectivities regardless of dopant structure.

These results, therefore, suggest that for the CO_2/CH_4 separation considered here, a small population of pores within the targeted ultramicropore-micropore "cross-over" regime of CMS materials act as pathways with little, to no transport resistance for either molecule. Selective functionalization of these sites to reduce CH_4 diffusive jumps leads to an increased permselectivity coupled with a decrease in permeance. However, within the small group of similarly sized amine dopants selected here, structure seems to only affect permeance not selectivity when treated under identical conditions (i.e. amine concentration). Therefore, it is of interest to expose different, larger gases to amine treated CMS materials as they will be able to provide more insight into the upper-end of the ultramicropore distribution, which will be considered later in this discussion.

5.5 Stability of Amine Doped Carbon Molecular Sieve Membranes

Although CMS membranes are subject to physical aging (*4*, *5*), performance of synthesized CMS membranes may be retained by: 1) exposure to active permeation of a feed gas (*4*, *6*); or 2) storage under moderate pressure (~100 psig) CO_2 (*7*). For the case of CO_2 storage, it is envisioned that the highly condensable CO_2 saturates the CMS microporous structure impeding relaxation of the porous aromatic structure. Moderate pressure CO_2 storage was used throughout this work, in order to minimize aging effects. Figure 5.7 summarizes results for untreated CMS membranes derived from 6FDA:BPDA-DAM(1:1) at 550 °C tested with a mixture of 50 mol% CO_2/50 mol% CH_4, stored under 100 psig of pure CO_2 between tests. After 30 days of storage, the CMS membranes show stable selectivity with ~10% drop in CO_2 permeance, referenced to initial performance. Extending storage time to a cumulative 90 days, the same membranes display stable selectivity and retain ~75% of the starting CO_2 permeance, showing that CO_2 storage can result in retention of a significant fraction of the attractive performance of CMS membranes, even over longer timeframes than previously investigated.

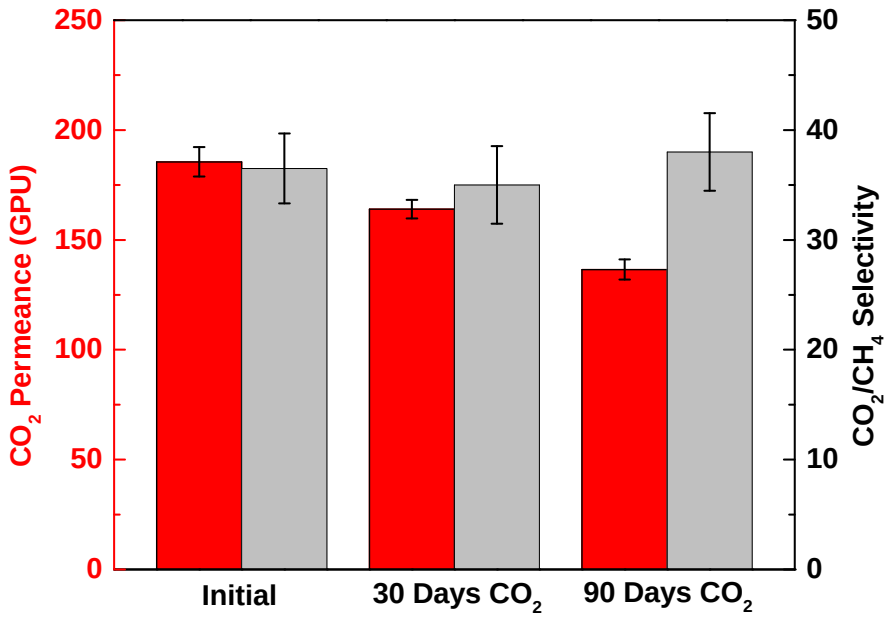

Figure 5.7. Performance of 6FDA:BPDA-DAM(1:1) derived CMS pyrolyzed at 550 °C under UHP argon after storage under 100 psig pure CO_2. Permeation results from 50 mol% CO_2/50 mol% CH_4 mixture gas tested at 50 psia and 35 °C.

However, it was noticed that after exposure to pure CO_2, amine doped CMS membranes lost CO_2/CH_4 selectivity while maintaining stable CO_2 permeance. These results are presented in Figure 5.8, where the open markers correspond to initial CO_2/CH_4 performance, and closed markers indicate permeation performance following exposure to CO_2.

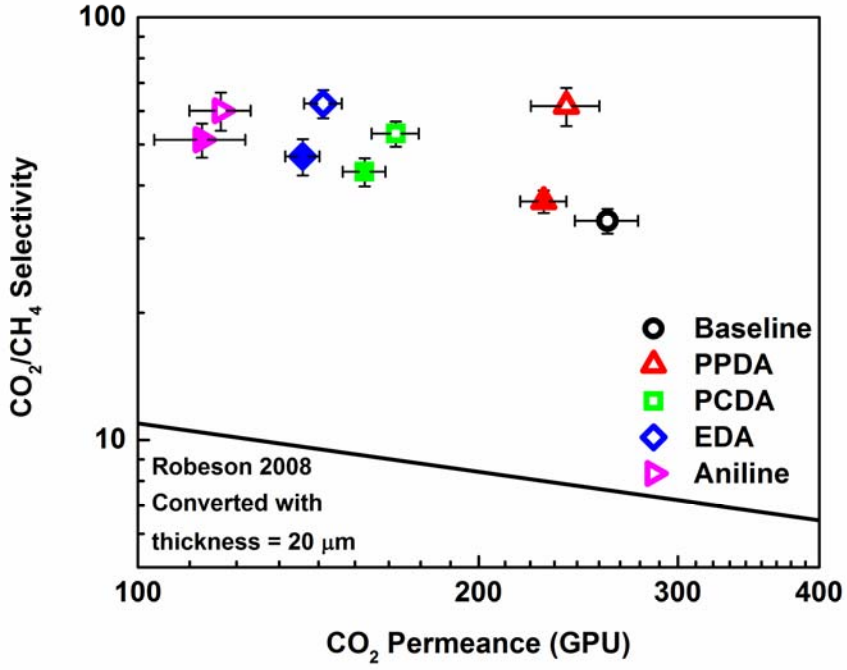

Figure 5.8. Performance degradation of amine treated CMS membranes. Open markers correspond to initial CO_2/CH_4 permeation results, closed markers correspond to permeation performance after exposure to pure CO_2. Pure gas measurements made at 50 psia and 35 °C.

Loss of CO_2/CH_4 selectivity with essentially constant CO_2 permeance is due to increased CH_4 permeance, suggesting that after exposure to CO_2 the amine doping modification is partially undone. While unexpected, this behavior may be attributed to interactions between the CO_2 and the amine dopants. As indicated previously, these dopants do not increase CO_2 affinity; nevertheless, interactions between CO_2 and amines have been widely studied for gas separations in both liquid absorption and solid adsorbents (*8–11*).

Considering amine doped CMS membranes investigated here, it is believed that trace amounts of moisture within the membrane resulting from atmospheric exposure

during module construction and testing procedures may combine with CO_2 forming carbonic acid. The presence of such acidic species may facilitate reversal of an amine-CMS bond resulting in a free amine that can bind a CO_2 molecule, forming either a carbamate or bicarbonate species depending upon conditions (*11*, *12*). While this hypothesis was not tested in this study, studies investigating exposure of a controlled %RH CO_2 feed versus a "bone dry" feed to amine doped CMS membranes is a direction for future work. Nevertheless, liberation of one end of a dopant could lead to increased mobility of the dopant within the CMS, thereby allowing the passage of gas penetrants through the larger less selective pathways that had once been blocked by the amine dopant bridge. Attempts to "regenerate" the current modules by heating, with hopes of removing the bound CO_2, were not feasible due to temperature limitations of the epoxy used in module construction. However, this would be an additional direction for future work.

Despite separation efficiency loss of amine treated CMS membranes after exposure to CO_2, subsequent permeation measurements indicates stable performance at the "degraded" state, summarized in Figure 5.9 below for a PCDA treated CMS membrane. The initially collected CO_2 and CH_4 pure gas permeation data resulted in a CO_2/CH_4 selectivity of 61 (cf. Figure 5.9 – Initial). After exposure to pure CO_2, retesting the membrane yields a "post CO_2 exposure" pure gas selectivity of 49 and a 50 mol% CO_2/50 mol% CH_4 mixture gas selectivity of 46. After 80 days storage under 100 psig CO_2, the same membrane displayed a CO_2/CH_4 mixture selectivity of 42 (cf. Figure 5.9 - 80 days CO_2 storage), showing that: 1) pressurized CO_2 storage can suppress physical aging of amine doped CMS membranes, similar to the case for untreated CMS; 2) further

performance degradation of amine doped CMS membranes is not seen after additional exposure to CO_2. Interestingly, the mono-amine (aniline) treated CMS display the smallest selectivity degradation, retaining 85% of initial CO_2/CH_4 selectivity. This could be due to a variety of factors, and would clearly benefit from additional work on mono-amine dopant performance.

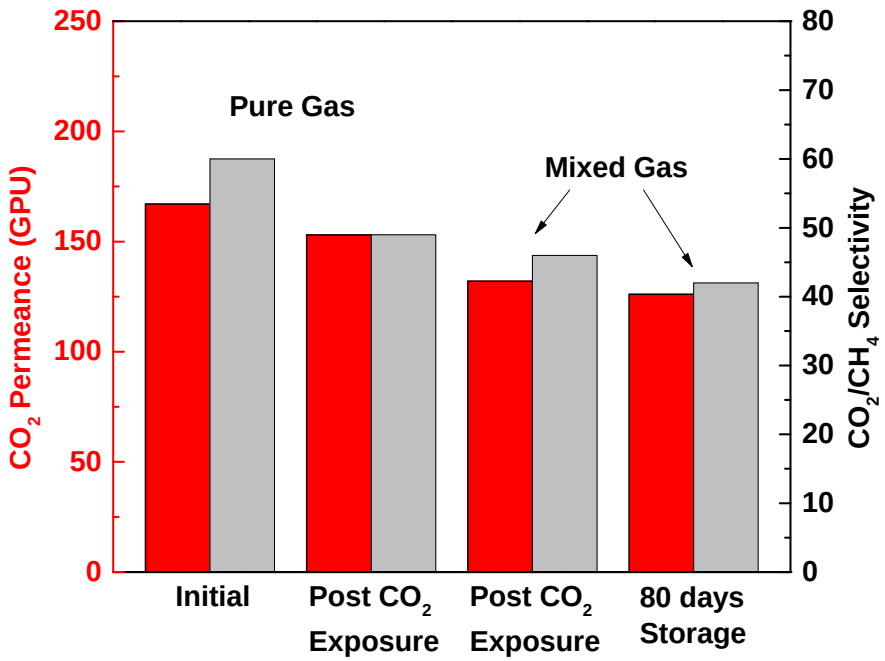

Figure 5.9. Long term testing of PCDA treated CMS membranes. Pure gas permeation performed at 50 psia and 35 °C. Mixed gas permeation of 50 mol% CO_2/ 50 mol% CH_4 at 50 psia feed pressure and 35 °C.

While performance degradation is seen for all amine treated CMS membranes after exposure to CO_2, the resulting materials still exhibit increased selectivity compared to baseline CMS (cf. Figure 5.8). Insight into the effects of amine dopants on the upper-

end of the ultramicropore distribution can be probed by permeation experiments of larger kinetic diameter gases, which will be considered next.

5.6 Impacts of Amine Dopant Structure on C_3H_6/C_3H_8 Separation Performance

Permeation experiments utilizing larger gas penetrants allows for probing the upper-end of the ultramicropore distribution of CMS materials, and the results of CMS structure modification techniques upon this regime. To investigated this regime, amine treated CMS membranes were exposed to an equimolar mixture of C_3H_6 and C_3H_8 (effective size of 3.82 Å and 3.95 Å, respectively) with results summarized in Figure 5.10, where the previously determined C_3H_6/C_3H_8 upper-bound relationship has been converted from Barrer to GPU using an average hollow fiber skin layer thickness of 20 μm, analogous to the CO_2/CH_4 cases studied previously (*13*).

It should be noted that the amine doped materials tested with the binary C_3 mixture gas had previously been exposed to CO_2 prior to permeation experiments, as the degradation behavior had not yet been discovered. However, the following analysis still holds in determining the effects of dopants upon the resulting performance for the C_3 separation on a qualitative basis.

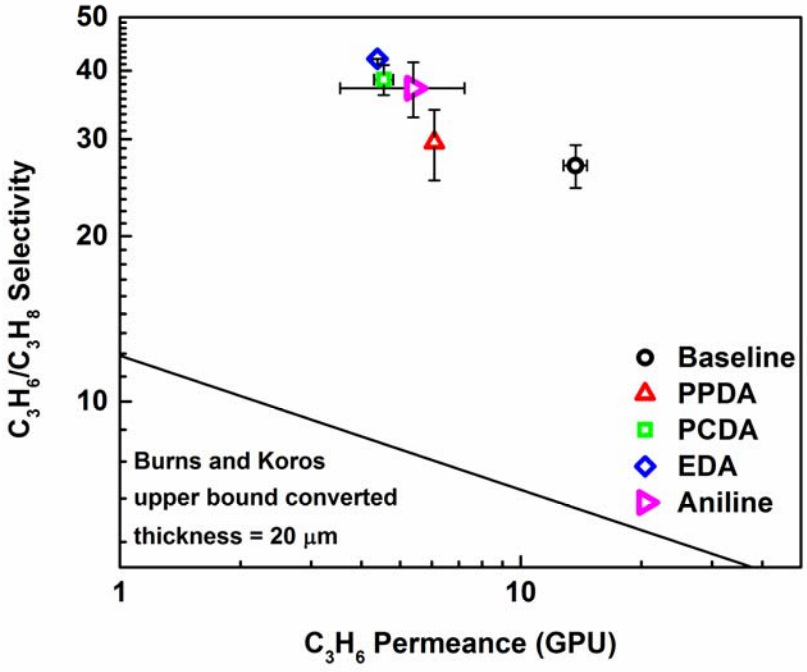

Figure 5.10. Mixed gas permeation results of CMS hollow fiber membranes treated with different amine dopants, tested with 50 mol% C_3H_6/50 mol% C_3H_8 at 50 psia and 35°C. Solid line represents the C_3H_6/C_3H_8 upper-bound transformed from Barrer to GPU using a 20 μm separation skin layer thickness (*13*).

From Figure 5.10 it is obvious that presence of amine dopants have a pronounced effect upon on CMS membranes for the C_3H_6/C_3H_8 separation, following a more intuitive structure-property trend compared to the CO_2/CH_4 separation in the previous section. It is clear that as the size of the amine dopant is decreased, a permeance reduction is coupled with increased selectivity. CMS membranes treated with the flexible EDA and PCDA show the lowest productivities and highest selectivities of the dopants investigated, presumably due to their ability to access smaller pore size populations than the rigid aniline and PPDA. While complementary gas sorption experiments of C_3H_6 and C_3H_8 on amine doped CMS materials were not performed, it is clearly a direction for future work.

Nevertheless, it is reasonable to assume the trends observed in CO_2 and CH_4 sorption on amine doped CMS would hold; introduction of amine dopants would decrease overall sorption capacity due to the presence of the amine dopants within a small population of micropores in CMS materials.

Considering the results for CO_2/CH_4 and C_3H_6/C_3H_8 performance of amine treated CMS membranes, initial insights into amine dopant structure-performance can be represented in Figure 5.11, where idealized bimodal pore size distributions for untreated and amine treated CMS membranes are presented. Introduction of a "large" amine dopant (e.g. PPDA) will result in modification of small micropores and large ultramicropores, causing a narrowing of both distributions. Decreasing the size of an amine dopant results in a shift of the modified pore size distribution, where further narrowing of the ultramicropore distribution is expected as pore accessibility of the dopant increases. But, based on the results in Figure 5.3, this shift seems to have small impacts on CO_2/CH_4 selectivity, indicating that only a small number of pores that are modified by this doping technique are leading to increased size and shape selectivity of the smaller CO_2 and CH_4 penetrants. This is not the case for the larger C_3 penetrants, which rely heavily on large ultramicropores for discrimination between compact bulky (i.e. C_3H_6) and more bulky (i.e. C_3H_8) penetrants. As shown in Figure 5.10, modification of pores within this regime may result in moderate permselectivity increases with permeance reductions from the tighter pore structure.

However, as dopant size decreases, the micropore distribution will broaden slightly – as smaller dopants may also tend to reside in large ultramicropores rather than small micropores, supported by experimentally collected sorption coefficients reported in

Table 5.3, where the largest dopant studied PPDA resulted in the lowest sorption coefficient for both CO_2 and CH_4. Further reduction in dopant size (e.g. EDA and aniline) or increased dopant flexibility (PCDA) leads to slight increases in sorption coefficients, or amount of gas that can be sorbed into the CMS micropores of the amine treated material, supporting the suggested shift in the pore size distribution reflected in Figure 5.11.

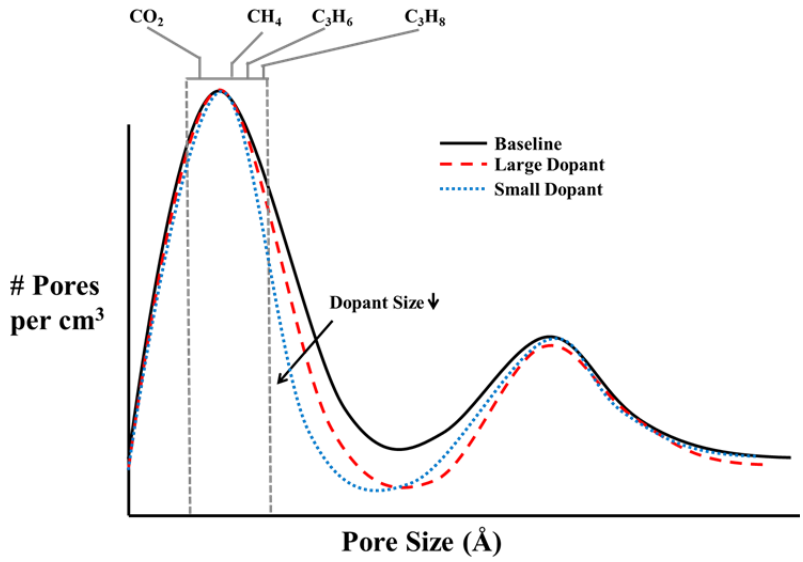

Figure 5.11. Idealized bimodal pore size distribution of untreated and amine treated CMS membranes. Dotted lines correspond to suggested pore size distribution sharpening as a result of amine dopant treatment.

5.7 Comparison between Reactive and Non-reactive Dopant Molecules

To this point, supported by NMR noted later, it is envisioned that amine dopants bind within the CMS structure, augmenting the separation properties by removing less selective pathways within the microporous structure. However, the role of the reactive amine group can be investigated further by comparison with a similarly sized,

nonreactive molecule such as *p*-xylene (cf. Table 5.1). To study this, CMS membranes were treated under identical conditions (i.e. 10 ppm in THF) with PPDA and *p*-xylene, for which the CO_2/CH_4 permeation performance are shown in Figure 5.12.

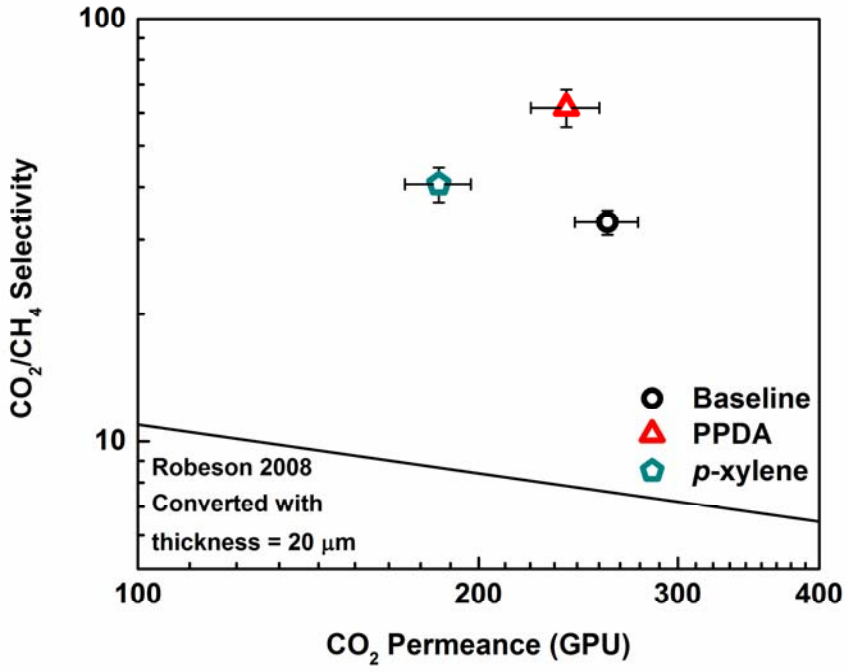

Figure 5.12. Pure gas CO_2 and CH_4 permeation results of CMS hollow fiber membranes treated with 10 ppm of PPDA and *p*-xylene dopants, tests performed at 50 psia and 35 ºC Solid line represents the 2008 CO_2/CH_4 Robeson upper-bound transformed from Barrer to GPU using a 20 μm separation skin layer thickness (*3*).

Comparing the performance of 10 ppm *p*-xylene treated CMS to baseline CMS, there is a significant reduction in CO_2 permeance from 260 to 180 GPU with a corresponding slight increase of selectivity from 33 to 40, which is significantly lower than PPDA treated CMS. The performance reduction may be due to *p*-xylene sorbing into the CMS micropores, removing available sorption sites for both penetrants causing a reduction in productivity without a significant rise in selectivity. While counterintuitive,

the selectivity difference can be explained by considering large ultramicropores and small micropores as distinct features, envisioned to be modified by amine doping. These regions can be described as morphologically distinct entities, where packing imperfections between the aromatic sheets can give rise small micropores, and large ultramicropores may be the result of poorly packed smaller aromatic strands that coalesce to form the aromatic sheets that pack into micropore cells. These packing imperfections may be associated with areas of increased residual oxygen and nitrogen content as a result of aromatization and fragmentation of the polymer precursor, even when formed under UHP Ar (see elemental analysis in Table B.1 in Appendix B). It is envisioned that the amine dopants will be attracted to these sites, leading towards functionalization of these disordered areas increasing selectivity of the treated material. Conversely, the chemically neutral *p*-xylene will not have increased attraction for these areas of disorder with chemical heterogeneity, and will reside in micropore galleries leading to decreased permeance and similar selectivity as the untreated baseline CMS.

It should be noted that unlike the amine treated CMS membranes, retesting pure gas permeation of the *p*-xylene treated CMS after exposure to CO_2 does not result in a performance drop, further supporting the hypothesis of CO_2 interacting with amines present from the doping process. Attempts of removing the *p*-xylene via exposure to unit activity (~140 psig) C_3H_6 for 24 hours, a treatment previously shown to "clean" CMS membranes exposed to organic materials (*2*), were unsuccessful with the membranes showing no significant change in performance, suggesting the *p*-xylene is trapped within the CMS structure. This result is surprising, and further investigation of exposing

p-xylene to CMS membranes for gas separations should clearly be addressed in future work.

Experimentally collected gas sorption isotherms of CO_2 and CH_4 on the 10 ppm *p*-xylene treated CMS materials are presented in Figure 5.13, along with isotherms for baseline CMS materials for reference. The associated Langmuir fit parameters and average sorption coefficients ($\mathbb{S}$) at 50 psia are summarized in Table 5.4. The results of the gas sorption measurements confirm the reduced capacity of both gases after introduction of the *p*-xylene to CMS membranes.

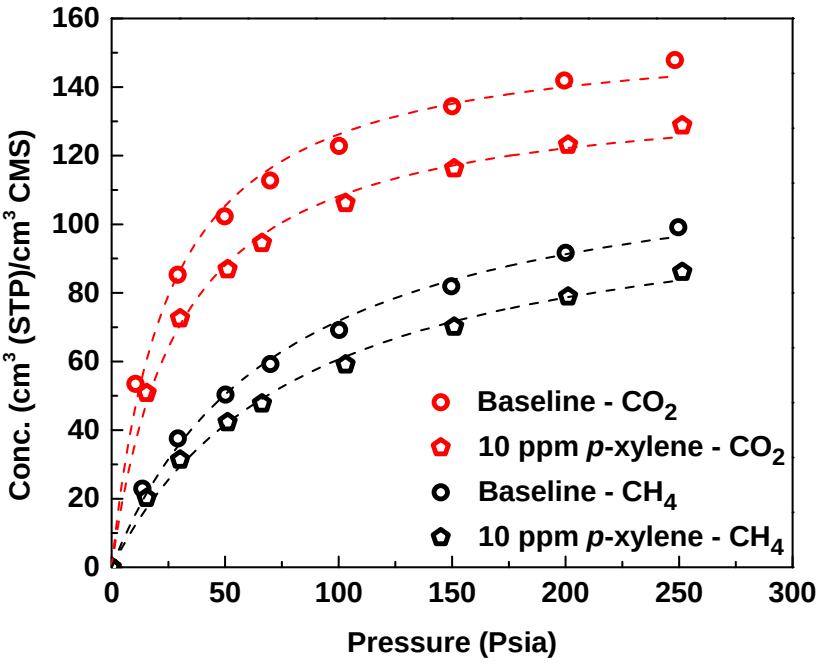

Figure 5.13. Gas sorption of CO_2 and CH_4 for baseline (untreated) and 10 ppm *p*-xylene treated CMS at 35 °C. Dashed lines represent Langmuir fit to experimentally collected data.

Table 5.4. Langmuir fit parameters for CO_2 and CH_4 gas sorption on untreated and *p*-xylene treated CMS membranes at 35 °C. Sorption coefficients for 50 psia and 35 °C.

Gas	Dopant	C_H' [cm^3 (STP)/ cm^3 CMS]	*b* [1/psia]	$\mathbb{S}$ [cm^3 (STP)/ (cm^3 CMS-psia)]
CO_2	**Baseline (0 ppm)**	157.35 ± 3.40	0.041 ± 0.004	2.11 ± 0.28
	10 ppm *p*-xylene	140.29 ± 3.24	0.034 ± 0.002	1.71 ± 0.33
CH_4	**Baseline (0 ppm)**	125.08 ± 4.13	0.013 ± 0.001	1.00 ± 0.13
	10 ppm *p*-xylene	111.92 ± 3.93	0.012 ± 0.001	0.87 ± 0.15

5.8 NMR Analysis to Determine Chemical Functionality of Amine Dopants in Carbon Molecular Sieve Membranes

In order to gain further insight into chemical states of the amine dopants within treated CMS materials, solid-state nuclear magnetic resonance (NMR) measurements of both ^{13}C and ^{15}N were performed. Due to the relatively low natural abundance of the ^{15}N isotope (*14*), ^{15}N-enriched amine dopants were used to improve responses in the collected NMR spectra. Two amine dopants, PPDA and aniline, were used within the NMR measurements in order to probe the differences in chemical species, as well as the role of a diamine to a single amine in the functionalization of CMS materials. As amine doping treatments for CMS membranes use relatively small (ppm) concentrations, NMR samples were synthesized under two different conditions: 1) 10 ppm of the desired amine dopant in THF, identical to that used to create membranes used for gas permeation experiments; 2) 5 wt% amine in THF was used to enhance incorporation of the isotopically labeled amines within the CMS materials in order to increase signal response.

5.8.1 ^{15}N-PPDA Treated Carbon Molecular Sieve Membranes

Both ^{13}C and ^{15}N CP MAS NMR spectra for CMS materials treated with ^{15}N-enriched PPDA amine dopant are shown in Figure 5.14 – (i) and (ii). Examination of the ^{13}C CP MAS spectra shows a large, broad peak centered at ~130 ppm for all samples investigated, indicative of the sp^2 carbons in the aromatic plates within the CMS material. It should be noted that the broad peaks centered at ~30 and ~225 ppm are spinning side bands (highlighted in gray and labeled "SSB"), artifacts of the MAS NMR technique that do not correspond to any chemical moieties within the materials. Further investigation of the spectra show additional small peaks in the amine treated samples at 66 and 160 ppm, corresponding to chemical shifts of sp^2 carbon-nitrogen and imine or amide carbonyl bonds, respectively. Peak assignments displayed in Figure 5.14 – (iii)-(v) correspond to representative configurations of amine dopants within CMS materials from the NMR results (*15*).

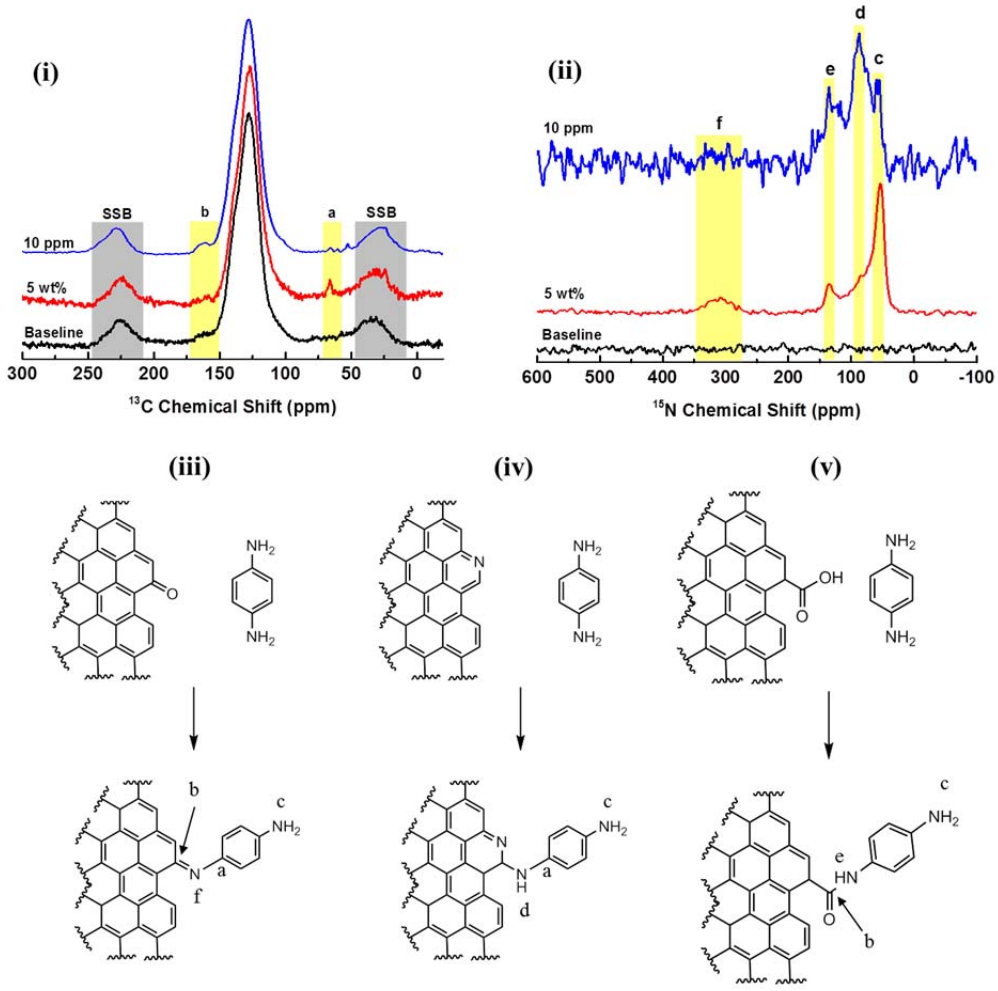

Figure 5.14. CP MAS NMR results for ^{15}N-PPDA treated CMS membranes, (i) ^{13}C spectra, (ii) ^{15}N spectra, (iii)-(v) are peak assigned adducts from possible reactions of the amine dopant with CMS material based off NMR results.

Inspection of the ^{15}N CP MAS NMR spectra for the baseline sample shows no response, due to the low natural abundance of ^{15}N; therefore, any chemical shifts displayed in the amine treated CMS spectra are *directly related to presence of the ^{15}N-labeled PPDA*. The chemical shift at 57 ppm corresponds to a primary amine, indicating that not all of the amines react within the CMS material due to either: 1) unreacted PPDA that is remaining within the CMS microstructure; 2) a pendant primary amine from a

PPDA within the CMS that could not reach an adjacent sheet or reactive group. The shift at 85 ppm corresponds to a secondary amine, possibly resulting of the pyridine substitution pathway (cf. Figure 5.14 – (iv)). The chemical shift at 135 ppm corresponds to a secondary amide moiety, which may be a result of reaction of the primary amine with carboxylic acid functionality shown in Figure 5.14 – (v). While this pathway was not originally hypothesized, it is possible for residual carboxylic acid moieties formed during imide ring degradation may be present due to the low pyrolysis temperature used here (550 °C).

Examining the 5 wt% treated spectrum it is clear that the intensity indicative of a primary amine at 58 ppm is greatly reduced suggesting a large portion of unreacted PPDA dopant was present within the CMS material under this treatment condition. Additionally, a chemical shift centered at 307 ppm corresponds to the proposed imine bond formed via the pathway outlined in Figure 5.14 – (iii). While this peak is not seen in the 10 ppm case, may still be present but at a level not measureable due to dilute concentration.

5.8.2 ^{15}N-Aniline Treated Carbon Molecular Sieve Membranes

In order to investigate the chemical differences between diamine and mono-amine dopants, analogous MAS NMR measurements were conducted utilizing ^{15}N-enriched aniline, where resulting ^{13}C and ^{15}N CP MAS NMR spectra are shown in Figure 5.15 - (i) and (ii) below. Similarly, proposed adducts from the reaction of aniline with the CMS materials are shown in Figure 5.15 – (iii)-(v).

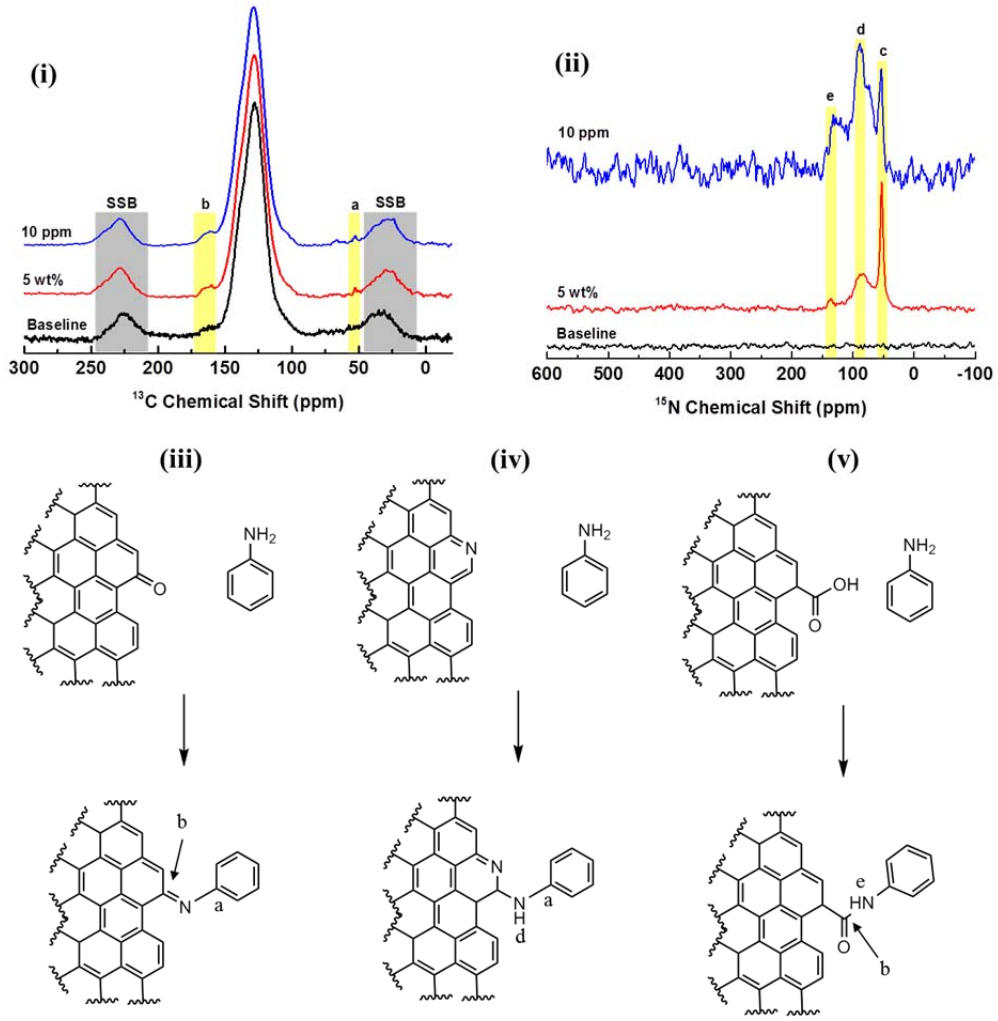

Figure 5.15. CP MAS NMR results for ^{15}N-aniline treated CMS membranes, (i) ^{13}C spectra, (ii) ^{15}N spectra, and (iii)-(v) are peak assigned adducts from possible reactions of the amine dopant with CMS material based off NMR results.

The ^{13}C CP MAS NMR spectra shown in Figure 5.15 – (i) for the aniline treated CMS materials is similar to that of the PPDA treated (cf. Figure 5.14 – (i)), where the spectra is dominated by the large broad peak at ~130 ppm corresponding to sp^2 carbons in the aromatic sheets. The new chemical shifts in the treated CMS at 52 and 160 ppm can be assigned to the sp^2 carbon – nitrogen bond in the aniline dopant and imine or amide bonds, respectively.

Examination of the ^{15}N spectra for the aniline treated CMS show identical peaks to that of the PPDA treated CMS membranes, suggesting similar adducts between the two amine dopants. However, in the case of the aniline, presence of the chemical shift at 53 ppm (primary amine) indicates that some amine dopant is present within the CMS structure without forming new covalent bonds, even at the lower 10 ppm concentration. The chemical shifts at 89 and 130 ppm can be identified as the same moieties as in the PPDA case, and have been identified in the proposed adducts presented in Figure 5.15 – (iii)-(v) (*15*).

These results show that there is not one unique chemical state of the amine dopants within treated CMS membranes. As there are a number of suggested reaction sites between CMS and amines, the variety of measured chemical states should not be surprising. Similar states were detected for both dopants investigated here, likely due to chemical similarities between the PPDA and aniline molecules. As was discussed in Chapter 4, these results suggest that amine doping is much more complex than originally envisioned and further studies will need to be conducted in order to elucidate the exact states present; however, the results shown in Figure 5.14 and Figure 5.15 suggest the presence of new chemical bonds supporting the initial hypothesis for amine doping as a new chemical modification of CMS materials.

5.9 Summary and Conclusions

This study extended the post-synthetic amine doping technique by examination of different, yet complementary amine dopant molecules to provide insight into resulting CMS membrane performance for gas separations. The general trend of smaller amine dopants resulting in lower productivity coupled with increased selectivity suggests

functionalization of smaller pores within the ultramicropore-micropore "cross-over" regime. However, as seen in the CO_2/CH_4 separation, the amine dopant size seems to have little effect upon selectivity; treatments with smaller amine dopants resulted in further permeance reductions with minimal selectivity enhancement. Meanwhile, testing larger C_3H_6/C_3H_8 penetrants showed a much stronger stable dependence of increasing selectivity with decreasing dopant size. These results suggest that, like oxygen doping of CMS membranes, different gas penetrants will exhibit different performance on modified CMS membranes, and that a condition ideal for one gas pair may not be attractive for another.

Instability of the amine doping technique was discovered after exposing treated CMS membranes to pure CO_2. This behavior is hypothesized to be a result of amine-CO_2 interactions causing breakage of bonds formed between dopants and the CMS. The degraded membranes exhibit lower CO_2/CH_4 selectivity than initially recorded, but still result in increased performance compared with untreated CMS membranes. Despite the reduction of initial separation efficiency, long-term storage of CMS membranes under 100 psig CO_2 allows for retention of separation performance. Investigation of stabilizing the amine-CMS bond via dopant selection, or regeneration of previously measured separation efficiency clearly needs to be addressed, and would be an interested avenue for continuation of this research.

Additionally, solid state NMR measurements of CMS membranes treated with amine dopants allowed for chemical evidence of new covalent bonds formed between amine dopant and CMS membranes, providing confirmation for the initially hypothesized reactions of dopants with CMS materials.

5.10 References

(1) Kiyono, M. Carbon Molecular Sieve Membranes For Natural Gas Separations, Georgia Institute of Technology, 2010. Ph.D. Thesis.

(2) Jones, C. W.; Koros, W. J. Carbon molecular sieve gas separation membranes-II. Regeneration following organic exposure. *Carbon* **1994**, *32*, 1427–1432.

(3) Robeson, L. M. The upper bound revisited. *J. Memb. Sci.* **2008**, *320*, 390–400.

(4) Xu, L.; Rungta, M.; Hessler, J. V.; Qiu, W.; Brayden, M.; Martinez, M.; Barbay, G.; Koros, W. J. Physical aging in carbon molecular sieve membranes. *Carbon* **2014**, *80*, 155–166.

(5) Ma, X.; Williams, S.; Wei, X.; Kniep, J.; Lin, Y. S. Propylene/Propane Mixture Separation Characteristics and Stability of Carbon Molecular Sieve Membranes. *Ind. Eng. Chem. Res.* **2015**, *54*, 9824–9831.

(6) Wenz, G. B.; Koros, W. J. Tuning Carbon Molecular Sieves for Natural Gas Separations: A Diamine Approach. *AIChE J.* **2017**, *63*, 751–760.

(7) Bhuwania, N. Engineering The Morphology of Carbon Molecular Sieve (CMS) Hollow Fiber Membranes, Georgia Instititue of Technology, 2014. Ph.D. Thesis.

(8) Blauwhoff, P. M. M.; Versteeg, G. F.; Van Swaaij, W. P. M. A Study on the Reaction Between CO2 and Alkanolamines in Aqueous Solutions. *Chem. Eng. Sci.* **1983**, *38*, 1411–1429.

(9) Vaidya, P. D.; Kenig, E. Y. CO2-alkanolamine reaction kinetics: A review of recent studies. *Chem. Eng. Technol.* **2007**, *30*, 1467–1474.

(10) Sumida, K.; Rogow, D. L.; Mason, J. A.; McDonald, T. M.; Bloch, E. D.; Herm, Z. R.; Bae, T. H.; Long, J. R. Carbon dioxide capture in metal-organic frameworks. *Chem. Rev.* **2012**, *112*, 724–781.

(11) Bollini, P.; Didas, S. A.; Jones, C. W. Amine-oxide hybrid materials for acid gas separations. *J. Mater. Chem.* **2011**, *21*, 15100–15120.

(12) Didas, S. A.; Sakwa-Novak, M. A.; Foo, G. S.; Sievers, C.; Jones, C. W. Effect of amine surface coverage on the Co-adsorption of CO2 and water: Spectral deconvolution of adsorbed species. *J. Phys. Chem. Lett.* **2014**, *5*, 4194–4200.

(13) Burns, R. L.; Koros, W. J. Defining the challenges for C3H6/C3H8 separation using polymeric membranes. *J. Memb. Sci.* **2003**, *211*, 299–309.

(14) Coplen, T. B.; Bohlke, J. K.; De Bievre, P.; Ding, T.; Holden, N. E.; Hopple, J. a.; Krouse, H. R.; Lamberty, A.; Peiser, H. S.; Revesz, K.; Rieder, S. E.; Rosman, K. J. R.; Roth, E.; Taylor, P. D. P.; Vocke, R. D.; Xiao, Y. K. Isotope-abundance variations of selected elements (IUPAC Technical Report). *Pure Appl. Chem.* **2002**, *74*, 1987–2017.

(15) Thorn, K. A.; Pettigrew, P. J.; Goldenberg, W. S.; Weber, E. J. Covalent Binding of Aniline to Humic Substances. 2. 15 N NMR Studies of Nucleophilic Addition Reactions. *Environ. Sci. Technol.* **1996**, *30*, 2764–2775.

CHAPTER 6. CARBON MOLECULAR SIEVE STRUCTURE AND MEMBRANE PERFORMANCE RELATIONSHIPS

Parts of this chapter are reproduced from "Rungta, M.; Wenz, G.B.; Zhang, C.; Xu, L.; Qiu, W.; Adams, J.S.; Koros, W.J., Carbon Molecular Sieve Structure Development and Membrane Relationships. *Carbon,* **2017**, *115*, 237-248.

6.1 Overview

This chapter seeks to extend the fundamental understanding of the structure of carbon molecular sieve (CMS) membranes, and provide an initial step in connecting the transformation of the random coil polyimide into ultra-rigid CMS materials with exquisite size and shape selectivity. A majority of the data reported within this work has been previously reported (*1–3*); however, the resulting analysis and hypotheses regarding the evolution of the CMS structure comprise the unique contribution of this work.

This chapter starts with a review of the currently accepted representation of CMS materials, and the shortcomings of traditional characterization techniques when applied to CMS materials. A hypothetical evolution pathway from the random coil polyimide precursor to the ultra-rigid CMS material is proposed, after which transport data resulting from molecular scale gas probe analysis is discussed in a self-consistent manner with respect to the proposed pathway. Lastly, additional CMS pore size tuning tools are discussed in terms of the new vision of the CMS evolution pathway, and how they may be used to create next generation membranes for challenging gas separations.

6.2 Current Carbon Molecular Sieve Structure and Characterization Limits

It is generally accepted that CMS transport properties rely upon a slit-like pore structure consisting of a distribution of larger (~ 7-20 Å) micropores connected by smaller (< 7 Å) ultramicropore windows (*4–7*). This fact notwithstanding, understanding the evolution of precursor semi-flexible polymers into final CMS structures is at an early stage. Figure 6.1-(i & ii) represent the CMS pore structure and bimodal distribution comprising micropores and ultramicropores. Figure 6.2 is a popular representation of a CMS material derived from a hydrocarbon precursor but it also provides a starting point for discussion of more complex CMS materials derived from polyimide precursors in this work, such as shown in Figure 6.3.

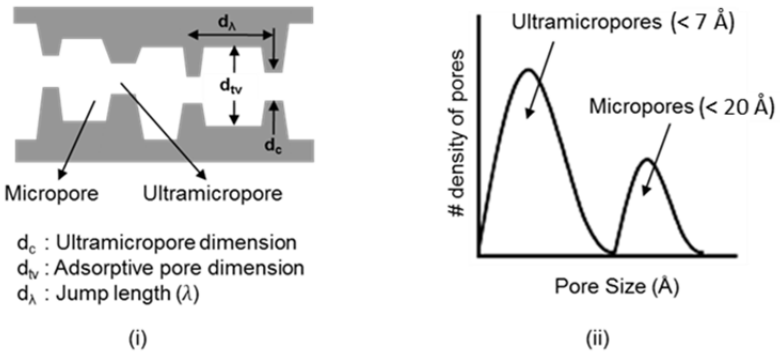

Figure 6.1. CMS (i) Idealized "slit-like" pore structure and (ii) Bimodal distribution of pores (*8*).

Figure 6.2. Turbostratic carbon structure believed to represent some CMS materials (6).

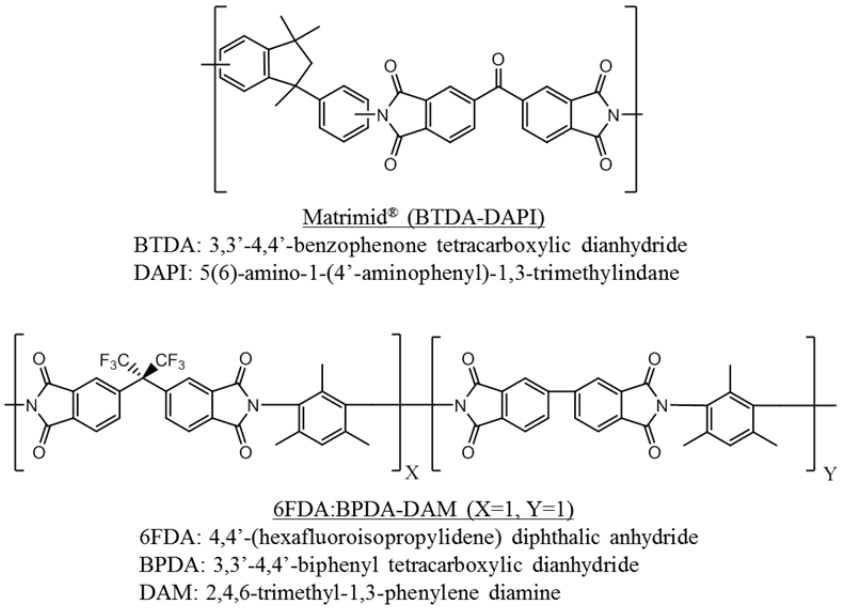

Figure 6.3. Chemical structure of semi-flexible precursor polyimides Matrimid® and 6FDA:BPDA-DAM(1:1).

Making a connection between the representations of the bimodal distribution of pores in Figure 6.1 and a more chemically-relevant structure such as that in Figure 6.2 is desirable—but challenging. It is reasonable to connect these two representations by attributing ultramicropores to defects *within the plates* shown in Figure 6.2, while attributing the micropores to the spaces *between the plates*. Of course, the details of the plate structure in such a picture will be different in a simpler hydrocarbon versus a

polyimide derived CMS. Unlike oxygen-containing cellulosic and purely hydrocarbon precursors, the presence of fluorine and nitrogen in the polymer backbone introduces additional factors affecting the ultimate properties of the final CMS versus the case in Figure 6.2. Moreover, differences will exist even between CMS derived from different precursor polyimides (*8–10*); however, the general concepts and features should be similar, as is considered later in this discussion.

Previous work on CMS materials derived from Matrimid® and similar aromatic polyimide precursors noted the difficulties in using traditional characterization techniques, due to the amorphous nature of these materials (*11–15*). Recent work on more complex 6FDA-based polyimide precursors further highlighted the disconnect between precursor physical properties and the resulting CMS materials. This recent work documented the lack of direct physical connection between free volume and x-ray "d-spacings" of polymer precursors and corresponding properties of CMS (*16*). Considering these previous discussions, it is evident that this lack of a simple connection between the random coil precursor and the generally accepted slit-like structure of the final CMS, reminiscent to Figure 6.1, needs to be addressed (*4*, *8*). Establishing such a connection is critical to the advancement of the fundamental understanding of CMS materials. The current work aims to establish this important connection by discussing similarities and differences that arise from Matrimid® and 6FDA:BDPA-DAM derived CMS materials.

6.3 Evolution of the Carbon Molecular Sieve Structure

Although CMS materials formed from various polyimide precursors will exhibit differences in final structure and performance, the general features and concepts presented here should be relevant to all such precursors. For the specific case of the

6FDA:BPDA-DAM precursor of interest here, we will focus on the evolution from the random coil precursor during transformation into a disrupted plate structure with slit-like ultramicropores related to Figure 6.2 in a typical pyrolysis protocol. Such a general protocol, noted in the Chapter 3, is represented in Figure 6.4 with three distinct periods: ramp, soak, and cool. During these periods, the random polymer coil (Figure 6.5-(i)) is transformed to a dramatically different CMS material. Elemental analysis of the CMS and consideration of evolved gases during the "ramp" phase of pyrolysis under UHP argon indicate that CF_3H, HF as well as CO_2, CO and H_2 are important components leaving during pyrolysis of such a precursor (*17*). During the temperature ramping process, further aromatization occurs, with considerable nitrogen maintained in the carbon until rather high temperatures (Appendix B), consistent with other studies (*18–22*). On the other hand, CO and CO_2 evolution occurs even at relatively low temperatures to remove most, but not all, of the originally present oxygen atoms. For the precursor in Figure 6.3, considering pathways consistent with the loss of the components mentioned above leads to a possible rigid, highly aromatic strand represented in Figure 6.5-(ii), which will be used in discussion of the CMS formation. Details of the suggested strand structure are not crucial for high level considerations that are the main interest here, and this representative example strand will be discussed later.

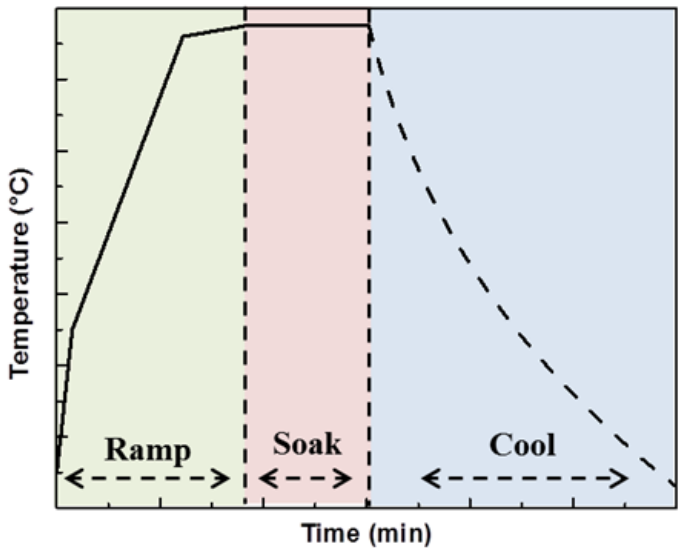

Figure 6.4.Typical time versus temperature profile used for CMS formation in this study.

Pyrolysis of a typical ~150,000 g/mol semi-flexible random coil polyimide, which loses only ~40% of its weight upon pyrolysis, to produce a high molecular weight rigid structure presents a *solid state packing problem*. A similar problem is encountered in transforming a high molecular weight cellulosic precursor to the type of structure in Figure 6.2 or Figure 6.5-(vi). In either case, the entangled semi-flexible precursor undergoing aromatization and extreme linearization will tend to experience sufficient localized stresses to cause periodic scissions along its backbone, illustrated in Figure 6.5-(i), (ii). Such backbone scissions are envisioned to occur during the temperature ramp to the final pyrolysis temperature (cf. Figure 6.4 – "ramp") allowing aromatization to proceed while producing shorter, more mobile structural strands; however, *a packing issue still exists* for such rigid strand oligomers.

It is envisioned that the rigid strands "solve the packing problem" in the way a rigid liquid crystalline polymer responds to the presence of high concentrations of rigid

strands—by organizing into more packable entities such as plates (*23*). Polymeric materials that exhibit liquid crystallinity are comparatively rigid, resulting in extension along the backbone – similar to that of the aromatic structural strands that are envisioned within the CMS materials. Envisioning these strands as simple hard body, rod-like structures whose only interactions are large repulsions due to direct overlap allows for a simpler explanation. While intermolecular attractive forces may contribute to increase stabilization, they are neglected for the sake of simplicity here.

While counterintuitive, the aligned plates comprised of strands (Figure 6.5-(iii)) are in an overall higher entropy state. According to statistical thermodynamics, the entropy (*S*) of a system is the measure of the different possible microstates accessible within a system, can be represented by:

$$S = k_B \ln(Z) \tag{6.1}$$

where k_B and Z are the Boltzmann constant and system partition function or measure of possible arrangements, respectively. The system partition function, Z, can be rewritten as:

$$Z = Z_{comb} * Z_{orient} \tag{6.2}$$

where Z_{comb} is the combinatorial partition function, measuring the number of accessible non-overlapping configurations for the system of rod particles. Z_{orient} is the measure of rods with disorientation from the preferred axis of alignment within the system. Z_{comb} and Z_{orient} are competing factors; Z_{comb} decreases with increasing disorder of rods whereas Z_{orient} increases, indicating phase stability occurs at some intermediate value. When high concentrations of rod particles with sufficient mobility are present, realignment towards a

common (parallel) axis is driven by the reduction of excluded volume between adjacent rods (*23*). While the reorientation results in a reduction in the Z_{orient} due to the smaller fraction of rods not aligned, it is coupled with an even larger increase in Z_{comb} as alignment in a high concentration of rods results in a drastic increase in the possible states (Z), or packing, resulting in an overall increase in the system entropy, S.

Based on the above analysis, it can be envisioned that alignment of the strands during the temperature ramp phase of the pyrolysis is preferred as it reduces the excluded volume present within a "random" phase packing of strands (Figure 6.5-(ii)), allowing for an increased number of possible packing states of lateral entities. Some lateral linkages due to consolidation of lateral strands may occur, evolving molecular H_2 in the process. Nevertheless, an amorphous nature results, since kinetic restrictions hinder perfect organization within the plates themselves and with imperfect long range stacking of plates during the limited time at high temperature during the "soak" phase in Figure 6.4, when mobility is high. A typical idealized micropore "cell" with imperfectly packed sides comprised of imperfectly organized strands, reminiscent of Figure 6.2, is illustrated in Figure 6.5-(iv). Ongoing evolution to the many neighboring cells in the idealized CMS structure is envisioned to occur during the final thermal soak and cooling after pyrolysis, as illustrated in Figure 6.5-(iv) through (vi). During the soak and cooling phases (cf. Figure 6.4), adjacent micropore "cells" (Figure 6.5-(iv)) will coalesce, wherein ultramicropore "walls" will be shared between "cells", resulting in a cellular structure envisioned to have a form similar to Figure 6.5-(vi), where the front ultramicropore "walls" have been removed to highlight the resulting structure. The amorphous CMS, with micropores separated by ultramicropores in the micropore plate

walls will, however, have molecular sieving properties. The hypothetical evolution path and structures illustrated in Figure 6.5 is useful not only to envision the formation of the polyimide-derived CMS, but also to understand how controlling pyrolysis atmosphere and post-processing of CMS materials affect resulting membrane performance.

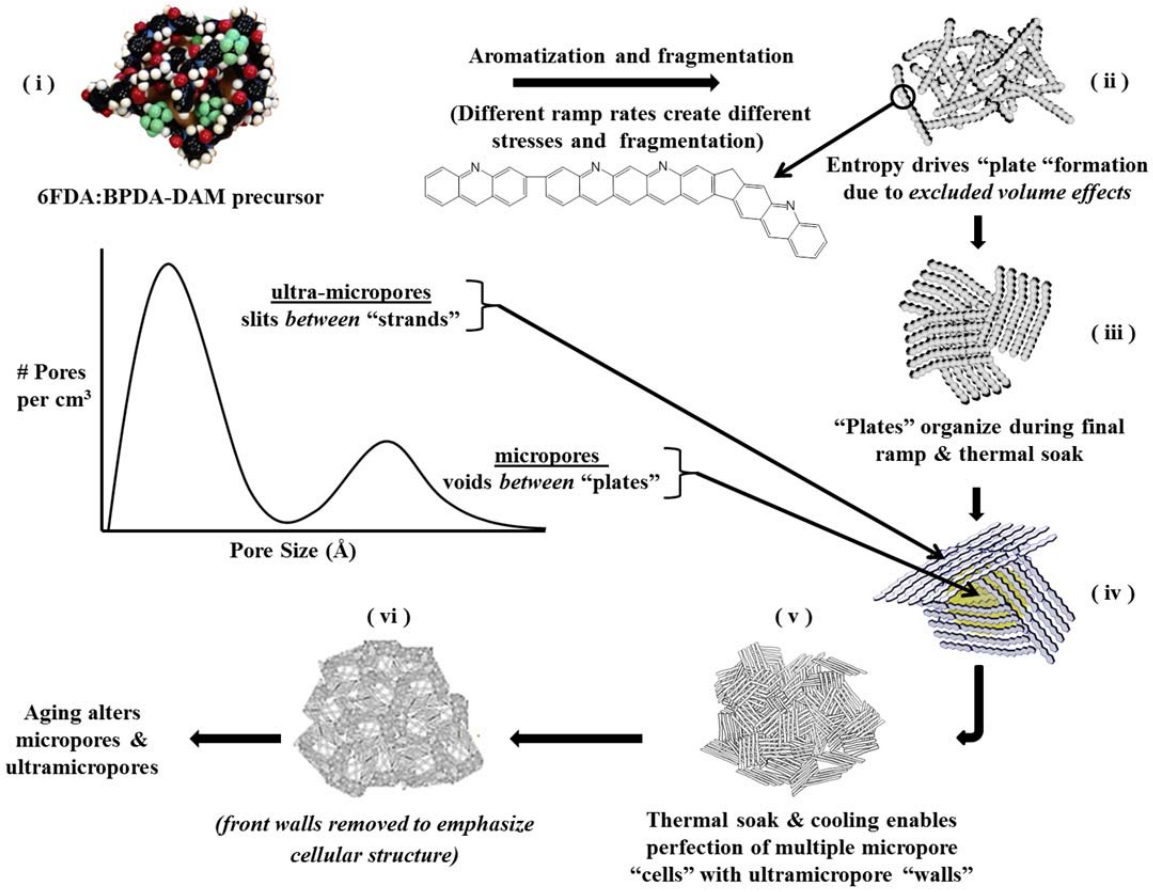

Figure 6.5. Envisioned initial steps in transformation from random coil precursor polyimide to organized amorphous CMS material with bimodal distribution of micropores with ultramicropores.

Post-synthesis, CMS materials are subject to a physical aging phenomenon, where partial densification of the imperfectly stacked plates may occur, with reduction in the average distance between the plates, i.e. the *micropore size* or the molecular jump length

(λ in Figure 6.6) (*3*, *24*, *25*). Such minor changes in organization of the aromatic strands *within the various plates* result in minor diffusion selectivity changes associated with the slits (d_{um} in Figure 6.6) *between* the imperfectly organized strands, but with significant reductions in diffusion and sorption coefficients (*24*). The conceptual model presented in Figure 6.5 and Figure 6.6 helps clarify how processing and structure can be related to resultant membrane performance in a consistent manner.

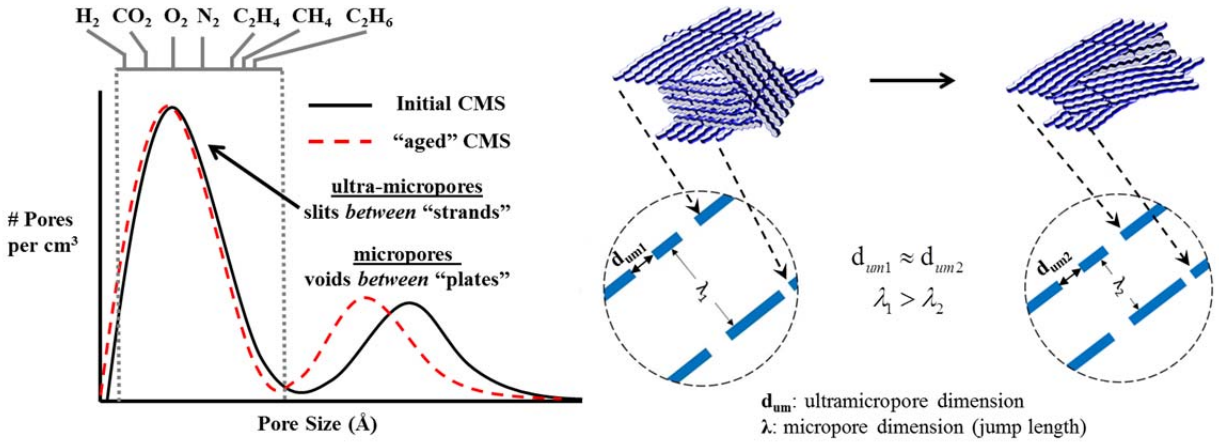

Figure 6.6. Aging or annealing of CMS structure results in micropore settling with only minor ultramicropore slit tightening.

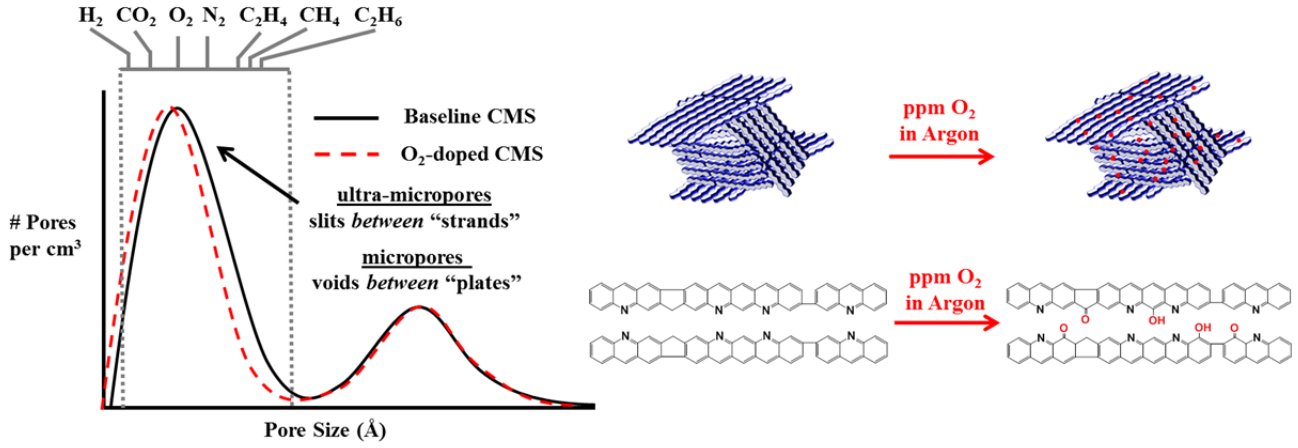

Figure 6.7. Oxygen doping of CMS structure results in tightening of size-selective ultramicropores with no changes in micropore distribution.

During CMS formation, addition of parts per million of molecular oxygen into the pyrolysis atmosphere leads to selective functionalization of the edges of the imperfectly organized strands, illustrated by the idealized aromatic structure in Figure 6.5-(ii) (*2*, *26*). This doping can selectively narrow accessible points, and tighten the ultramicropore distribution as shown in Figure 6.7, resulting in an increase in membrane selectivity with a moderate reduction in productivity. Oxygen doping has been shown to only modify the size selective ultramicropores in Matrimid® derived CMS materials, *not the micropores believed to be responsible for sorption.* (*27*). Another study demonstrated that for different 6FDA-based polyimide precursors the same effect applies, and presumably is general to all CMS materials (*28*). While determination of the exact state of the oxygen is outside the scope of this current discussion, spectroscopic evidence of carbonyls has been previously reported (*2*); however one can envision a multitude of oxygen chemisorption pathways during the complex pyrolysis process. In fact, as noted later, CMS formed under UHP Argon contains residual oxygen (Table B.1 in Appendix B), which may be present in various states. For example, oxygen resulting in an alcohol functionality, whether remaining from precursor materials or due to oxygen doping, may undergo tautomerization to the previously observed carbonyl form (*29*, *30*). Detailed identification of the array of oxygen functionalities in the CMS materials will clearly benefit from additional work in the future.

Finally, Figures 6.5, 6.6, and 6.7 also provide a framework to discuss changes in precursor structure and the impact on CMS separation properties. The biphenyl link in the BPDA unit in Figure 6.3 provides a potential weak point in the precursor backbone, which actually offers a tool to control strand structure. Increasing the 6FDA:BPDA

monomer ratio from (1:1) to (2:1) may impact the complex process of aromatization, fragmentation and organization envisioned in Figure 6.5, along with and the ultimate CMS properties. The above conceptual framework will be used to discuss such issues in a self-consistent manner in the following sections.

6.4 Impacts of Precursor Structure

6.4.1 Sorption Isotherms and Pore Distribution Analysis from CO_2 Sorption

Gas sorption measurements for the extensive array of gases in Table 6.1 were carried out on CMS derived from 6FDA:BPDA-DAM at 675 °C. Sorption isotherms for 6FDA:BPDA-DAM at 35 °C are shown along with earlier reported results for Matrimid® derived CMS in Figure 6.8 (*11*).

Table 6.1. Gases used for sorption and permeation measurements utilized in the "molecular" ruler methodology employed in this work.

Size (σ) and critical temperature (T_c) for common gases (H_2, CO_2, O_2, N_2, CH_4) adopted from (*31*), noble gases (He, Ne, Ar, Kr, Xe) from (*32*, *33*), for SF_6 from (*31*, *32*), with size of C_2H_4 and C_2H_6 defined based on slit-like pores using space-filling CPK models and calibrated "slits" (*11*, *34*)**.**													
Gas	He	Ne	H_2	CO_2	O_2	Ar	N_2	Kr	C_2H_4	CH_4	C_2H_6	Xe	SF_6
σ (Å)	2.6	2.8	2.89	3.3	3.46	3.5	3.64	3.7	3.75	3.8	3.85	4.1	5.5
T_c (K)	5.3	44.5	33.2	304	155	151	126	209	283	191	306	290	319

As described earlier in Chapter 2, gas molecules sorb into micropore sites of the CMS and transport through the membrane by making diffusive jumps from one sorption site to the next through size selective ultramicropore slits. Gas sorption generally increases with condensability (e.g. critical temperature, T_c) but may also be augmented by other factors like dipoles and quadrupoles (*35*). Since micropore sorption sites

communicate by narrower ultramicropore windows, exclusion of the larger penetrant in a gas pair can occur; however, the distribution of ultramicropore sizes makes complete exclusion unlikely. As expected, sorption isotherms in Figure 6.8 show a general trend of increasing sorption uptake with increasing penetrant critical temperature (Table 6.1). Helium can sample most of the pores, but its sorption uptake is very small owing to its low critical temperature. On the other hand, SF_6 with a high critical temperature and condensability shows low sorption uptake, presumably due to substantial molecular sieving because of its large size. For all gases, higher sorption is seen in 6FDA:BPDA-DAM derived CMS, compared to the corresponding Matrimid® derived CMS reported earlier at 675 °C, reflecting larger 6FDA:BPDA-DAM CMS micropore volume compared to Matrimid® (*11*).

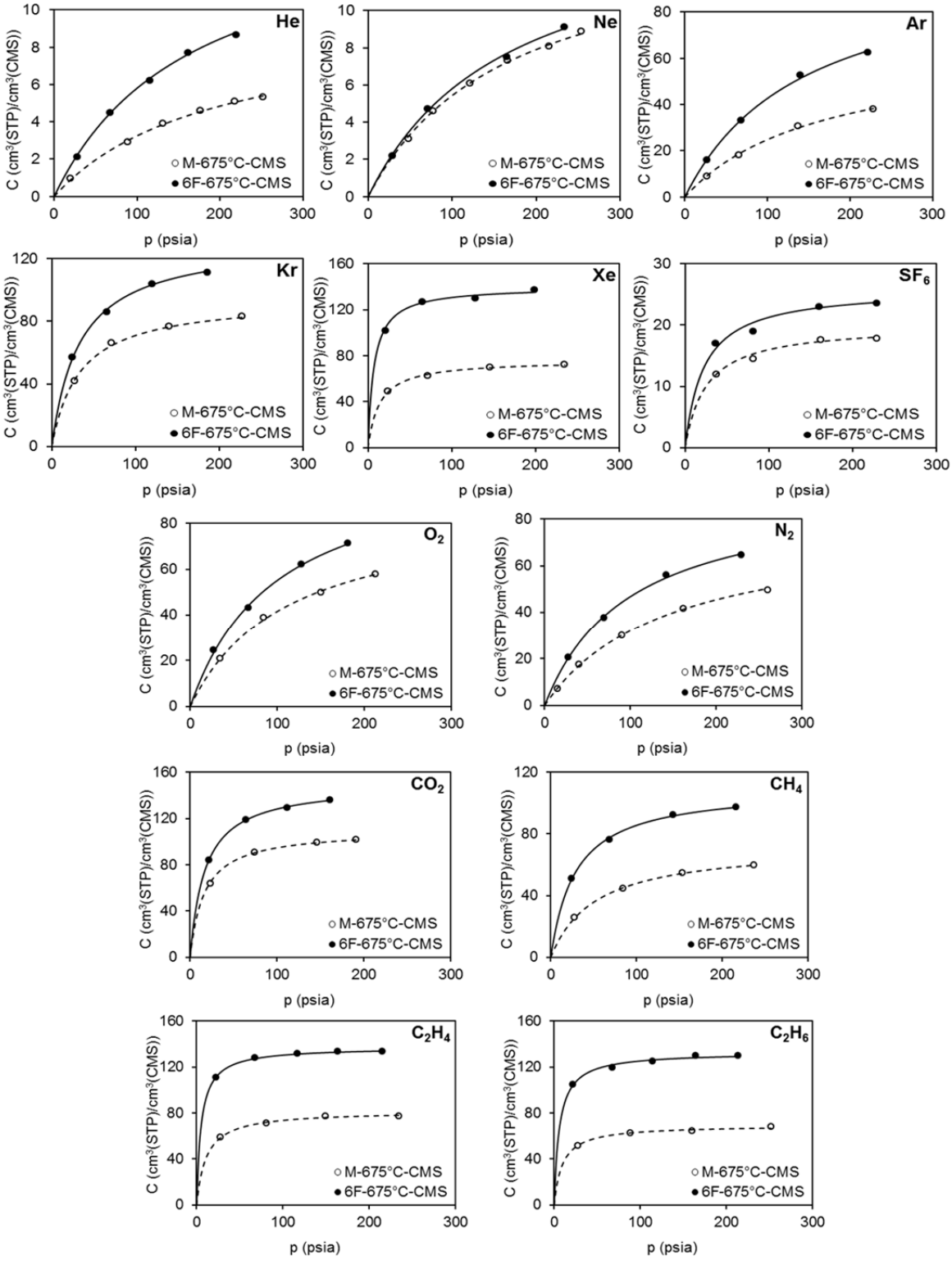

Figure 6.8. Sorption isotherms of different gases for CMS derived from UHP Ar pyrolysis of Matrimid® and 6FDA:BPDA-DAM at 675 °C. Reproduced from (*1*).

.

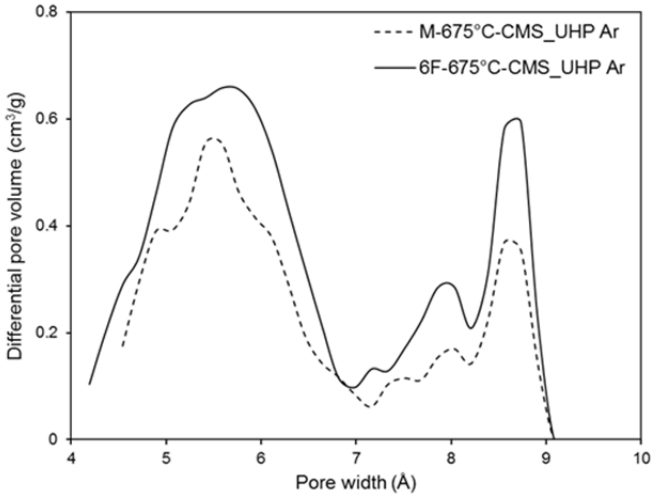

Figure 6.9. Pore size distribution from CO_2 uptakes for CMS derived from UHP Ar pyrolysis of Matrimid® (- - -) and 6FDA:BPDA-DAM (––) at 675 °C. Data generated by Micromeritics for samples supplied from (*1*). Details in (*8*).

A similar trend was also reported by Kiyono et al. for CMS derived from Matrimid® and 6FDA:BPDA-DAM pyrolysis at 550 °C (*2*). A pore size distribution (Figure 6.9), obtained from analysis of CO_2 uptake measurements at 0 °C, complement the above conventional sorption findings (*8*). Consistent with trends observed in in the sorption data for the wide range of gases in Figure 6.8, the 6FDA:BPDA-DAM CMS has a larger overall micropore volume compared to Matrimid® CMS reported earlier (*8*). The higher sorption uptakes of the 6FDA:BPDA-DAM derived CMS compared to the Matrimid® derived CMS reflect higher saturation capacities, consistent with larger micropore volume when compared to Matrimid® noted in Figure 6.9 and reported in Table 6.2. The increased micropore volume is due to presence of the bulky $–CF_3$ groups in the 6FDA unit of the 6FDA:BPDA-DAM precursor, which are evolved during the pyrolysis process as HF and HCF_3, disrupting polymer chain packing. Loss of these bulky fluorinated

groups leads to a more open CMS structure with higher porosity when compared to Matrimid® which lacks any bulky fluorinated groups, and is reflected in the measurements above. Although useful for characterizing micropores, small ultramicropores with sizes < 4 Å cannot be probed via CO_2 or N_2 sorption pore characterizations.

Table 6.2. Pore volume of CMS materials derived Matrimid® and 6FDA:BPDA-DAM(1:1) from CO_2 uptake measurements at 0 ^{0}C.

	Volume in pores ≤10.8 Å (cm^3/g)	**Volume in ultramicropores ≤7 Å (cm^3/g)**
M-675°C-CMS_UHP Ar	0.1072	0.0835
6F-675°C-CMS_UHP Ar	0.1600	0.1184

6.4.2 Gas Diffusion as Ultramicropore Probes

Permeability of the penetrant gases listed in Table 6.1 for CMS derived from the pyrolysis of Matrimid® and 6FDA:BPDA-DAM at 675 °C are reported in Figure 6.10. Permeability trends cannot be conclusively understood using pore size distributions obtained from sorption measurements; however diffusivity trends allow investigation of ultramicropore dimensions responsible for molecular sieving. The strong dependence of diffusivity upon molecular size is the basis for an effective "molecular ruler" to characterize the amorphous CMS materials, complementing traditional characterization methods (11). Examining diffusion coefficients and diffusion selectivities for various penetrant gas pairs can provide insight into CMS materials not captured in permeability and sorption measurements. Corresponding sorption and average transport diffusion coefficients (determined from $P/\overline{\mathbb{S}}_A$) are reported in supplemental Figures B.1 and B.2 in Appendix B, respectively.

For all gases, the 6FDA:BPDA-DAM-derived CMS shows higher permeabilities than Matrimid® derived CMS. The higher permeabilities and free volume of the 6FDA:BPDA-DAM versus Matrimid® polymer precursor correlates with higher permeabilities in the final CMS; however, as shown by Fu et. al. (*16*), such a correlation is not always seen. Given the complex events during the CMS formation, this lack of a simple correlation should not be surprising.

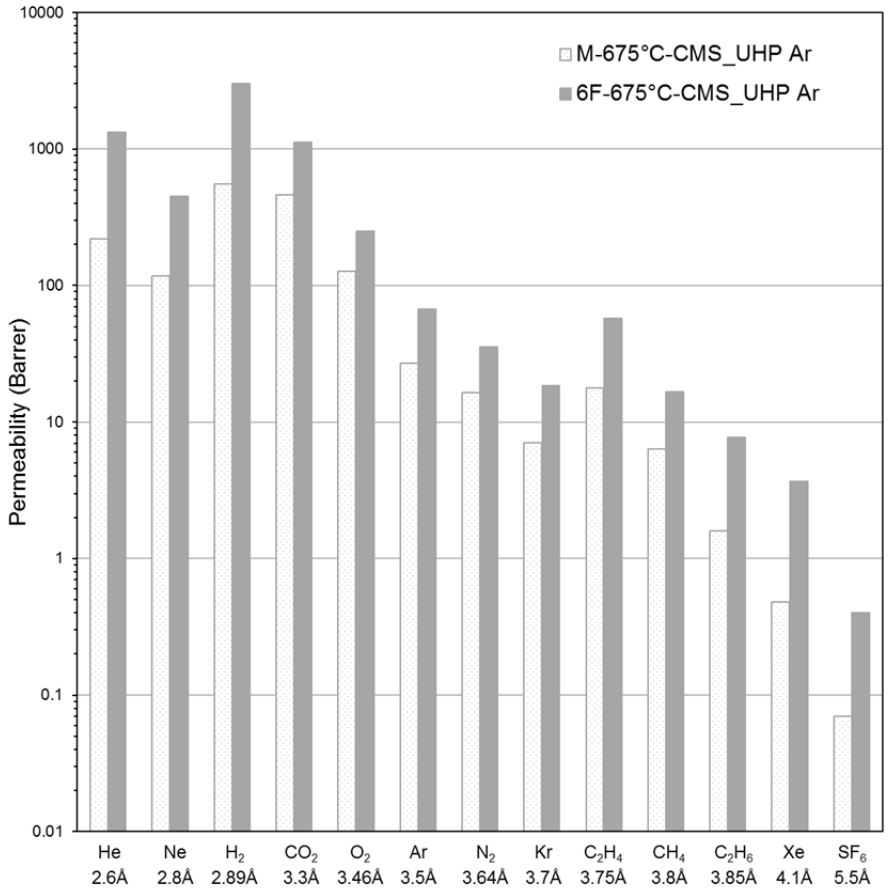

Figure 6.10. Permeabilities of different gases for CMS derived from Matrimid® and 6FDA:BPDA-DAM at 675 ^{0}C under UHP Argon. Permeability measurements were made at 35 °C using 50 psia feed pressure. Reproduced from (*1*).

While permeability and sorption coefficients have practical utility; the special capability of CMS to execute penetrant size and shape selectivity is seen best by extracting and analyzing diffusion coefficients from permeability and solubility coefficients. The more meaningful thermodynamically corrected diffusivities in CMS derived from 6FDA:BPDA-DAM are shown in Figure 6.11, along with values for previously studied Matrimid® derived CMS created at 675 ^{0}C under UHP Argon (*11*). These thermodynamically corrected coefficients are preferred here, since they avoid complications with concentration dependence of diffusion for highly condensable gases, and depend exclusively on penetrant shape and size. As expected, the corrected diffusion coefficients decrease by orders of magnitude with small differences in penetrant size. The diffusivities for all gases are much larger for the 6FDA:BPDA-DAM derived CMS compared to the Matrimid® derived CMS. Although ultramicropore windows are the diffusion limiting pores in CMS, the squared jump length in Equation 6.3 also enters into the effective diffusion coefficient, as was previously mentioned in Chapter 2 Section 2.3.2:

$$D_A = \frac{f_A \lambda_A^2}{6} \tag{6.3}$$

where f_A and λ_A are the random walk jumping frequency, and jump length, respectively (*36*). For a given CMS type, an *averag*e jump, $\lambda \sim d_\lambda$ in Figure 6.1, applies. In the context of the idealized models in Figure 6.4 and Figure 6.2, d_λ corresponds to the average distance *between the walls* in an average micropore, such as shown in Figure 6.5-(iv). The larger pore volumes at each effective size in 6FDA:BPDA-DAM-derived CMS compared to Matrimid® derived CMS in Figure 6.8 suggests larger average values of $\lambda \sim$

d_λ (cf. Figure 6.1) in 6FDA:BPDA-DAM derived CMS. This is due to presence of the bulky $–CF_3$ groups in the 6FDA unit of 6FDA:BPDA-DAM precursor, which disrupt polymer chain packing leading to a more open CMS structure after pyrolysis. This feature contributes to higher diffusion and sorption coefficients—and hence much higher permeabilities. The ratio of thermodynamically-corrected diffusivities, measures the *relative jump frequency* for members of a gas pair in each of the two CMS types. In all cases, these data show higher selectivities when considering a given gas pair in Matrimid® derived CMS, reflecting a more compact organization of the corresponding ultramicropores comprising the walls of the respective micropores. While these trends hold in general, understanding subtle differences in ultramicropore distributions of CMS membranes derived from different polymer precursors is essential to engineering CMS for specific gas separations. Two of the most important cases, CO_2/CH_4 and C_2H_4/C_2H_6 will be considered further to illustrate some principles and the utility of the framework provided by Figures 6.1, 6.5, 6.6 and 6.7.

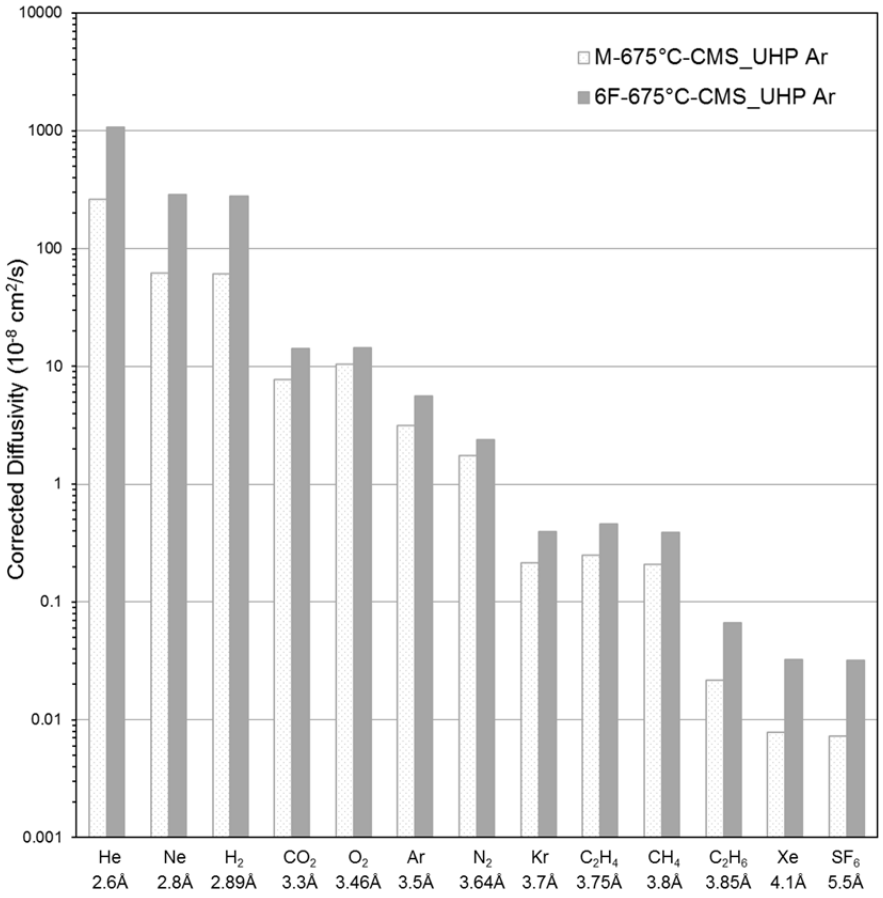

Figure 6.11. Corrected diffusivities of different gases at 35 °C for CMS derived from UHP Argon Pyrolysis of Matrimid® and 6FDA:BPDA-DAM to 675 °C.

Considering the CO_2/CH_4 separation, the CO_2 permeability of the 6FDA:BPDA-DAM derived CMS is approximately 230% higher than that of the Matrimid® derived CMS (due to combined higher CO_2 diffusion and sorption effects). Despite this large productivity advantage for the 6FDA:BPDA-DAM CMS over the Matrimid® CMS, the CO_2/CH_4 *diffusion selectivity* (shown in Table 6.3) is quite similar for both materials. From this perspective, considering 6FDA:BPDA-DAM CMS over Matrimid® CMS for CO_2/CH_4 separations is more desirable. In addition, this allows the 6FDA:BPDA-DAM CMS to be tuned to improve its CO_2/CH_4 selectivity even further while maintaining attractive permeability.

The technologically important C_2H_4/C_2H_6 pair is even more challenging to separate than the CO_2/CH_4 pair. Due to similarity in critical temperatures and size of these gases (Table 6.1), both sorption selectivity and diffusion selectivity of the C_2H_4/C_2H_6 pair tend to be low, thereby suppressing permselectivity (*37–39*). This pair is also particularly interesting, since it allows insights related to two relatively large penetrants with sizes *at the higher size tail end of the ultramicropore pore size distribution* illustrated in Figure 6.5. Considering CMS formed at 675 °C under UHP Argon, the C_2H_4 permeability of the 6FDA:BPDA-DAM CMS is approximately 320% higher than that of the Matrimid® CMS; however, the diffusion selectivity is 54% lower for the 6FDA:BPDA-DAM vs. Matrimid® derived CMS (shown in Table 6.3). This permeability-selectivity trade-off is especially apparent when considering the C_2H_4/C_2H_6 pair, and additional tools for tuning the selectivity without considerable permeability reductions become even more important.

Table 6.3.Corrected diffusion coefficients and diffusional selectivity properties of key gas pairs for Matrimid® and 6FDA:BPDA-DAM(1:1) CMS pyrolyzed to 675 °C under UHP Argon.

Gas	**σ (Å)**	**Matrimid®**		**6FDA:BPDA-DAM(1:1)**	
		Đ (cm^2/s)	**α_D**	**Đ (cm^2/s)**	**α_D**
CO_2	3.30	7.7 E-08	CO_2/CH_4 = 38.5	13.5 E-08	CO_2/CH_4 = 35.0
C_2H_4	3.75	2.5 E-09	C_2H_4/C_2H_6 = 12.3	4.5 E-09	C_2H_4/C_2H_6 = 5.7

An additional topic on the impacts of precursor polymer structure relates to the 6FDA:BPDA-DAM(1:1) precursor shown in Figure 6.3 with awareness that the BPDA component provides a potential weak point in the precursor backbone. In this regard, increasing the 6FDA:BPDA monomer ratio from (1:1) to (2:1) tends to reduce backbone

scissions in the stressed structure during aromatization. Larger, less mobile strands may suppress packing arrangement and lead to larger micropore volume and longer jump lengths in the (2:1) CMS variant. At the same time, after losing the CF_3H groups, a more linear strand structure in the 6FDA:BPDA (2:1) case will have less degrees of freedom of movement due to fewer biphenyl bonds in the aromatized strand. This second factor could provide an intrinsically tighter, more selective ultramicropore size distribution. For instance, when considering the CO_2/CH_4 pair, our preliminary work is consistent with these two aforementioned effects and interpretable in terms of higher micropore volume and longer jump lengths with tighter and a more size and shape selective ultramicropore distribution for the 2:1 variant. Specifically, the 675 °C pyrolyzed CMS 6FDA:BPDA-DAM(1:1) derived CMS gives 1100 Barrers CO_2 permeability and permselectivity CO_2/CH_4 = 66, while the CMS from the precursor 6FDA:BPDA-DAM(2:1) gave 2800 Barrers CO_2 permeability with selectivity CO_2/CH_4 = 77.

6.5 Additional Pore Size Tuning Tools

6.5.1 Oxygen Doping

As described in the previous section, the similar diffusion selectivity between CMS derived from Matrimid® and 6FDA:BPDA-DAM (cf. Table 6.3) provides a major opportunity for tuning of the later material. Specifically, the productivity advantage of the 6FDA:BPDA-DAM derived CMS can be leveraged by further controlled tightening of the ultramicropores to sacrifice some permeability to create a more selective membrane. This strategy, illustrated in Figure 6.12 by careful ultramicropore tuning via oxygen doping, results in moderate reductions in CO_2 permeability with significant selectivity

increases (*2*). Consistent with the representation in Figure 6.7, oxygen doping of the ultramicropore edges improves diffusion selectivity while maintaining large $\lambda \sim d_\lambda$ that results in high diffusivity, and high micropore sorption capacity, so permeability also remains high. In the context of Figure 6.7, oxygen doping primarily affects size selective ultramicropores rather than affecting the sorption coefficients. These oxygen doping results support the idea that modification of only the size selective ultramicropores can lead to a membrane material with both attractive selectivity and permeability. Although Figure 6.12 relates to 550 °C pyrolysis, the same approach could clearly be applied for the 675 °C pyrolysis conditions to further augment performance of the 6FDA:BPDA-DAM(2:1) CMS even beyond the appealing preliminary results noted for this case.

This ultrafine pore size engineering can also be extended to even more challenging gas pairs, for instance the C_2H_4/C_2H_6 pair which differ only by 0.1 Å in effective size (Table 6.1). Preliminary oxygen doping shows a remarkable effect for 6FDA:BPDA-DAM(1:1) for pyrolysis, with an optimum of 10 ppm O_2 in Argon at 675 °C, versus UHP Argon at 675 °C. Specifically, the permselectivity was raised more than 30% from 7.3 in Figure 6.10 to 9.6, with only moderate reduction of 30% in the attractive permeability under the 10 ppm O_2 in Argon versus UHP Argon at 675 °C. Additional detailed studies of oxygen doping for this gas pair will be presented in Chapter 7.

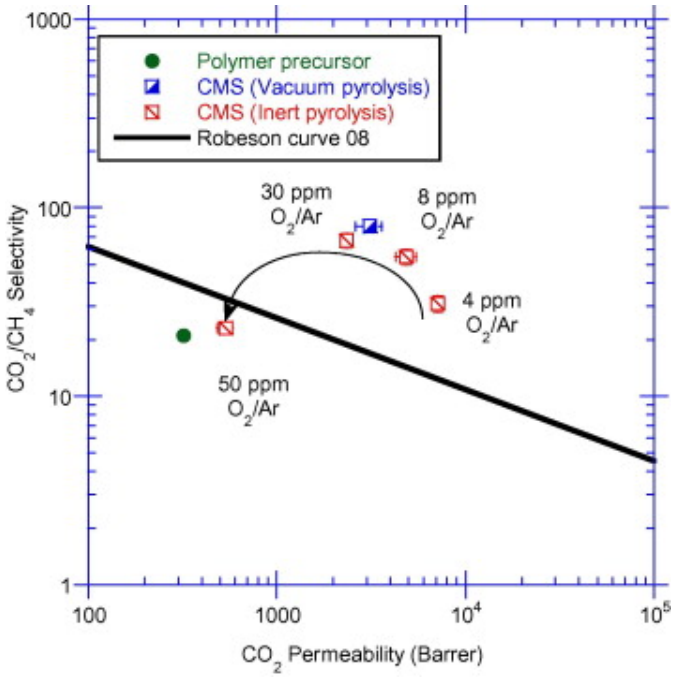

Figure 6.12. Separation performance of oxygen-doped 6FDA:BPDA-DAM(1:1) CMS films, pyrolyzed to 550 ^{0}C. Reprinted with permission from reference (*2*). Copyright 2010 Elsevier.

6.5.2 Amine Doping

The upper end of the CMS ultramicropore size distribution and the lower end of the micropore distribution (cf. Figures 6.5, 6.6, and 6.7) reflect morphological features that control separation of larger penetrants in the upper size range of Table 6.1. This terrain ideally allows diffusion jumps by more compact large penetrants without losing size and shape selectivity relative to slightly less compact large penetrants. Pore tuning in this range, therefore, provides additional insight into the complex domain in Figures 6.2, 6.5, 6.6, and 6.7 comprising large ultramicropores and small micropores as morphologically distinct entities, which is considered next. A small number of poorly packed strands within intercommunicating micropore walls should comprise the upper range of the ultramicropore distribution. On the other hand, local regions with more

"settled" plates having small values of $\lambda \sim d_\lambda$ in Equation 2.13 will comprise the lower range of the micropore distribution. In fact, the largest ultramicropores may effectively comprise defects in packing associated with the chaotic drive towards ordered plates, which may not be so neatly organized as the idealized representation in Figure 6.5. Indeed, the actual CMS composition (Table B.1 in Appendix B), while envisioned to comprise mostly C, H, and N, with structures illustrated in Figure 6.5, also includes some oxygen *even when formed under UHP Argon*. Although speculative, we envision naturally occurring, residual oxygen-containing sites to be associated with such regions of less perfection created during the chaotic scission and organization process.

These residual oxygen-containing sites may provide a route for selective functionalization of the CMS membranes with carefully selected "dopants", sharpening the upper ultramicropore and lower micropore size distributions illustrated in Figure 6.5. This observation motivated the work presented in Chapter 4 (*3*), exploiting this fact as an extension of the more conventional oxygen doping concept, noted earlier in Figure 6.7. As shown in Figure 6.13 addition of small molecule dopants are envisioned to functionalize the larger slits resulting from imperfect packing of strands in the CMS structure. In the context of Figure 6.13, treatment of conventionally-produced CMS was doped with trace amounts (1000 - 10 ppm) of *p*-phenylenediamine (PPDA) in tetrahydrofuran (THF) (*3*). While a wide array of molecular dopants can be envisioned, utilization of diamines in this preliminary study was based on the fact that small amine penetrants introduced to the CMS are tenaciously, even covalently retained (*40*). This preliminary work was done on identical asymmetric CMS membranes with the same thin

dense layer formed at 550 °C, so productivity is reported in GPU (1 GPU = 10^{-6} cc(STP)/cm^2 cmHg).

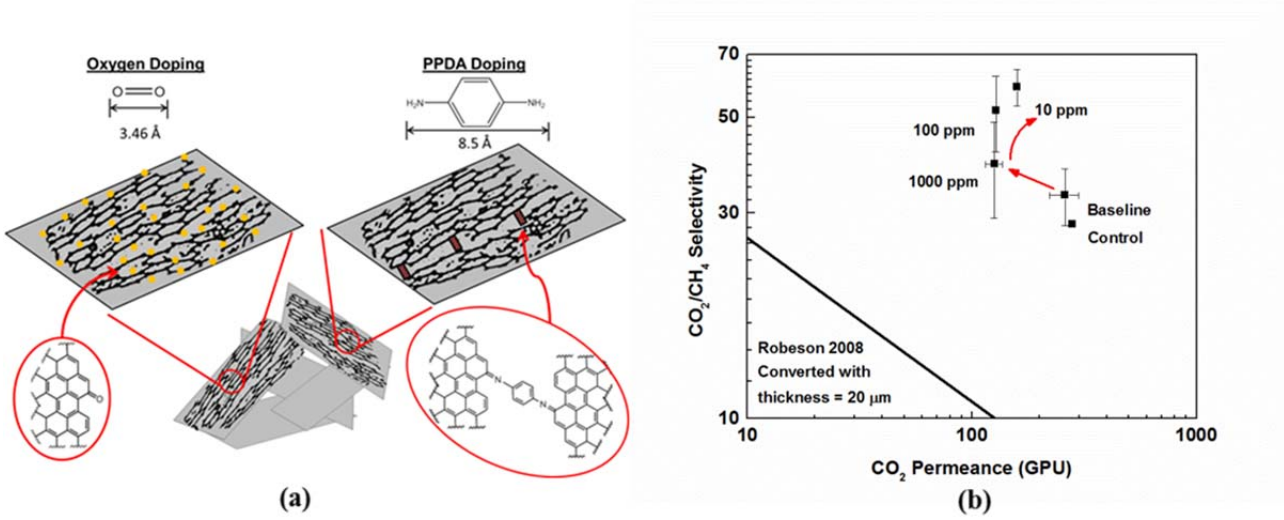

Figure 6.13. (a) Comparison of oxygen and "amine doping" techniques. (b) Performance of amine doped 6FDA:BPDA-DAM CMS membranes for CO_2/CH_4 separation. Reprinted with permission from reference (*3*). Copyright 2016 Wiley.

The lower pyrolysis temperature, compared to 675 °C, was chosen to maintain larger micropore dimensions (cf. Figure 6.6) to provide high sorption capacity (C'_{HA}) and diffusion jump lengths (d_λ in Figure 6.1). The provocative trends in Figure 6.13 suggest that amines may be suited to sharpen the large end of the ultramicropore range to complement oxygen doping for the small and mid-range ultramicropores. Combining these two ultramicropore engineering tools will provide abilities to refine CMS for such larger penetrants such as the olefin-paraffin pairs, as well as smaller ones in Figure 6.7 and Table 6.1.

6.6 Conclusions

Differences in CMS structure and performance resulting from the use of different polymer precursors, while keeping other pyrolysis conditions fixed, were discussed. Sorption uptake measurements were used to characterize the CMS micropore distribution. A gas probe method provided insight into changes in CMS transport properties in terms of differences in ultramicropore distributions, leading to changes in CMS performance. As with other studies, the relationship between precursor and ultimate CMS properties was shown to be more complex than one related only to precursor fractional free volume. The 6FDA:BPDA-DAM 675 °C CMS shows a higher C_2H_4 permeability but lower C_2H_4/C_2H_6 selectivity compared to the Matrimid® CMS. This general permeability-selectivity trade-off however may not always be obvious since in the case of CO_2/CH_4 separation, the 6FDA:BPDA-DAM CMS shows a comparable selectivity as the Matrimid® CMS, but with much higher permeability. This is especially important when the effects due to multiple pyrolysis parameters are coupled. For example, simply increasing the pyrolysis temperature may result in a CMS with higher selectivity but lower permeability as seen in going from pyrolysis of Matrimid® at 500 °C vs. 675 °C (*11*). On the other hand changing the polymer precursor to 6FDA:BPDA-DAM while increasing the pyrolysis temperature at the same time may produce a more optimal CMS avoiding this unwanted trade-off, as was demonstrated for CO_2/CH_4 separation. Careful consideration of the CMS micropore and ultramicropore distributions is thus important for engineering CMS for a given gas separation application.

6.7 References

(1) Rungta, M. Carbon Molecular Dense Film Membranes for Ethylene/Ethane Separations, Georgia Institute of Technology, 2012. Ph.D. Thesis.

(2) Kiyono, M.; Williams, P. J.; Koros, W. J. Effect of polymer precursors on carbon molecular sieve structure and separation performance properties. *Carbon* **2010**, *48*, 4432–4441.

(3) Wenz, G. B.; Koros, W. J. Tuning Carbon Molecular Sieves for Natural Gas Separations: A Diamine Approach. *AIChE J.* **2017**, *63*, 751–760.

(4) Koresh, J. E.; Sofer, A. The Carbon Molecular-sieve Membranes: General Properties and Permeability of CH4/H2 Mixtures. *Sep. Sci. Technol.* **1987**, *22*, 973–982.

(5) Rouqurol, J.; Avnir, D.; Fairbridge, C.; Everett, D.; Haynes, J.; Pernicone, N.; Ramsay, J.; Sing, K.; Unger, K. Recommendations for the characterization of porous solids. *Pure Appl. Chem.* **1994**, *66*, 1739–1758.

(6) Jenkins, G. M.; Kawamura, K. *Polymeric Carbons -- Carbon Fibre, Glass and Char*; Cambridge University Press, 1976.

(7) Mariwalat, R. K.; Foley, H. C. Evolution of Ultramicroporous Adsorptive Structure in Poly (furfuryl alcohol) - Derived Carbogenic Molecular Sieves. *Ind. Eng. Chem. Res.* **1994**, *33*, 607–615.

(8) Steel, K. M.; Koros, W. J. An investigation of the effects of pyrolysis parameters on gas separation properties of carbon materials. *Carbon* **2005**, *43*, 1843–1856.

(9) Kim, Y. K.; Lee, J. M.; Park, H. B.; Lee, Y. M. The gas separation properties of carbon molecular sieve membranes derived from polyimides having carboxylic acid groups. *J. Memb. Sci.* **2004**, *235*, 139–146.

(10) Xiao, Y.; Chung, T.; Chng, M. L.; Tamai, S.; Yamaguchi, A. Structure and Properties Relationships for Aromatic Polyimides and Their Derived Carbon Membranes : Experimental and Simulation Approaches. *J. Phys. Chem. B* **2005**, *109*, 18741–18748.

(11) Rungta, M.; Xu, L.; Koros, W. J. Structure–performance characterization for carbon molecular sieve membranes using molecular scale gas probes. *Carbon* **2015**, *85*, 429–442.

(12) Fu, Y.-J.; Liao, K.-S.; Hu, C.-C.; Lee, K.-R.; Lai, J.-Y. Development and characterization of micropores in carbon molecular sieve membrane for gas separation. *Microporous Mesoporous Mater.* **2011**, *143*, 78–86.

(13) Park, H. B.; Kim, Y. K.; Lee, J. M.; Lee, S. Y.; Lee, Y. M. Relationship between chemical structure of aromatic polyimides and gas permeation properties of their carbon molecular sieve membranes. *J. Memb. Sci.* **2004**, *229*, 117–127.

(14) Campo, M. C.; Magalhães, F. D.; Mendes, A. Comparative study between a CMS membrane and a CMS adsorbent: Part I—Morphology, adsorption equilibrium and kinetics. *J. Memb. Sci.* **2010**, *346*, 15–25.

(15) Chen, J.; Loo, L. S.; Wang, K.; Do, D. D. The structural characterization of a CMS membrane using Ar sorption and permeation. *J. Memb. Sci.* **2009**, *335*, 1–4.

(16) Fu, S.; Sanders, E. S.; Kulkarni, S. S.; Koros, W. J. Carbon molecular sieve membrane structure–property relationships for four novel 6FDA based polyimide precursors. *J. Memb. Sci.* **2015**, *487*, 60–73.

(17) Williams, P. J. Analysis of Factors Influencing The Performance of CMS Membranes for Gas Separations, Georgia Institute of Technology, 2006. Ph.D. Thesis.

(18) Hatori, H.; Yamada, Y.; Shiraishi, M.; Yoshihara, M.; Kimura, T. The mechanism of polyimide pyrolysis in the early stage. *Carbon* **1996**, *34*, 201–208.

(19) Inagaki, M.; Harada, S.; Sato, T.; Nakajima, T.; Horino, Y.; Morita, K. Carbonization of polyimide film "Kapton." *Carbon* **1989**, *27*, 253–257.

(20) Bürger, A.; Fitzer, E.; Heym, M.; Terwiesch, B. Polyimides as precursors for artificial carbon. *Carbon N. Y.* **1975**, *13*, 149–157.

(21) Ehlers, G. F. L.; Fisch, I. R.; Powell, W. R. Thermal Degradation of Polymers with Phenylene Units in the Chain . IV . Aromatic Polyamides. *J. Polym. Sci. Part A Polym. Chem.* **1970**, *8*, 3511–3527.

(22) Turk, M. J.; Ansari, A. S.; Alston, W. B.; Gahn, G. S.; Frimer, A. A.; Scheiman, D. A. Evaluation of the thermal oxidative stability of polyimides via TGA techniques. *J. Polym. Sci. Part A Polym. Chem.* **1999**, *37*, 3943–3956.

(23) Flory, P. J. Molecular Theory of Liquid Crystals. *Adv. Polym. Sci.* **1984**, *59*, 1–36.

(24) Xu, L.; Rungta, M.; Hessler, J. V.; Qiu, W.; Brayden, M.; Martinez, M.; Barbay, G.; Koros, W. J. Physical aging in carbon molecular sieve membranes. *Carbon* **2014**, *80*, 155–166.

(25) Ma, X.; Williams, S.; Wei, X.; Kniep, J.; Lin, Y. S. Propylene/Propane Mixture Separation Characteristics and Stability of Carbon Molecular Sieve Membranes. *Ind. Eng. Chem. Res.* **2015**, *54*, 9824–9831.

(26) Grisdale, R. O. The Properties of Carbon Contacts. *J. Appl. Phys.* **1953**, *24*, 1288.

(27) Kiyono, M. Carbon Molecular Sieve Membranes For Natural Gas Separations, Georgia Institute of Technology, 2010. Ph.D. Thesis.

(28) Fu, S.; Wenz, G. B.; Sanders, E. S.; Kulkarni, S. S.; Qiu, W.; Ma, C.; Koros, W. J. Effects of pyrolysis conditions on gas separation properties of 6FDA/DETDA:DABA(3:2) derived carbon molecular sieve membranes. *J. Memb. Sci.* **2016**, *520*, 699–711.

(29) Kandambeth, S.; Mallick, A.; Lukose, B.; Mane, M. V.; Heine, T.; Banerjee, R. Construction of crystalline 2D covalent organic frameworks with remarkable chemical (Acid/Base) stability via a combined reversible and irreversible route. *J. Am. Chem. Soc.* **2012**, *134*, 19524–19527.

(30) Roberts, J. D.; Caserio, M. C. *Basic Principles of Organic Chemistry*; W. A. Benjamin, Inc.: New York, NY, 1965.

(31) Breck, D. W. *Zeolite Molecular Sieves: Structure, Chemistry, and Use*; Wiley & Sons: New York, NY, 1974.

(32) Reid, R. C.; Prausnitz, J. M.; Sherwood, T. K. *The Properties of Gases and Liquids*; 3rd ed.; McGraw-Hill: New York, NY, 1977.

(33) Bird, R. B.; Stewart, W. E.; Lightfoot, E. N. *Transport Phenomena*; 2nd ed.; John Wiley and Sons: New York, NY, 2002.

(34) Rungta, M.; Zhang, C.; Xu, L.; Koros, W. J. Membrane-Based Ethylene/Ethane Separation: The Upper Bound and Beyond. *AIChE J.* **2013**, *59*, 3475–3489.

(35) Mukaddam, M.; Litwiller, E.; Pinnau, I. Gas Sorption, Diffusion, and Permeation in Nafion. *Macromolecules* **2016**, *49*, 280–286.

(36) Petropoulos, J. H. Some fundamental approaches to membrane gas permeability and permselectivity. *J. Memb. Sci.* **1990**, *53*, 229–258.

(37) Tanaka, K.; Taguchi, A.; Hao, J.; Kita, H.; Okamoto, K. Permeation and separation properties of polyimide membranes to olefins and paraffins. *J. Memb. Sci.* **1996**, *121*, 197–207.

(38) Salinas, O.; Ma, X.; Litwiller, E.; Pinnau, I. Ethylene/ethane permeation, diffusion and gas sorption properties of carbon molecular sieve membranes derived from the prototype ladder polymer of intrinsic microporosity (PIM-1). *J. Memb. Sci.* **2016**, *504*, 133–140.

(39) Salinas, O.; Ma, X.; Litwiller, E.; Pinnau, I. High-performance carbon molecular sieve membranes for ethylene/ethane separation derived from an intrinsically microporous polyimide. *J. Memb. Sci.* **2016**, *500*, 115–123.

(40) Jones, C. W.; Koros, W. J. Carbon molecular sieve gas separation membranes-II. Regeneration following organic exposure. *Carbon* **1994**, *32*, 1427–1432.

CHAPTER 7. LOW-LEVEL OXYGEN DOPING OF CARBON MOLECULAR SIEVE MEMBRANES FOR ETHYLENE/ETHANE SEPARATIONS

7.1 Overview

Olefin/paraffin separations represent a large fraction of energy usage in petrochemical industry. Across the olefin/paraffin separation landscape the ethylene/ethane separation is one of critical importance, and a significant challenge due to the similarities in size and condensability of the two gases (cf. Table 7.1). Currently, separation of C_2H_4 from C_2H_6 is performed via cryogenic distillation, where process conditions can require column temperatures of -23 ^{o}C and pressures of 320 psig, resulting in high capital and energy costs.

Membranes offer an attractive combination of low capital, operating and maintenance costs, making them an attractive choice for implementation in large-scale gas separation processes. While membranes are an alternative to traditional phase-change based separation techniques (i.e. distillation), current polymeric membrane materials exhibit low separation efficiency for the C_2H_4/C_2H_6 separation, so direct replacement of traditional distillation processes is currently not feasible (*1*, *2*). Alternatively, membranes could be implemented as complementary separators into a hybrid membrane-distillation process for olefin/paraffin separations, where the membrane units could reduce the associated distillation column duties (*3*). In this configuration the membrane separator would be used for bulk separations and traditional cryogenic distillation for "polishing"

the product stream, enabling the > 99.9% C_2H_4 purity levels required for chemical manufacturing.

Table 7.1. Critical temperature (T_c) from (*4*) and size (σ) of C_2H_4 and C_2H_6 defined on slit-like pores using space-filling CPK models and calibrated "slits" (2, 7).

Gas	T_c (K)	σ (Å)
C_2H_4	283	3.75
C_2H_6	306	3.85

Integration of membrane modules into hybrid distillation processes has motivated a significant amount of research for development of high performance stable membrane materials for C_2H_4/C_2H_6 separations, from which CMS membranes have emerged as an attractive class as the combination of micropores and ultramicropores allow for both high permeability and high selectivity via a molecular sieving effect (*5*, *6*). Additionally, unlike their polymeric precursors, CMS materials do not experience plasticization when exposed to high pressure condensable feeds owing to their rigid structure (*7–11*).

Penetrant diffusion through the critical ultramicropore windows requires molecules to overcome energetic repulsion from the rigid CMS ultramicropore surface, and small changes in ultramicropore window size can result in significant differences in the activation energy associated for these processes (*12–14*). For the C_2H_4/C_2H_6 pair, prior work on O_2/N_2 and N_2/CH_4 was extended to establish a fundamental framework for materials development; specifically, examination of two limiting cases in activated diffusion of C_2H_4 and C_2H_6 in CMS materials, shown in Figure 7.1 (*9*).

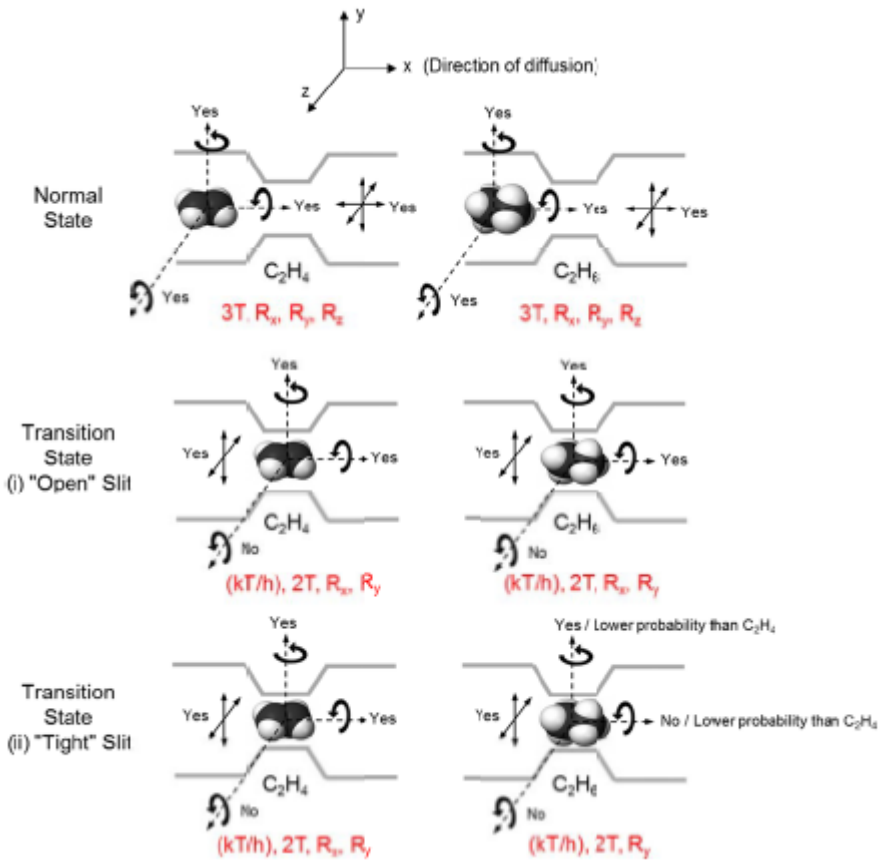

Figure 7.1. Representation of degrees of freedom in the normal and transition states for (i) "open" CMS slit and (ii) "tight" CMS slit for C_2H_4 and C_2H_6 transport through a CMS membrane. Reproduced from (*9*).

Considering the case represented in Figure 7.1 – (i), the "open" CMS pore structure allows rotation of both C_2H_4 and C_2H_6 around both x and y axes within the activated transition state. Within this configuration, the entropic selectivity factor (described in Chapter 2) has been shown to be as low as 1.2 (*9*). CMS materials formed at low final pyrolysis temperature result in a more "open" pore structure, as there is limited exposure to high temperature where CMS strand mobility is high leading to a higher degree of disorder in the resulting "plates" that comprise the micropore cells.

Higher final pyrolysis temperatures allow for increased CMS strand and plate mobility, annealing the CMS structures, resulting in a "tight" slit case shown in Figure 7.1-(ii). This configuration allows rotation of the smaller C_2H_4 around both x and y axes while restricting rotation of C_2H_6 around the x axis. In this case, the entropic selectivity has been shown to be as high as 31 (*9*).

While transitioning from an "open" to a "tight" CMS structure can be controlled via final pyrolysis temperature, incremental temperature changes can lead to dramatic effects upon transport performance, particularly for larger gas penetrants like C_2H_4 and C_2H_6 considered here. Rungta *et. al.* demonstrated that increasing pyrolysis temperature from 550 °C to 675 °C for Matrimid® derived CMS membranes results in a step-change in C_2H_4/C_2H_6 selectivity from ~6 to ~12 while maintaining ~15 Barrer C_2H_4 permeability (*15*). However, increasing from 675 °C to 800 °C showed minimal selectivity enhancement for C_2H_4/C_2H_6 coupled with dramatic permeability reductions to < 1 Barrer C_2H_4. Similar experiments performed on 6FDA:BPDA-DAM(1:1) derived CMS indicated: 1) the lack of a step-change in C_2H_4/C_2H_6 selectivity over the temperatures investigated; 2) 6FDA:BPDA-DAM(1:1) derived CMS displayed much higher permeabilities coupled with lower selectivities (*15*). Considering CMS formed under UHP Ar at 675 °C, 6FDA:BPDA-DAM(1:1) CMS displays ~320% higher C_2H_4 permeability than Matrimid® CMS, whereas the diffusional selectivity for the 6FDA:BPDA-DAM(1:1) CMS is ~54% lower than Matrimid® CMS. These results suggest that developing pore tuning tools that increase selectivity with minimal permeability reductions are even more important, particularly in the case of critical gas

separations like C_2H_4/C_2H_6 being examined here as compared to previously studied smaller penetrants.

During CMS formation, introduction of parts per million of molecular oxygen into the pyrolysis atmosphere leads to selective functionalization of the strand edges that comprise the aromatic plates, depicted in Figure 7.2 below (*16*). This technique, referred to as oxygen doping, was previously shown to modify only the size selective ultramicropores in Matrimid® derived CMS, as the exposed carbon edges are ~17x more reactive towards molecular oxygen than the basal planes (*17*, *18*). This modification results in a tightening of the size-selective ultramicropore distribution, *not the micropores responsible for sorption*; thereby, leading to increased membrane selectivity with moderate permeability reductions. Similar studies on CMS membranes derived from 6FDA-based polyimide precursors showed the same effect applies, and is believed to be general to all CMS materials (*19*).

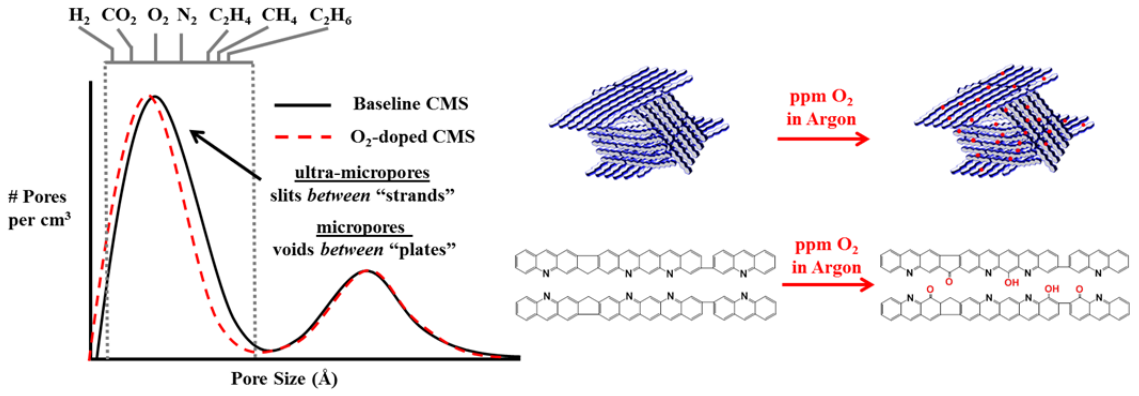

Figure 7.2. Schematic representation of oxygen doping of CMS structure indicates tightening of ultramicropore distribution with no changes in micropore distribution.

Until now oxygen doping has been primarily used for O_2/N_2 and CO_2/CH_4 separations (*16*, *19*), but extension of this ultra-fine pore tuning technique to the more challenging C_2H_4/C_2H_6 gas pair, which differ by only 0.1 Å in effective size (cf. Table 7.1), may allow for increased performance for CMS materials. An initial oxygen doping study of 6FDA:BPDA-DAM(1:1) derived CMS membranes for the C_2H_4/C_2H_6 separation investigated conditions that had resulted in optimal CO_2/CH_4 performance (i.e. 30 and 50 ppm O_2 in Argon); however, CMS formed under these conditions displayed minimal C_2H_4/C_2H_6 selectivity enhancement, with significant C_2H_4 permeability losses indicating higher oxygen concentrations resulted in "over-doping" of the CMS pore structure (*15*). While addition of ppm levels of oxygen to the pyrolysis atmosphere results in performance enhancement, there is a maximum concentration for which attractive performance is attained. Increasing the pyrolysis atmosphere oxygen concentration past this critical point leads to a loss of both *permeability and selectivity* as a result of "over-doping" the CMS membrane. This can be understood in terms of shifts in the ultramicropore distribution, shown in Figure 7.3, where "over-doping" of the CMS membrane leads to an excessively tight ultramicropore distribution. The remaining pathways within "over-doped" materials result in exclusion of all penetrants, leading to reductions in productivity. However, existence of a few pathways large enough to provide minimal selectivity enhancement via oxygen doping will result in "over-doped" CMS membranes displaying lower selectivity compared to "optimal" or even un-doped cases. Of course, pyrolysis atmosphere oxygen concentrations corresponding to "optimal" and "over-doping" conditions will be dependent upon a variety of factors (e.g.

final pyrolysis temperature and gas pair of interest), but is expected to be general to the technique.

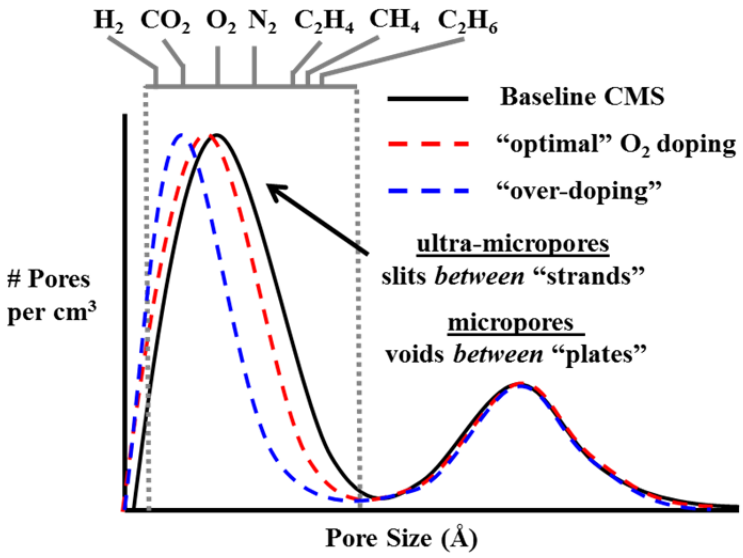

Figure 7.3. Representation of ultramicropore shifts caused by oxygen doping of CMS materials: "optimal" doping shows slight narrowing of ultramicropore distribution, whereas "over-doping" occurs at higher pyrolysis atmosphere oxygen concentration leading to overly tight pore structure.

Considering the differences in effective sizes between CO_2/CH_4 (0.5 Å) and C_2H_4/C_2H_6 (0.1 Å), it should not be surprising that CMS formation conditions optimized for CO_2/CH_4 separations may not exhibit optimal performance for C_2H_4/C_2H_6 separations and vice versa. Therefore, it is believed that lower concentrations of molecular oxygen in the pyrolysis atmosphere will result in C_2H_4/C_2H_6 selectivity enhancements with minor C_2H_4 permeability reductions, and will be investigated here.

7.2 Permeation Results of Oxygen Doped Carbon Molecular Sieve Membranes for the C_2H_4/C_2H_6 Separation

Detailed oxygen doping studies of 6FDA:BPDA-DAM (1:1) derived CMS formed at 675 ^{0}C are reported in Figure 7.4. Examination of the results shows a balance between oxygen concentration and resultant membrane performance, similar to the previously investigated CO_2/CH_4 separation (*16*). However, unlike the CO_2/CH_4 case the "optimum" oxygen concentration for the C_2H_4/C_2H_6 case occurs as lower concentration; 10 ppm O_2/Ar for C_2H_4/C_2H_6 case versus 30 ppm O_2/Ar for CO_2/CH_4 case. Upon changing the pyrolysis atmosphere from UHP Ar to 10 ppm O_2/Ar, the resulting membranes display ~140 % increase in permselectivity to 9.6 with a corresponding 33% decrease in permeability, due to the selective tightening of the ultramicropores. Increasing the pyrolysis oxygen concentration from 10 ppm to 20 ppm (balance Ar) results in "over-doping" of the CMS, resulting in loss of both permeability and selectivity with performance lower than the UHP Ar case. These results, in the context of Figure 7.3, suggest that increasing pyrolysis oxygen concentration from 10 ppm O_2 to 20 ppm O_2/Ar results in removal a number of pathways, previously selective for C_2H_4 over C_2H_6, from the accessible region in the distribution. Meanwhile, a small number of larger low selectivity pores that exhibit minimal enhancement from oxygen doping remain active, leading towards an overall reduction in selectivity at the higher (20 ppm O_2/Ar) concentration.

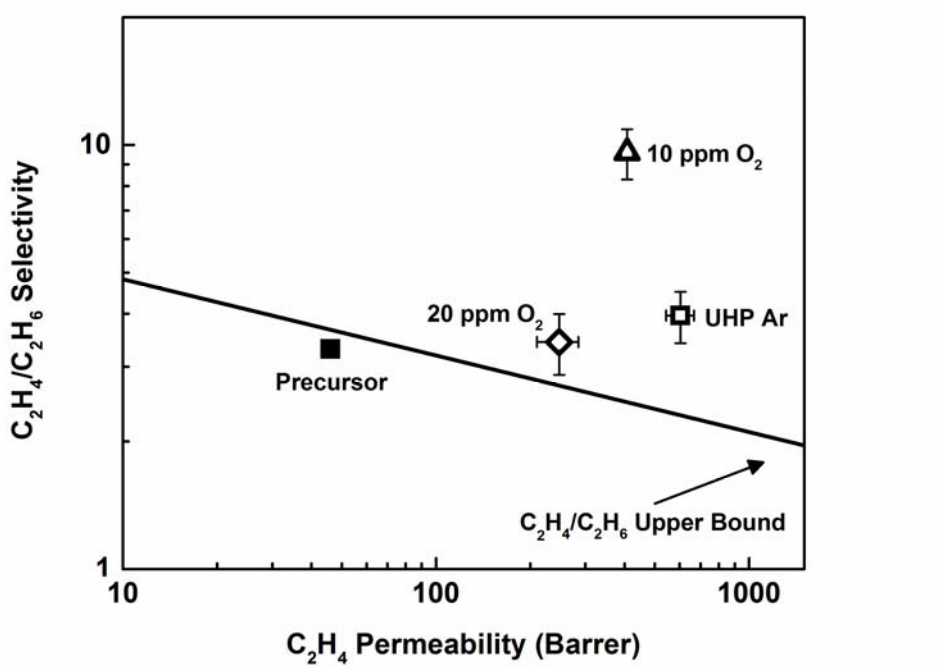

Figure 7.4. Separation performance of 6FDA:BPDA-DAM(1:1) derived CMS membranes pyrolyzed under varying concentrations of oxygen in UHP Ar at 675 °C for the C_2H_4/C_2H_6 gas pair. Labels represent the oxygen concentration in pyrolysis atmosphere. Permeation experiments conducted at 50 psia and 35 °C. Polymeric upper bound for C_2H_4/C_2H_6 from (*20*).

7.3 Effects of Oxygen Doping upon Sorption and Diffusivity of C_2H_4 and C_2H_6 in Carbon Molecular Sieve Membranes

Gas sorption measurements of C_2H_4 and C_2H_6 at 35 °C were performed on 6FDA:BPDA-DAM(1:1) derived CMS pyrolyzed to 675 °C under varying concentrations of oxygen in UHP Ar to probe the effects on CMS microporous structure and are presented in Figure 7.5 and Figure 7.6, respectively. Markers within these figures correspond to experimentally measured sorption capacities, while corresponding Langmuir isotherm fits are represented by the curves, with fit parameters summarized in Table 7.2.

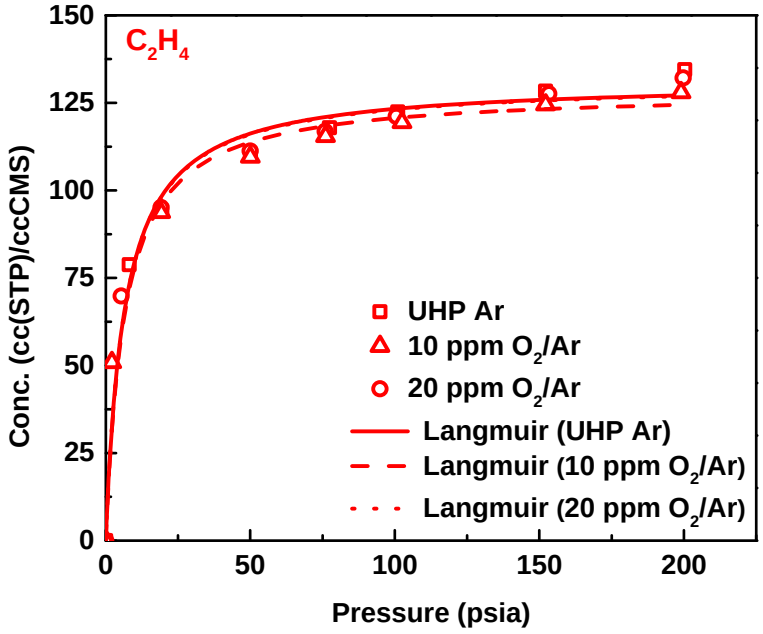

Figure 7.5. Pure gas sorption isotherm of C_2H_4 at 35 ^{0}C in 6FDA:BPDA-DAM(1:1) derived CMS membranes formed under different pyrolysis atmospheres. Fitted lines correspond to Langmuir model.

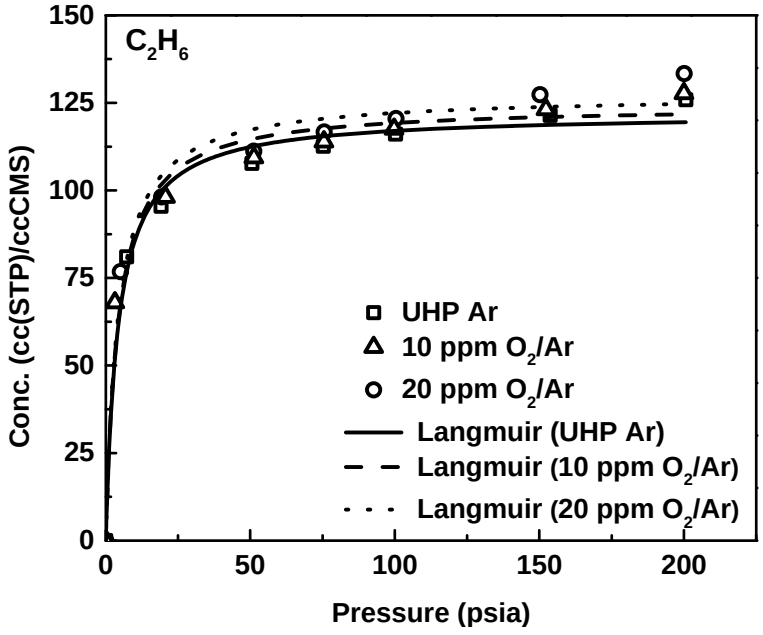

Figure 7.6. Pure gas sorption isotherm of C_2H_6 at 35 ^{0}C in 6FDA:BPDA-DAM(1:1) derived CMS membranes formed under different pyrolysis atmospheres. Fitted lines correspond to Langmuir model.

Table 7.2. Langmuir fit parameters for sorption of C_2H_4 and C_2H_6 at 35 ^{0}C in 6FDA:BPDA-DAM(1:1) CMS membranes pyrolyzed under different pyrolysis atmospheres.

Gas	Atmosphere	C_H' [cm^3 (STP)/cm^3 CMS]	*b* [1/psia]
C_2H_4	**UHP Ar**	131.3 ± 3.2	0.155 ± 0.025
	10 ppm O_2/Ar	128.5 ± 3.5	0.155 ± 0.025
	20 ppm O_2/Ar	131.0 ± 2.3	0.155 ± 0.025
C_2H_6	**UHP Ar**	122.0 ± 2.5	0.234 ± 0.038
	10 ppm O_2/Ar	124.4 ± 2.9	0.234 ± 0.038
	20 ppm O_2/Ar	127.3 ± 2.5	0.234 ± 0.038

If the idealized representation of CMS materials presented in Figure 7.2 is accepted, it is reasonable to assume that size selective ultramicropores add negligible area for gas sorption compared to the larger micropores. Examining the sorption isotherms in Figure 7.5 and Figure 7.6 indicates that regardless of the concentration investigated within this study, oxygen doping has no effect upon the equilibrium sorption capacity of either C_2H_4 or C_2H_6, similar to previously noted studies of oxygen doping for CO_2/CH_4 and O_2/N_2 (*17*, *19*). These results confirm oxygen doping only modifies the size selective ultramicropores, *not the larger micropores responsible for gas sorption*, and seems to be general to all CMS materials for all gas penetrants. Tabulated sorption coefficients (cf. Table 7.3) further support this notion; regardless of pyrolysis atmosphere, sorption coefficients for C_2H_4 and C_2H_6 are essentially identical. Furthermore, sorption selectivities for all samples are essentially unity, owing to the similar condensabilities of both penetrants, shown in Table 7.1.

Table 7.3. Pure gas sorption coefficients and sorption selectivity of CMS membranes derived from 6FDA:BPDA-DAM(1:1) pyrolyzed to 675 ^{o}C under different pyrolysis atmospheres at 35 ^{o}C and 50 psia.

Atmosphere	$\mathbb{S}_{C_2H_4}$ [cm^3 (STP)/ (cm^3 CMS-psia)]	$\mathbb{S}_{C_2H_6}$ [cm^3 (STP)/ (cm^3 CMS-psia)]	$\alpha_{\mathbb{S}}$
UHP Ar	2.32 ± 0.54	2.25 ± 0.52	1.03 ± 0.34
10 ppm O_2/Ar	2.28 ± 0.53	2.29 ± 0.53	0.99 ± 0.33
20 ppm O_2/Ar	2.32 ± 0.54	2.34 ± 0.54	0.99 ± 0.32

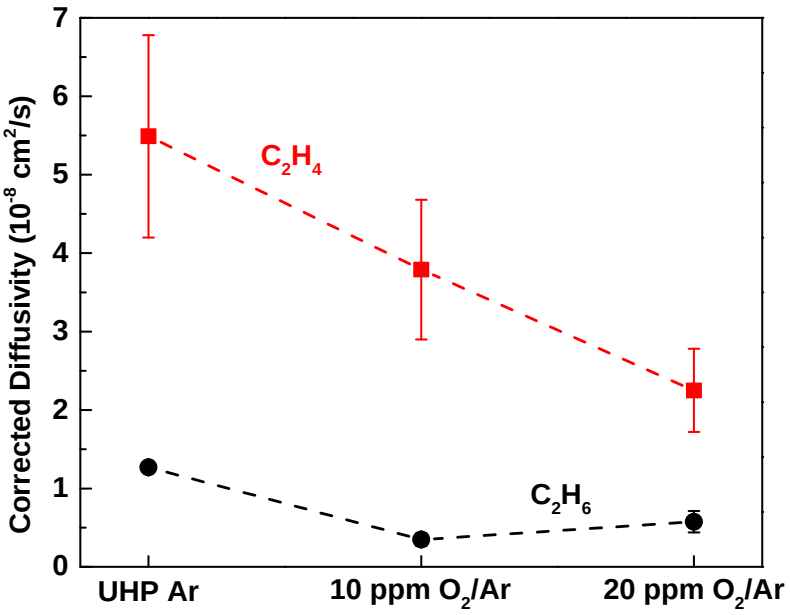

Figure 7.7. Thermodynamically corrected diffusivities of C_2H_4 and C_2H_6 at 35 °C for 6FDA:BPDA-DAM(1:1) derived CMS formed at 675 °C under different pyrolysis atmospheres.

Thermodynamically corrected diffusion coefficients for C_2H_4 and C_2H_6 for oxygen doped CMS membranes are reported in Figure 7.7. Addition of 10 ppm O_2 into the pyrolysis atmosphere results in a 31% reduction from 5.49 x 10^{-8} to 3.79 x 10^{-8} cm^2/s in C_2H_4 diffusivity, and 73% reduction from 1.27 x 10^{-8} to 3.48 x 10^{-9} cm^2/s for C_2H_6. Reductions in diffusivity indicate a "tighter" CMS structure as result of the oxygen doping of the ultramicropores, clearly affecting the larger C_2H_6 more than the smaller C_2H_4 as reflected by the relative diffusivity reductions. Increasing the oxygen concentration from 10 ppm to 20 ppm has minimal effect upon C_2H_6 diffusivity, but reduces C_2H_4 diffusivity an additional 28% to 2.26 x 10^{-8} cm^2/s. This behavior supports the "over doping" permeation performance of the 20 ppm O_2/Ar CMS membrane, as

these conditions result in an overly tight pore structure restricting transport of both penetrants but one that impacts C_2H_4 more than C_2H_6. Corrected diffusion and sorption selectivities reported in Figure 7.8 show that diffusion selectivity closely matches the permselectivity reported in Figure 7.4, highlighting the dominance of size and shape discrimination within these CMS materials.

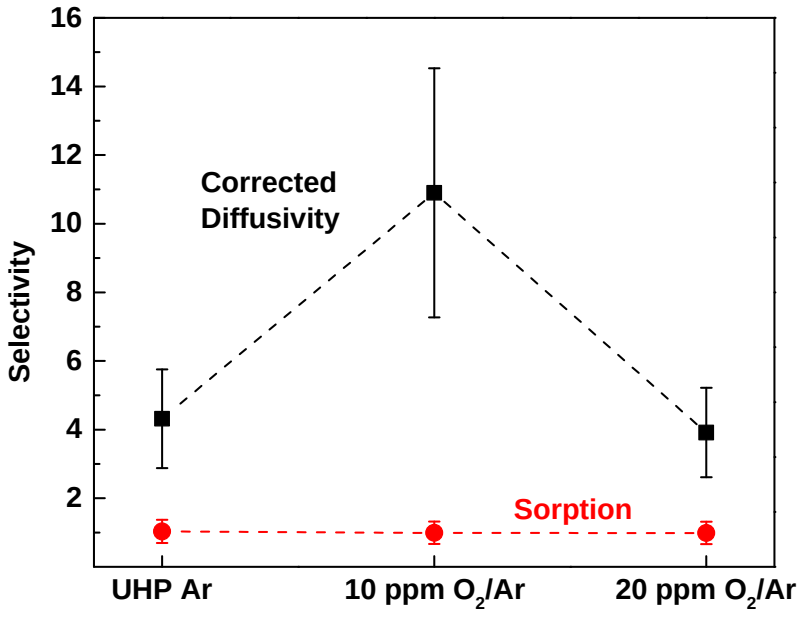

Figure 7.8. Corrected diffusion (Đ) and sorption selectivities of oxygen doped 6FDA:BPDA-DAM(1:1) derived CMS formed at 675 °C at 50 psia, 35 °C.

7.4 Pore Size Distribution of Oxygen Doped Carbon Molecular Sieve Membranes from CO_2 Sorption

Low pressure CO_2 sorption on microporous materials, like CMS, can be used to probe features responsible for molecular sieving and is complementary to more traditional transport results (*21*). Figure 7.9 below shows the DFT-derived pore size distributions for 6FDA:BPDA-DAM(1:1) derived CMS pyrolyzed to 675 °C under varying pyrolysis oxygen concentrations from CO_2 sorption measurements at 0 ^{0}C, assuming a carbon-slit geometry (*22*). As expected, all of the samples in this study exhibit a bimodal distribution of pore sizes. Comparisons of distributions from samples pyrolyzed under UHP Ar and 10 ppm O_2/Ar show very little difference, further supported by the measured pore volume and surface area reported in Table 7.4. This suggests oxygen doping at 10 ppm O_2/Ar is truly a fine tuning technique, considering the effect upon transport results discussed previously. Increasing the pyrolysis atmosphere oxygen content from 10 ppm to 20 ppm results in a loss of pore volume primarily in the ultramicropore range (<7 Å), suggesting a number of ultramicropores are transitioning to an excessively tight structure resulting from the higher oxygen concentration. It should be noted that this technique is limited to pores ≥ 4 Å, so small ultramicropores (< 4 Å) responsible for molecular sieving of the penetrants of interest here cannot be directly probed. Thus, permeability-selectivity trends cannot be conclusively determined from these measurements; however, it can be useful to corroborate results from traditional transport measurements.

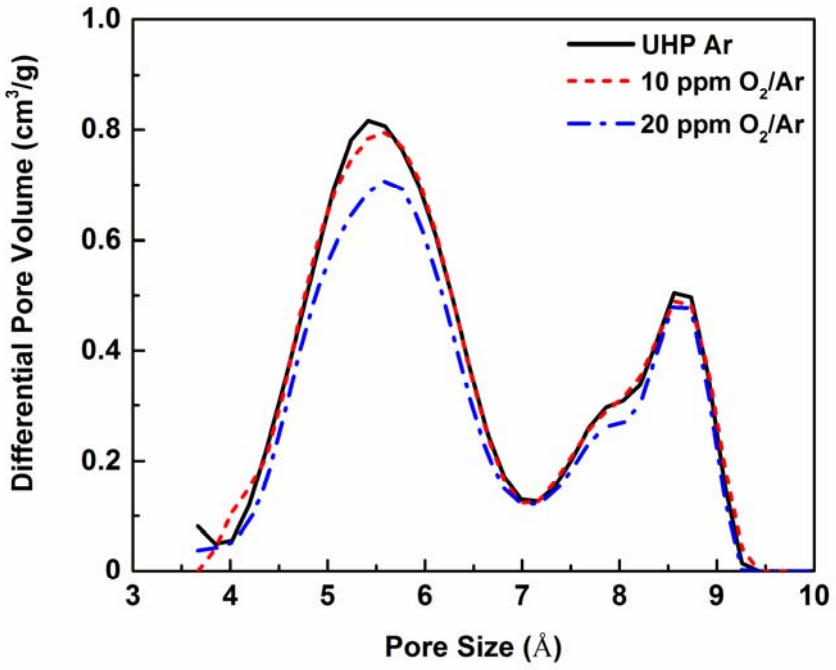

Figure 7.9. Pore size distribution derived from CO_2 uptake measurements at 0 ^{0}C in 6FDA:BPDA-DAM(1:1) derived CMS membranes pyrolyzed to 675 ^{0}C under varying oxygen concentration during pyrolysis.

Table 7.4. Pore volume and surface area of oxygen doped CMS membranes derived from 6FDA:BPDA-DAM(1:1) at 675 ^{o}C determined via CO_2 uptake measurements at 0 ^{0}C.

Atmosphere	Volume in pores ≤10.7 Å (cm^3/g)	Total area in pores ≥ 4 Å (m^2/g)
Argon	0.1600	522
10 ppm O_2/Ar	0.1590	521
20 ppm O_2/Ar	0.1400	454

7.5 Summary and Conclusions

Carbon molecular sieve membranes derived from 6FDA:BPDA-DAM(1:1) pyrolyzed to 675 ^{o}C in atmospheres containing low concentrations of oxygen were investigated for separation performance for the challenging C_2H_4/C_2H_6 gas pair. CMS membranes formed under 10 ppm O_2/Ar resulted in ~140 % increase in pure-gas permselectivity, with a moderate ~33% reduction in C_2H_4 permeability. Complementary

high pressure sorption indicated oxygen doping selectively modifies ultramicropores responsible for size and shape specificity of the CMS membranes, not the larger micropores responsible for high sorption capacity. However, increasing pyrolysis atmosphere oxygen concentration to 20 ppm resulted in reduction of both C_2H_4/C_2H_6 permselectivity and C_2H_4 permeability, as a result of "over doping" the CMS leading to an excessively tight pore structure. Complementary porosity measurements indicated reduced pore volume for ultramicropores at the higher 20 ppm oxygen concentration, supporting transport results.

This work provides a framework for utilization of oxygen doping as a ultra-fine pore size tuning technique, as impressive selectivity enhancements were realized for penetrants with 0.1 Å difference in size. However, it is evident that oxygen doping CMS membranes for larger penetrants exhibit increased sensitivity to pyrolysis atmosphere, compared to the smaller penetrants (e.g. CO_2/CH_4) previously studied. This is due to the relatively small population of large ultramicropores that allow diffusional jumps of compact large penetrants while restricting passage of slightly less compact large penetrants. In fact, one could envision a synergy between low level oxygen doping here and amine doping previously discussed in Chapters 4 and 5. Utilization of small amine dopants (e.g. ethylenediamine, EDA) upon a low-level oxygen doped CMS material could allow for additional functionalization of large ultramicropores, *as well as small micropores*, leading towards even greater membrane selectivity between large penetrants with modest reduction in productivities. However, this remains as speculation to this point, and warrants further investigation.

7.6 References

(1) Staudt-Bickel, C.; Koros, W. J. Olefin/paraffin gas separations with 6FDA-based polyimide membranes. *J. Memb. Sci.* **2000**, *170*, 205–214.

(2) Tanaka, K.; Taguchi, A.; Hao, J.; Kita, H.; Okamoto, K. Permeation and separation properties of polyimide membranes to olefins and paraffins. *J. Memb. Sci.* **1996**, *121*, 197–207.

(3) Xu, L.; Rungta, M.; Brayden, M. K.; Martinez, M. V.; Stears, B. A.; Barbay, G. A.; Koros, W. J. Olefins-selective asymmetric carbon molecular sieve hollow fiber membranes for hybrid membrane-distillation processes for olefin/paraffin separations. *J. Memb. Sci.* **2012**, *423–424*, 314–323.

(4) Breck, D. W. *Zeolite Molecular Sieves: Structure, Chemistry, and Use*; Wiley & Sons: New York, NY, 1974.

(5) Koresh, J. E.; Sofer, A. The Carbon Molecular-sieve Membranes: General Properties and Permeability of CH4/H2 Mixtures. *Sep. Sci. Technol.* **1987**, *22*, 973–982.

(6) Steel, K. M.; Koros, W. J. Investigation of Porosity of Carbon Materials and Related Effects On Gas Separation Properties. *Carbon N. Y.* **2003**, *41*, 253–266.

(7) Vu, D. Q.; Koros, W. J.; Miller, S. J. High Pressure CO 2 / CH 4 Separation Using Carbon Molecular Sieve Hollow Fiber Membranes. *Ind. Eng. Chem. Res.* **2002**, *41*, 367–380.

(8) Vu, D. Q.; Koros, W. J.; Miller, S. J. Effect of condensable impurity in CO2/CH4 gas feeds on performance of mixed matrix membranes using carbon molecular sieves. *J. Memb. Sci.* **2003**, *221*, 233–239.

(9) Rungta, M. Carbon Molecular Dense Film Membranes for Ethylene/Ethane Separations, Georgia Institute of Technology, 2012. Ph.D. Thesis.

(10) Salinas, O.; Ma, X.; Litwiller, E.; Pinnau, I. Ethylene/ethane permeation, diffusion and gas sorption properties of carbon molecular sieve membranes derived from the prototype ladder polymer of intrinsic microporosity (PIM-1). *J. Memb. Sci.* **2016**, *504*, 133–140.

(11) Salinas, O.; Ma, X.; Litwiller, E.; Pinnau, I. High-performance carbon molecular sieve membranes for ethylene/ethane separation derived from an intrinsically microporous polyimide. *J. Memb. Sci.* **2016**, *500*, 115–123.

(12) Singh, A.; Koros, W. J. Significance of entropic selectivity for advanced gas separation membranes. *Ind. Eng. Chem. Res.* **1996**, *35*, 1231–1234.

(13) Ning, X.; Koros, W. J. Carbon molecular sieve membranes derived from Matrimid® polyimide for nitrogen/methane separation. *Carbon* **2014**, *66*, 511–522.

(14) Fu, S.; Sanders, E. S.; Kulkarni, S. S.; Wenz, G. B.; Koros, W. J. Temperature dependence of gas transport and sorption in carbon molecular sieve membranes derived from four 6FDA based polyimides : Entropic selectivity evaluation. *Carbon* **2015**, *95*, 955–1006.

(15) Rungta, M.; Zhang, C.; Xu, L.; Koros, W. J. Membrane-Based Ethylene/Ethane Separation: The Upper Bound and Beyond. *AIChE J.* **2013**, *59*, 3475–3489.

(16) Kiyono, M.; Williams, P. J.; Koros, W. J. Effect of polymer precursors on carbon molecular sieve structure and separation performance properties. *Carbon N. Y.* **2010**, *48*, 4432–4441.

(17) Kiyono, M. Carbon Molecular Sieve Membranes For Natural Gas Separations, Georgia Institute of Technology, 2010. Ph.D Thesis.

(18) Grisdale, R. O. The Properties of Carbon Contacts. *J. Appl. Phys.* **1953**, *24*, 1288.

(19) Fu, S.; Wenz, G. B.; Sanders, E. S.; Kulkarni, S. S.; Qiu, W.; Ma, C.; Koros, W. J. Effects of pyrolysis conditions on gas separation properties of 6FDA/DETDA:DABA(3:2) derived carbon molecular sieve membranes. *J. Memb. Sci.* **2016**, *520*, 699–711.

(20) Rungta, M.; Xu, L.; Koros, W. J. Carbon molecular sieve dense film membranes derived from Matrimid® for ethylene/ethane separation. *Carbon* **2012**, *50*, 1488–1502.

(21) Campo, M. C.; Magalhães, F. D.; Mendes, A. Comparative study between a CMS membrane and a CMS adsorbent: Part I—Morphology, adsorption equilibrium and kinetics. *J. Memb. Sci.* **2010**, *346*, 15–25.

(22) Lozano-Castelló, D.; Cazorla-Amorós, D.; Linares-Solano, A. Usefulness of CO2 adsorption at 273 K for the characterization of porous carbons. *Carbon* **2004**, *42*, 1233–1242.

CHAPTER 8. CONCLUSIONS AND RECOMMENDATIONS

8.1 Dissertation Overview

Carbon molecular sieve (CMS) membranes are emerging as an attractive class of advanced materials for application in large-scale gas separations. The ultra-rigid structure allows for CMS materials to exhibit simultaneous high permeability and selectivity for a variety of challenging gas separations. However, linking CMS formation, processing and precursor structure to resulting performance is desired. While CMS membranes display impressive separation performance, similar to their polymeric precursors, CMS membranes are subject to a physical aging phenomenon, in which partial densification of the CMS microstructure leads to reduced productivity and increased selectivity. While neither of these issues are "show stoppers" in the advancement of CMS membrane research per se, understanding the details of CMS formation and physical aging can enable further engineering of the CMS microporous structure, leading towards enhanced performance and stability for challenging gas separations.

The overarching goal of this thesis was to investigate additional methods for modifying and controlling separation performance of carbon molecular sieve membranes. While this work focused on modification of CMS materials derived from 6FDA:BPDA-DAM(1:1) polyimide precursor, the frameworks provided allows facile extension to CMS membranes derived from various polymer precursors and pyrolysis conditions. The research objectives outlined in Chapter 1 are reproduced below for convenience:

1) Development of post-synthetic modification of carbon molecular sieve membranes with diamine dopants (Chapter 4)
2) Investigation of size and functionality of amine dopants for modification of carbon molecular sieve membranes (Chapter 5)
3) Hypothetical transformation pathway from random coil precursor to rigid molecular sieving carbon molecular sieve matrix (Chapter 6)
4) Investigation of low level oxygen doping of carbon molecular sieve membranes for olefin/paraffin separations (Chapter 7)

The following section reviews the key findings and contributions to this work.

8.2 Conclusions

8.2.1 Post-pyrolysis Engineering of Carbon Molecular Sieve Pore Structure via Addition of Reactive Components

The first section of this thesis focused on developing a post-synthetic modification technique, with the initial goal of suppressing physical aging of CMS membranes by creating linkages between adjacent CMS sheets with the rigid *p*-phenylenediamine as a reactive molecule. Unfortunately, long term permeation results showed amine treated CMS membranes still physically aged under vacuum conditions. Nevertheless, this preliminary work showed that engineering of the CMS microporous structure is possible via post-synthetic modification with reactive compounds, as interplay between reactive dopant concentration and resulting performance was found. Complementary gas sorption measurements indicated amine dopants were not selectively placed at the size-selective ultramicropore edges as initially hypothesized; rather, dopants

were present in a combination of ultramicropores and micropores, leading to alterations in *both distributions simultaneously*, a unique feature of this work. These results were the first to highlight the importance of the pores within the "cross-over" regime between "large" ultramicropores and "small" micropores as important factors in engineering CMS performance for gas separations. In terms of smaller gas pairs (e.g. CO_2/CH_4), these "cross-over" pores are not directly responsible for discrimination between penetrants, but rather serve as pathways with little transport resistance. Removal of some high throughput less selective pathways through introduction of the amine dopants increased the diffusional (size and shape) selectivity of treated CMS membranes, forcing penetrant transport to occur through more selective pathways.

Further investigation of the amine dopant treatment expanded both chemical reactivity and structure of amine dopants, in order to establish a reactive molecule structure-resulting CMS property relationship. Reducing size, or increasing flexibility, of the selected amine dopant led to increased functionalization of the CMS microporous structure, resulting in further enhancements in separation efficiency compared to the original *p*-phenylenediamine treated materials. However, for the CO_2/CH_4 separation, the relatively small population of "cross-over" pores responsible for increased selectivity upon functionalization for these smaller penetrants, as smaller amine dopants resulted in marginal selectivity gains with marked productivity reductions. On the other hand, testing the same materials for the larger C_3H_6/C_3H_8 gas pair, which have a higher dependence upon "large" ultramicropores for diffusive jumps, showed significant permselectivity increases as dopant size decreased; a direct result of fewer active less selective pathways due to presence of the reactive molecules. These results confirm that control of pores

within the "cross-over" between "large" ultramicropores and "small" micropores are critical in tuning resulting CMS separation performance, particularly for larger penetrants which rely heavily on these pores for successful diffusive jumps. Selective functionalization of pores within this terrain leads to increased membrane efficiency while maintaining attractive productivities.

Recalling earlier work showing that addition of ppm amounts of molecular oxygen *to the pyrolysis atmosphere* leads to modification of only size selective ultramicropores helped identify a possible synergy between oxygen and amine doping techniques. Post-synthetic amine doping of CMS membranes that have been oxygen doped during synthesis will modify both ultramicropore and "cross-over" pore regimes, where amine doping will modify the large less selective pathways not affected by the fine oxygen doping pore tuning. Application of these two treatments upon the same material may allow for even greater options for size and shape selectivity than CMS membranes tuned by only oxygen doping or amine doping. Additionally, increased presence of CMS chemical heterogeneity (e.g. carbonyls and hydroxyl groups) due to the oxygen doping, may result in increased amine functionalization at a given treatment condition.

Nuclear magnetic resonance studies of amine doped CMS materials indicated new covalent bonds formed between reactive amine dopants and CMS membranes, providing evidence that amine dopants were successful in chemically modifying the CMS membranes. Unfortunately, degradation of the impressive separation performance of amine treated materials was discovered, likely a result of amine-CO_2 interactions leading to some reversibility of amine-CMS bonds. However, the degraded materials still have

higher separation efficiency than un-doped CMS and are stable upon further exposure to CO_2.

These results show that engineering of the CMS microporous structure via exposure to reactive molecules is possible; however, caution must be exercised to ensure stability of the reactive dopants in the presence of aggressive gas feed components. Furthermore, while the amine molecules investigated in this current study did not lead to aging resistant CMS materials, impeding movement in micropores by addition of reactive linkages still offers a path towards stabilization, and provides a wide variety of methods from which to choose for future research.

8.2.2 Development of Self-consistent Mechanism Linking Random Polymer Precursor Structure, Formation and Processing Conditions to Resulting Carbon Molecular Sieve Membrane Performance

Owing to the amorphous structure, traditional characterization techniques fail to supply the angstrom-level detail required for directed engineering of CMS materials for challenging gas separations. Additionally, there is a fundamental gap in linking a random coil polyimide precursor to the resulting ultra-rigid CMS structure, which was addressed in this work. For the first time, a self-consistent mechanism that incorporates and connects structure-property relationships to the CMS formation process was presented. In particular, the novel concept of entanglement-driven polymer chain scission, forming strands that simultaneously aromatize and linearize was introduced. Formation of the final CMS structure is caused by entropy-driven organization of these aromatic strands, similar to but more complex than liquid crystals, forming molecular sieving plates. Simultaneous high sorption capacity and diffusion coefficients in CMS materials result

from micropores formed by kinetically hindered organization of the aromatic sheets containing the size selective ultramicropores.

This newly developed self-consistent mechanism allows for understanding how various pyrolysis processing steps aside from final pyrolysis temperature (i.e. ramp rates, thermal soak times, cooling rates) affect performance of resulting CMS materials. Additional tuning of separation performance is possible considering the aforementioned polymer chain scission-aromatic strand formation mechanism via alteration of polymer precursor composition or chemistry. However, investigation of these items will require considerable future work.

8.2.3 Addition of Molecular Oxygen to Pyrolysis Atmosphere as Fine Tuning Technique of Carbon Molecular Sieve Pore Structure for Application to Olefin/Paraffin Separations

Insight gained into the final structure responsible for attractive performance of CMS materials from the developed self-consistent mechanism was used to guide fine tuning of CMS membranes for the C_2H_4/C_2H_6 separation. This separation is of significant importance and challenge owing to the similar effective size and condensabilities of the penetrants of interest. Addition of molecular oxygen into the pyrolysis atmosphere results in selective functionalization of the edges of the aromatic stands that form the ultramicropores, shifting to a more selective pore size distribution. This leads to increased diffusional selectivity as only the aromatic strand edges are functionalized; no augmentation of traditional micropores results as the pyrolysis temperature, thus the kinetic driving forces for organization of aromatic plates, remains constant. However, a number of "small" micropores residing in the "cross-over" regime may result from

defects during plate organization. Upon oxygen doping, this pore population may transition to a smaller size that will impact jump opportunities for the larger C_2H_4 and C_2H_6 penetrants, whereas previously these pores were transparent to both penetrants. While this mechanism supports the transport trends noted in the C_2H_4/C_2H_6 gas pair, confirmation of this transition will require significant future work.

Oxygen doping enables much finer engineering of the resulting CMS performance when compared to changing other processing parameters such as final pyrolysis temperature, and resulted in significant (~140%) C_2H_4/C_2H_6 selectivity enhancement with mild (~33%) reduction in C_2H_4 permeability. However, caution must be exercised during application of this technique, as further addition of oxygen past a critical concentration results in removal of a significant amount of accessible selective pathways, leaving a number of larger less selective pathways active resulting in unattractive performance. For the C_2H_4/C_2H_6 separation investigated, this critical oxygen level occurs at a much lower concentration (10 ppm O_2/Ar) than for the CO_2/CH_4 separation (30 ppm O_2/Ar), highlighting the increased sensitivity of large penetrants to fine changes in the CMS microstructure and the notion that a CMS membrane optimized for one gas separation may not perform ideally for another separation.

8.3 Recommendations for Future Work

During this thesis, deeper understanding of the complex amorphous CMS structure was developed, enabling guided application of both new and previously applied CMS tuning techniques. However, there is still a significant amount of work to advance the understanding impacts of processing and formation of CMS membranes upon

separation performance. This following section outlines several possible areas for future directions of CMS related research.

8.3.1 Modification of Carbon Molecular Sieve Membranes with Reactive Molecules

The amine doping treatment investigated showed that addition of ppm levels of amine dopants in THF positively impacts separation performance for both CO_2/CH_4 and C_3H_6/C_3H_8 gas pairs. However, degradation of amine treated membranes suggesting a partial reversal of amine-CMS bonds after exposure to CO_2. For this treatment to be a viable tuning technique, the cause of performance reduction needs to be investigated and suppressed. Exposure of streams of CO_2 feeds with controlled humidity to amine treated CMS membranes while monitoring performance, will provide insight into the performance degradation observed. Complementary spectroscopic characterization (i.e. NMR, FTIR) of amine treated CMS membranes before and after exposure to humidified CO_2 streams may provide additional insight to support trends observed in traditional transport (e.g. permeation and sorption) measurements.

Furthermore, reversibility of the amine-CMS degradation may be probed by reheating the membrane under a dry feed (e.g. UHP N_2) driving off the CO_2. Thus, the primary amine will be regenerated and may reestablish a covalent bond with the CMS. This requires careful consideration during membrane module construction as selecting an appropriate epoxy that can withstand high temperature exposure and not affect membrane performance will be critical.

Initial studies of amine doping in this work treated CMS membranes in a THF solution containing the desired amine dopant; however, if applied on an industrial scale this method may be unfavorable. Instead, addition of small amounts of the desired amine

dopant to the pyrolysis furnace purge post-synthesis may be preferred, as the number of process steps would be reduced. Alternatively, simultaneous doping and CMS synthesis by addition of amine or other dopants to the pyrolysis atmosphere may be explored, analogous to oxygen doping of CMS membranes.

The framework for extension of amine doping provided above will only be worthwhile if stability of amine or alternative dopants within CMS materials is addressed. Nevertheless, similar methodologies utilizing different chemistries could be implemented as alternative doping strategies, if amines fail to be inherently stable. One such example is the use of boronic acids, which have been shown to covalently link between graphene oxides layers, forming porous networks with increased gas storage capacities (*1*). While CMS materials formed under inert UHP argon may not contain the required carbonyl and hydroxyl functionalities required for this covalent linkage, oxygen doped CMS membranes likely will (*2*). Additionally, while reactions between organoboron compounds and CO_2 have been reported, they are mediated with transition metal-based catalysts (*3*). Furthermore, porous networks derived entirely from boronic acids have shown excellent stability when exposed to pure CO_2 (*4*). Considering these statements, treatment of an oxygen doped CMS membrane with boronic acids may be analogous to amine doping, and is predicted to exhibit stability upon exposure to CO_2 and other gases.

8.3.2 Investigation of Entropic Selectivity for Oxygen Doped Carbon Molecular Sieve Membranes

Addition of ppm levels of molecular oxygen to the pyrolysis atmosphere during CMS synthesis leads to functionalization of size selective ultramicropores, not the

micropores responsible for gas sorption. These rigid CMS ultramicropore windows enable discrimination between differently shaped, yet similarly sized materials by restriction of various degrees of rotational and/or vibrational freedom, resulting in an "entropic selectivity"; however, the role of oxygen doping upon entropic selectivity has yet to be investigated. Determination of sorption enthalpy and activation energies of diffusion and permeation for oxygen doped samples will allow for estimating entropic and energetic contributions to the high diffusional selectivities exhibited by oxygen doped CMS membranes. While both energetic and entropic factors contribute, the tightened critical ultramicropore dimension in the oxygen doped CMS will result in further restriction of degrees of freedom for a penetrant, increasing entropic selectivity contributions. This restriction will likely be more dominant when investigating olefin/paraffin separations, as small differences in ultramicropore dimensions can lead to significant advantages in separating the slightly more compact olefins from the less compact paraffins.

8.3.3 Precursor Structure and Processing Effects on Carbon Molecular Sieve Membrane Performance

Development of the self-consistent CMS formation mechanism provides a framework in connecting precursor structure, formation and processing conditions to resulting CMS performance. Further investigation of these factors, in a controlled and thoughtful manner, will allow for further refinement, expansion and generalization of this mechanism.

Preliminary investigations into structural factors that affect aromatic strand formation, in 6FDA:BPDA-DAM derived CMS identified the BPDA unit as a potential

weak point in the polymer structure as increasing the 6FDA:BPDA ratio from (1:1) to (2:1) led to increases in *both selectivity and productivity* for the CO_2/CH_4 gas pair. This suggests that longer aromatic strands are formed, allowing for larger yet more compact ultramicropore plates resulting from entropy-driven organization. However, the larger plates will be subject to increased steric limitations leading to an overall more open CMS structure with increased micropore dimensions, reflected by higher sorption capacity and diffusion coefficients. Therefore, it is of interest to investigate varying concentrations of the 6FDA:BPDA monomer ratios, in a consistent manner, to refine this aspect of strand formation with respect to weak links in the polymer chain during the simultaneous fragmentation and linearization process that occurs as the polymer chain degrades. Additionally, investigation into pyrolysis ramp rates during CMS synthesis will provide another avenue of refining the aromatic strand formation mechanism. For example, faster pyrolysis ramp rates is envisioned to increase fragmentation rates forming shorter strands as a result of the increased thermal stresses applied to the entangled polymer chains during degradation. As excluded volume effects of the entropy-driven organization is dependent upon strand length, shorter aromatic strands are expected to form smaller ultramicropore plates. During the "thermal soak" phase of the pyrolysis process these smaller ultramicropore plates may organize into an overall tighter CMS structure due to competing effects of kinetic mobility and steric hindrances, leading to decreased permeability and increased selectivity. This seems somewhat counterintuitive, as smaller strands could also increase frustration during organization; however, the integrated framework developed within this work will allow for self-consistent analysis of any results from future exploration.

8.4 References

(1) Srinivas, G.; Burress, J. W.; Ford, J.; Yildirim, T. Porous graphene oxide frameworks: Synthesis and gas sorption properties. *J. Mater. Chem.* **2011**, *21*, 11323.

(2) Kiyono, M. Carbon Molecular Sieve Membranes For Natural Gas Separations, Georgia Institute of Technology, 2010. Ph.D. Thesis.

(3) Liu, Q.; Wu, L.; Jackstell, R.; Beller, M. Using carbon dioxide as a building block in organic synthesis. *Nat. Commun.* **2015**, *6*, 5933.

(4) Ockwig, N. W.; Cote, A. P.; Keeffe, M. O.; Matzger, A. J.; Yaghi, O. M. Porous , Crystalline , Covalent Organic Frameworks. *Science* **2005**, *310*, 1166–1171.

APPENDIX A. GAS COMPRESSIBILITY FACTORS

This appendix contains the gas compressibility factors used within this work. The compressibility factor (z) is used to account for the deviation of real gases from the idea gas law, as shown by:

$$z = \frac{PV}{nRT} = \frac{P\hat{V}}{RT} \tag{A.1}$$

where P is the pressure, V is the volume of the system, n is the number of moles of the gas of interest, T is the absolute temperature, and R is the universal gas constant. In the case when the system volume is not specifically known, the specific molar volume ($\hat{V}$) of the gas of interest can be used to simplify Equation A.1. For an ideal gas, by definition, z = 1.

The pressure dependent compressibility factor equations of pure gases used in this work were obtained from the National Institute of Standards and Technology (NIST) SUPERTRAPP software, Version 3.1. The pressure dependent equations are compiled in Table A.1 below, where pressure (P) is in units of psia.

Table A.1. Pressure dependent gas compressibility equations.

Gas	Temperature	Compressibility Equation
CO_2	35 °C	$z = 1 - 3.044x10^{-4}P - 3.588x10^{-8}P^2 - 7.937x10^{-11}P^3$
CH_4	35 °C	$z = 1 - 1.370x10^{-4}P + 1.646x10^{-8}P^2 + 3.492x10^{-12}P^3$
C_2H_4	35 °C	$z = 1 - 3.519x10^{-4}P - 8.215x10^{-8}P^2 - 2.966x10^{-11}P^3$
C_2H_6	35 °C	$z = 1 - 4.683x10^{-4}P - 1.487x10^{-7}P^2 - 1.681x10^{-10}P^3$

APPENDIX B. SUPPLEMENTARY INFORMATION FOR CARBON MOLECULAR SIEVE STRUCTURE AND MEMBRANE PERFORMANCE (CHAPTER 7)

This appendix contains supplementary information for the results and analysis pertaining to Chapter 7 of this thesis, parts of which are reproduced from "Rungta, M.; Wenz, G.B.; Zhang, C.; Xu, L.; Qiu, W.; Adams, J.S.; Koros, W.J., Carbon Molecular Sieve Structure Development and Membrane Relationships. *Carbon,* **2017**, *115*, 237-248.

B.1 Supplementary Transport Data

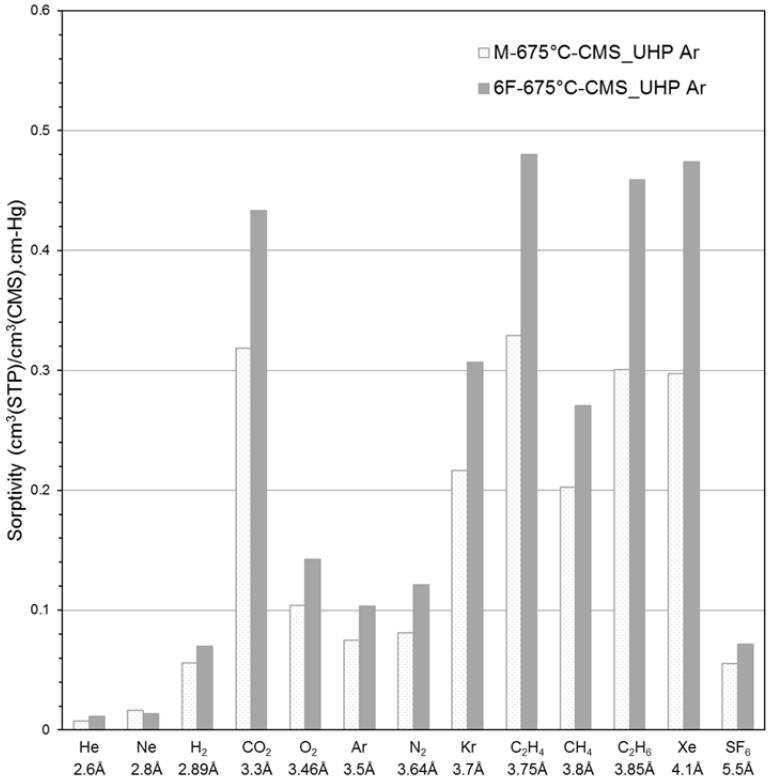

Figure B.1. Average sorption coefficients of different gases for CMS derived from Matrimid® and 6FDA:BPDA-DAM(1:1) at 675 °C under UHP Argon. Sorption coefficients are for 50 psia equilibrium pressure at 35 °C. Reproduced from (*1*).

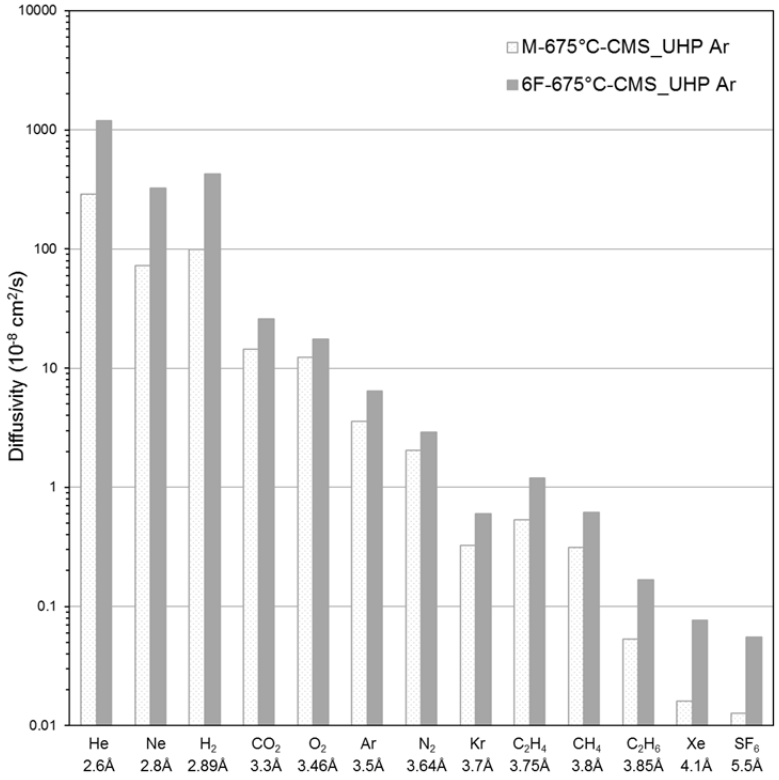

Figure B.2. Average transport diffusivities of different gases for CMS derived from Matrimid® and 6FDA:BPDA-DAM(1:1) at 675 ^{0}C under UHP Argon. Diffusion coefficients were back-calculated from permeabilities and sorption coefficients at 35 °C, 50 psia feed pressure. Reproduced from (*1*).

B.2 Elemental Analysis of CMS derived from 6FDA:BPDA-DAM(1:1)

Table B.1. Elemental analysis of 6FDA/BPDA-DAM(1:1) CMS.

Final Pyrolysis Temperature (°C)	**Carbon (wt%)[1]**	**Hydrogen (wt%)[1]**	**Nitrogen (wt%)[1]**	**Oxygen (wt%)[2]**	**Fluorine (wt%)[3]**
Precursor	62.26	2.62	6.60	15.08	13.43
500	78.28	3.23	6.98	13.67	<0.0001
550	83.38	2.90	6.49	5.68	<0.0001
600	85.81	2.09	5.62	4.10	<0.0001
675	86.48	1.52	5.41	5.00	<0.0001
800	87.53	1.12	4.76	4.82	<0.0001
1000	89.75	0.62	3.16	4.09	<0.0001

[1]Measured with CHN combustion analyzer. [2] Measured IR pyrolysis detection. [3] Measured via flask combustion.

B.3 References

(1) Rungta, M. Carbon Molecular Dense Film Membranes for Ethylene/Ethane Separations, Georgia Institute of Technology, 2012. Ph.D. Thesis.